



Università degli Studi di Cagliari

DOTTORATO DI RICERCA

IN INGEGNERIA INDUSTRIALE

Ciclo XXXII

**Magneto-Fluid-Dynamic interaction phenomena
for aerospace applications**

SSD ING-IND/31

Presentata da:

Silvia Maria Collu

Coordinatore Dottorato:

Francesco Aymerich

Tutor:

Augusto Montisci
Antoine Alemany

Esame finale anno accademico 2018 – 2019

Tesi discussa nella sessione d'esame Giugno Luglio 2020



Questa Tesi può essere utilizzata, nei limiti stabiliti dalla normativa vigente sul Diritto d'Autore (Legge 22 aprile 1941 n. 633 e succ. modificazioni e articoli da 2575 a 2583 del Codice civile) ed esclusivamente per scopi didattici e di ricerca; è vietato qualsiasi utilizzo per fini commerciali. In ogni caso tutti gli utilizzi devono riportare la corretta citazione delle fonti. La traduzione, l'adattamento totale e parziale, sono riservati per tutti i Paesi. I documenti depositati sono sottoposti alla legislazione italiana in vigore nel rispetto del Diritto di Autore, da qualunque luogo essi siano fruiti.

Silvia Maria Collu gratefully acknowledges Sardinian Regional Government for the financial support of her PhD scholarship (P.O.R. Sardegna F.S.E. - Operational Programme of the Autonomous Region of Sardinia, European Social Fund 2014-2020 - Axis III Education and training, Thematic goal 10, Investment Priority 10ii), Specific goal 10.5.



Dedicated to my father and my mother

Acknowledgements

A few words to thank all the people who have been close to me for the past three years and who have helped me get this job done.

First of all, I'd like to thank my supervisor Augusto Montisci, for his willingness, his support, for being so generous, unconventional and for encouraging me to "dare more".

Part of this dissertation has been developed at the SIMAP Laboratory of the CNRS, in Grenoble. Thanks to my supervisor Antoine Alemany for his mankinds, his determination and for sharing his enormous experience and expertise in the MHD field with me.

Special thanks go to Sara Carcangiu, who has helped me a lot whenever I needed it in these years, for her kindness and her friendship and for her constant encouragement.

Further thanks go to the whole research group of the Department of Electrical and Electronics Engineering of the University of Cagliari, coordinated by Prof. Alessandra Fanni.

Last but not least, I would like to thank my husband for encouraging me and for always believing in me, especially during my stay in Grenoble.

Finally, the most important thought is for my daughter Martina. Thanks for being the greatest gift of my life.

Abstract

The Magneto-hydro-dynamics (MHD) is the discipline that studies the interactions between conductive fluids and applied magnetic fields. It integrates the phenomena of fluid dynamics and magnetism or electromagnetism, but also new ones specific to the interaction of the 2 domains.

One of the remarkable features of this interaction is the mechanisms of induction to act without contact. One of the important properties that influence the intensity of electromagnetic forces is the electrical conductivity of the fluid. The dimensionless parameters which control the phenomena are generally 3; these are the classic Reynolds number (Re) in fluid mechanics, the interaction parameter (N) ratio of electromagnetic forces to inertia forces and the magnetic Reynolds number (Rm), ratio of the diffusion time of the magnetic field in the medium and the convection time. The proposed study is directed towards the analysis of 2 situations which a priori have little similarity but which in reality find their justifications in the sense that they both relate to flows around obstacles which are characterized by a wake whose configuration depends in particular on the magnetic Reynolds number. The analysis was performed digitally using the Finite Elements Method (FEM) with the software Comsol®. The first situation concerns the flow around a cylinder when the velocity field and the magnetic field are parallel to infinity. The analysis focused on the role of different parameters such as the influence of confinement, magnetic permeabilities relating to the fluid and the cylinder, and the magnetic Reynolds number. In all cases, the configuration of the wake, and in particular of von Karmann street, was analyzed either in terms of Strouhal number and in terms of drag exerted by the fluid on the cylinder. It has been observed in particular the existence of a critical value for the interaction parameter for which the von Karmann street disappears and is replaced by 2 vortices which remain attached to the cylinder. This critical value depends in particular on the magnetic Reynolds number. When this number becomes high the critical value of N is increased the vortices of von karmann persist for high magnetic fields.

In the second part of the thesis, the analysis method developed in the Part I has been applied to the study of the Space propulsion system called Mini-Magnetosphere Plasma Propulsion (M2P2).

The proposed system exploits the action of the solar wind, which is a completely dissociated hydrogen plasma made up of electrons and protons moving at high speed between $300 \div 800$ km/s, this wind is therefore sensitive to the action of field magnetic. The method is based on the creation of a large-scale magnetic field transported by a plasma magnetized by a coil, to thus form a mini-magnetosphere which deflects the solar wind as a sail would do it.

This interaction generates a force to propel the spacecraft. Although low, the force applied over a long period of time makes it possible to reach speeds of several tens of km / s. The physics of the phenomenon can be compared, any scale kept, to the terrestrial magnetic field which protects the earth from solar winds. In this study, two specific aspects were considered. The first one concerns the operative conditions that allow the ejected plasma to be captured by the magnetic field, in this way inflating the sail. The second one, concerns the calculation of the thrust that the wind exerts on the sail. The analysis has been performed resorting to the non-dimensional analysis on one side to reduce the computational burden of the FEM analysis, on the other side because it made it possible to perform at the same time the analysis of the real application and a possible experimental setup on ground.

TABLE OF CONTENTS

ACKNOWLEDGEMENTS	IV
ABSTRACT	V
TABLE OF CONTENTS	VII
LIST OF FIGURES	X
LIST OF TABLES	XIII
THESIS OUTLINE	15
1 FUNDAMENTALS OF MHD.....	16
1.1 INTRODUCTION	16
2 MHD EQUATIONS.....	20
2.1 GENERAL FORM OF MHD EQUATIONS	20
2.2 THE NON-DIMENSIONAL ANALYSIS.....	21
<i>2.2.1 Navies-Stokes equation.....</i>	<i>22</i>
<i>2.2.2 The continuity equation (incompressible fluid)</i>	<i>22</i>
<i>2.2.3 Vector potential equation</i>	<i>23</i>
<i>2.2.4 Ohm's law</i>	<i>23</i>
<i>2.2.5 Faraday-Neumann-Lenz equation.....</i>	<i>23</i>
<i>2.2.6 Ampère's law.....</i>	<i>24</i>
<i>2.2.7 Continuity equations</i>	<i>24</i>
<i>2.2.8 Equation of the Magnetic Induction.....</i>	<i>24</i>
2.3 NON-DIMENSIONAL NUMBERS: FUNDAMENTAL ASPECTS AND APPLICATIONS	25
3 MHD FLOW ANALYSIS OF A CONDUCTIVE FLUID AROUND A CYLINDER	28
3.1 GENERAL ASPECTS.....	28
3.2 FLUID DYNAMIC ANALYSIS.....	29
<i>3.2.1 Types of motion.....</i>	<i>29</i>
<i>3.2.2 Reynolds number.....</i>	<i>29</i>
<i>3.2.3 Vortex Shedding</i>	<i>30</i>
<i>3.2.4 Trochal number</i>	<i>31</i>
<i>3.2.5 Detachment point</i>	<i>33</i>
<i>3.2.6 Dragging Force.....</i>	<i>34</i>
3.3 ANALYSIS OF THE EFFECTS OF AN AXIAL MAGNETIC FIELD	35

3.3.1 Numerical model description	36
3.3.2 Equations and initial conditions	39
3.3.3. Characterisation of the magnetic field distribution for small Rm and for any value of the permeabilities ratio: μ_{flu}/μ_{cyl}	43
3.3.3.1 Contribution to the magnetic field due to the walls.....	45
3.3.3.2 Contribution of magnetic field due to the discontinuity of magnetic permeability.	47
3.3.4 Characterisation of the magnetic field distribution for a generic value of magnetic Reynolds number.	52
3.3.5 Fluid-dynamic boundary conditions	53
3.4 FEM MODEL	54
3.4.1 FEM analysis of the Fluid-Dynamics aspects.....	56
3.5 RESULTS FOR SMALL MAGNETIC REYNOLDS NUMBER	59
3.5.1 First case: $M = 1$	60
3.5.1.1. Evolution of drag coefficient	64
3.5.1.2 Evolution of detachment point	69
3.5.1.3 Cavity at low velocity of fluid.....	71
3.5.2 Dependency of the interaction parameter N on fluid confinement	73
3.5.3 Second case: $M = 1000$	79
3.5.4 Third case: $M = 1/100$	82
3.6 RESULTS FOR HIGH MAGNETIC REYNOLDS NUMBER	85
3.6.1 $Rm = 12.5$ and $M = 1$	85
3.6.1.1 Evolution of drag coefficient	90
3.7 CONCLUSION	93
4 MAGNETO PLASMA SAIL	94
4.1 INTRODUCTION	94
4.2 STATE-OF-THE-ART OF SOLAR SAILS.....	95
4.2.1 Solar wind.....	95
4.2.2 Types of solar sails.....	96
4.3 M2P2 – ANALYTICAL MODEL	102
4.4 FEM MODEL	103
4.4.1 Starting FEM model.....	103
4.4.2 Sail inflation: conditions for deviating the plasma	103
4.5 PROPULSIONS SYSTEM FEM ANALYSIS.....	109
4.5.1 Thrust on the sail.....	109
4.6 PROPULSIONS SYSTEM DIMENSIONLESS ANALYSIS	114
4.7 CONCLUSION	117

5 APPENDIX118

5.1 APPENDIX 1.118

5.2 APPENDIX 2.121

5.3 APPENDIX 3.122

BIBLIOGRAPHY124

List of figures

Figure 3.1: Flow separation from a fixed cylinder [3]	30
Figure 3.2: Flow on a circular cylinder with a smooth wall [4].	31
Figure 3.3: Strouhal number vs Reynolds number [5]	32
Figure 3.4: Comparison of Strouhal number versus Reynolds number for unbounded flow around a circular cylinder with different results in the literature: (—), experimental work of Williamson [7]; (...), numerical results of Henderson [8]; (○), numerical results of Posdziech and Grundmann [9]; (□) numerical results of Sahin and Owens [6].	33
Figure 3.5: Diagram of the angle of detachment vs the Reynolds number [10] [11]	33
Figure 3.6: Variation of drag coefficient with Reynolds number for spheres, cylinders, and disks [12]	35
Figure 3.7: Geometry of the model	37
Figure 3.8: Magnetic field distribution	37
Figure 3.9: Profile of velocity in the input section	43
Figure 3.10: Magnetic field generated by the small element on the upper wall	45
Figure 3.11: Contribution to the Magnetic field due to the two walls.	47
Figure 3.12: Discontinuity of tangential component of the magnetic induction and of radial component of magnetic field	48
Figure 3.13: Magnetic field in a generic point M of the domain due of the distribution $\Gamma\alpha$.	49
Figure 3.14: Magnetic field in a generic point M of the domain due of the distribution $q\alpha$	50
Figure 3.15: Hydrodynamic boundary conditions.	54
Figure 3.16: FEM Study: geometry.	55
Figure 3.17: FEM Study: mesh.	55
Figure 3.18: Velocity field and formation of Von Karman's wake behind the cylinder ($Re=200$)	57
Figure 3.19: Fluid pressure profile along the surface of cylinder.	57
Figure 3.20: Drag coefficient ($V = 1 \text{ m/s}$, $Re = 1000$)	58
Figure 3.21: Velocity profile upstream [a] and downstream [b] of the cylinder.	59
Figure 3.22: Distribution of magnetic field: $\mu_{cyl} = \mu_{flu}$	61
Figure 3.23: Von Karman's wake in the fluid dynamic system ($N = 0$).	62
Figure 3.24: Hydrodynamic configuration modified by magnetic field.	62

Figure 3.25: Cd coefficient for different values of N when $Re = 2000$.	65
Figure 3.26: Time average of fluid pressures on the cylinder versus N .	66
Figure 3.27: Trends of the drag coefficient for several Reynolds number versus interaction parameter N compared with experimental (a) and theoretical (b) results [17].	67
Figure 3.28: Trends of the drag coefficient versus interaction parameter for $Re = 1000$.	67
Figure 3.29: Distribution of vorticity for small values of N	68
Figure 3.30: Angular position of the boundary layer separation point from the stagnation point	69
Figure 3.31: Oscillation of detachment point versus N .	69
Figure 3.32: fluid vein detachment mechanism.	70
Figure 3.33: Eletromagnetic force effect.	71
Figure 3.34: Cavity and stagnation point of velocity in case $Re = 1000$ for $N = 1$.	72
Figure 3.35: Streamline of velocity and magnetic field inside and outside the cavity for $N = 572$	
Figure 3.36: Streamline of velocity and magnetic field inside and outside the cavity for $N = 2073$	
Figure 3.37: Interactions Magneto Fluid Dynamic.	74
Figure 3.38: Evolution of N_c with the growth of C .	76
Figure 3.39: Values of Cd for $H = 0.8 m$.	77
Figure 3.40: Values of Cd for $H = 0.45 m$.	77
Figure 3.41: Values of C_d for $H = 0.3 m$.	78
Figure 3.42: Distribution of magnetic field \mathbf{B} when $\mu_{cyl} > \mu_{flu}$.	79
Figure 3.43: Cd coefficient for $Re = 10000$.	81
Figure 3.44: Evolution of the drag coefficient versus the interaction parameter	81
Figure 3.45: Streamline of velocity and magnetic field inside and outside the cavity for $N = 0.482$	
Figure 3.46: Distribution of magnetic field \mathbf{B} when $\mu_{cyl} < \mu_{flu}$	82
Figure 3.47: Cd coefficient for different values of N when $Re = 10000$	84
Figure 3.48: Evolution of the drag coefficient versus the interaction parameter	85
Figure 3.49: Streamline of velocity and magnetic field inside and outside the cavity for $N = 0.4$.	85
Figure 3.50: Streamlines of velocity and magnetic field when $N = 0.1$.	86
Figure 3.51: Streamlines of velocity and magnetic field when $N = 1$.	87
Figure 3.52: Magnetic field streamlines (red) and velocity field streamlines (blu) for $N = 1$.	88
Figure 3.53: Magnetic field streamlines and velocity field streamlines in case $N = 5$.	89

Figure 3.54: Magnetic field streamlines and velocity field streamlines in case $N=10$.	89
Figure 3.55: Magnetic field streamlines and velocity field streamlines in case $N = 20$.	90
Figure 3.56: Cd coefficient in case $Re = 1000$ and $N = 0.1$ [a] and $N = 1$ [b].	91
Figure 3.57: Cd evolution versus N with $0 < N < 1$, for $Rm = 0.125$ and $Rm = 12.5$	91
Figure 3.58: Cd evolution versus N with $0 < N < 20$, for $Rm = 0.125$ and $Rm = 12.5$.	92
Figure 4.1: Solar wind	95
Figure 4.2: Photon Sail.	97
Figure 4.3: Electric Sail [26]	98
Figure 4.4: Magnetic Solar sail	99
Figure 4.5. Magnetosphere of MagSail [28].	100
Figure 4.6: Magneto Plasma Sail M2P2	101
Figure 4.7: Spaceship with magnetic coil source	101
Figure 4.8: Geometrical FEM model and mesh	104
Figure 4.9: Magnetic flux density norm B (log scale)	105
Figure 4.10: Effect of plasma injection in the presence of magnetic field.	106
Figure 4.11: Magnetic flux density norm B (log scale); left without plasma injection; right with plasma injection.	107
Figure 4.12: Effect of plasma injection on velocity field: with solar wind.	107
Figure 4.13: Deformation of the magnetosphere without plasma (above) and with plasma (below)	112
Figure 4.14: Forces applied to the two cross sections	113
Figure 4.15: Net thrust applied on the solid coil with and without plasma injection	113
Figure 5.1: Magnetic field generate by the small element on the upper wall.	118

List of Tables

Table 1.1: Conductivity values of some fluids	17
Table 2.1: Independent reference scales	21
Table 2.2: Dependent reference scales.	25
Table 2.3: Main dimensionless parameters.	26
Table 2.4: Derived dimensionless parameters.	26
Table 2.5: Variables parameters.	27
Table 2.6: Dimensionless equations	27
Table 3.1: Geometrical parameters.	37
Table 3.2: Electromagnetic parameters	38
Table 3.3: MHD equations.	39
Table 3.4: Vector parameters of Navier Stokes equation	39
Table 3.5: Continuity equation	40
Table 3.6: Navier Stokes equations	40
Table 3.7: Magnetic Induction equations	41
Table 3.8: Simplification of Magnetic Induction equations.	42
Table 3.9: Boundary condition of Vector Potentials of Velocity.	53
Table 3.10: Constant parameters of system.	56
Table 3.11: Tests results.	59
Table 3.12: Constant dimension parameters.	60
Table 3.13: Dimension and dimensionless variables.	60
Table 3.14: Parameters in the tests	61
Table 3.15: Test results	63
Table 3.16: Main parameters of test	73
Table 3.17: Values of the duct height	73
Table 3.18: Test results	75
Table 3.19: Evolution of critical value of N with the height of domain.	76
Table 3.20: Main parameters of the test	79
Table 3.21: Test results.	80
Table 3.22: Main parameters of the test	83
Table 3.23: Test results	83

Table 3.24: Main parameters of the test.	86
Table 4.1: Properties of solar wind	96
Table 4.2: Main fluid dynamic parameters	104
Table 4.3: Values of dimensionless parameters in the inflation of the sail	104
Table 4.4: Geometrical parameter.	110
Table 4.5: Parameter of plasma and solar wind	110
Table 4.6: Reynolds number in the solar wind	110
Table 4.7: Values of the resulting thrust.	112
Table 4.8: Dimensional and dimensionless parameters in the previous FEM simulation	114
Table 4.9: Dimensionless parameters	115
Table 4.10: New parameters after change of velocity.	115
Table 4.11: New parameters after change of Magnetic field	116
Table 4.12: New parameters after change of density.	116
Table 5.1: Summary of boundary conditions of magnetic induction field	122

Thesis outline

The thesis is organized as follows.

In the Chapter I, an introduction on the Fundamentals of Magnetohydrodynamic is reported.

In the Chapter II, the general equations of Magnetohydrodynamics are first introduced, and then in the successive paragraphs, the non-dimensional formulation specific for the present study is deduced. This leads to define the functioning regime in terms of four non-dimensional parameters, namely Reynolds number, magnetic Reynolds number, Hartman number, and interaction parameter, which completely characterize the process.

In the Chapter III, the problem of the cylinder swept by a plasma inside a magnetic field is analyzed in detail. Firstly, all the involved phenomena are introduced, putting in evidence the main parameters that describe the process. Secondly, the literature on the problem at hand is briefly described. Third, the numerical model developed in this study is described in detail, and then the results are shown and commented.

In the Chapter IV, the results of the previous study are exploited for the analysis of the Magnetic Plasma Sails. In particular, the conditions for plasma deviation in order to inflate the sail are assessed, and the calculation of the thrust exerted by the wind on the spacecraft is determined.

The Conclusion ends this dissertation.

1 Fundamentals of MHD

1.1 Introduction

The Magneto-Hydro-Dynamics (MHD) is the discipline that studies the interaction between conductive fluids and applied magnetic fields. In almost all cases, the fluid is the seat of a velocity field that, interacting with a magnetic field, generates an electrical current and then Laplace forces.

The MHD area includes phenomena on the astrophysical scale (solar activities, solar wind, earth magnetic field, etc.) and phenomena at laboratory scales and industrial applications (pumping, electrical generator, materials processing, nuclear fusion, etc.). It incorporates all the phenomena of both Fluid Dynamics and Magnetism, but new phenomena arise due to the interaction between magnetic field and operating fluid.

Ever since its beginnings, MHD always aroused interest in Industry due to its feature to perform processes without any solid moving parts and that the forces can be applied without mechanical contacts. All applications share the general equations system, which can be used to describe phenomena totally different among them. Nevertheless, due to the complexity of the model, the actual possibility to solve the system for a specific case strongly depends on the approximations that one introduces in the model.

The conductivity of operating fluid is one of the most important properties of an MHD system, because it determines the level of electrical current and finally the electromagnetic forces. The main types of conductive fluids suitable for MHD applications are:

1. Liquid metals
2. Electrolytes
3. Plasmas

In Table 1.1 some conductivity values of fluids are shown, compared with the values of solid conductors. It can be seen that the distilled water has an extremely low conductivity. In fact, the conduction of the electric current in the water is due to the salts dissolved in it. Non distilled water can be considered a weak electrolyte, therefore with a very low conductivity. In case of strong electrolytes, such as salt water and sulfuric acid, the scale changes significantly. Following in the table, the real plasmas are listed, such as molten glass (1400 [°C]), cold plasmas (around 10 000 [K]), then the hot plasmas (around 10^6 [K]), until the gases are completely ionized, with

values of conductivity higher and higher. It can be seen also that totally ionized gases are much more conductivity than copper.

Table 1.1: Conductivity values of some fluids

Material	$\sigma [\Omega^{-1}m^{-1}]$
Distilled water	10^{-4}
Weak electrolyte	$10^{-4} \div 10^{-2}$
Strong electrolyte	$10^{-2} \div 10^2$
<i>Water +25% NaCl (20°C)</i>	21.6
<i>Sulphuric acid (20°C)</i>	73.6
Molten glass (1400°C)	$10 \div 10^2$
Cool plasma ($10^4 K$)	10^3
Hot plasma ($10^6 K$)	10^6
Totally ionised gas	$10^7 \cdot T^{3/2}$
Liquid metals	$10^6 \div 10^7$
- <i>Steel (1500°C)</i>	$0.7 \div 10^6$
- <i>Mercury (20°C)</i>	10^6
- <i>Aluminum (700°C)</i>	$5 \cdot 10^6$
- <i>Sodium (400°C)</i>	$6 \cdot 10^6$
Solid metals	$10^6 \div 10^8$
- <i>Steel (20°C)</i>	10^6
- <i>Sodium (20°C)</i>	10^7
- <i>Copper (20°C)</i>	$6 \cdot 10^7$

This first part of study concerns a liquid with high electrical conductivity.

Liquid metals also have a very high conductivity, although less than the typical values of the same material in solid state. For this reason, great attention is payed to liquid metals, both as regards the production processes of the material itself, and for its use as operating fluid in energy conversion.

An important simplification of the set of MHD equations for liquid concerns the incompressibility. At the same time, the homogeneity and the isotropy of properties such as magnetic permeability, electrical conductivity and viscosity, also considerably reduce the complexity of the model.

The simplification of the model plays a fundamental role in the numerical simulation, which is mandatory in the study of any real-case problem. Regarding this aspect, several commercial Finite Elements Method (FEM) software have been recently equipped with the Multi-Physics approach, which consists in embedding in the same model all the Physics involved in the phenomenon, which are not limited to the Fluid-dynamics and Magnetism only, but also the thermic, chemical and other aspects are considered. In general, the complexity of the model gives rise to numerical instabilities,

which means that often, providing a good approximation of the final solution as starting solution is mandatory to allow the numerical model to converge.

In this thesis, an important paradigm of MHD is analysed, which consists in a liquid metal flowing in a concurrent magnetic field and encountering a cylindrical obstacle. Depending on the nature of the fluid and the functioning regime, this simple system could represent the gold electroplating very important in connecting industry, or a vehicle traveling in a conducting medium, or other different systems. On the other hand, some flow meters are based on the frequency analysis of the Von Karman street. Furthermore, this simple system is also an element of fundamental research in the sense that many phenomena can be identified as for example reduction of instabilities, Alfvén waves, two-dimensionalization of the flow, etc.

In the absence of the magnetic field, in laminar conditions the fluid downstream the obstacle evolves with the typical Von Karman street, which is formed by vortices that originate from the surface of the cylinder with a constant frequency, depending on the operating conditions. It is worth to pointing out that this kind of regime, although dynamical, is not turbulent, as the streamlines of the flow can be defined. On the contrary, upstream the obstacle, the regime of the flow is not affected by the obstacle, excepted for a thin boundary layer on the surface. If an external magnetic field is applied, the behavior of the fluid changes, depending on the parameters of the phenomenon. In particular, when the magnetic field is concurrent with the flow, it tends to reduce the vortices, as a consequence of the eddy currents generated in the fluid by the interaction between the magnetic field and the local component of the velocities orthogonal to that of the undisturbed flow.

Another interesting phenomenon occurring in this setup is that of Alfvén's waves. These are perturbations of the magnetic field producing perturbation of the velocity. The finding of such waves has aroused a great deal of interest during 50th of the past century, mainly for their application in telecommunications. The propagation velocity of these waves depends on the intensity of the induction field, on the magnetic permeability of the medium; therefore one of the most interesting aspects is related to the possibility to modulate the propagation velocity. In the setup considered in the present study, the Alfvén's waves can be observed only within a range of values of the applied magnetic field.

In this thesis, a numerical analysis of the above described setup is performed. The nondimensional analysis is assumed. The study is compared with experimental studies retrieved from the literature. In all these cases, all the involved phenomena are analyzed in detail, in particular the effects of the magnetic field on the fluid dynamic regime, and the dragging force.

The second part of the thesis is applied to the study of a problem of interest for Aerospace that concerns a system of propulsion called magneto-plasma solar sails. This system exploits the solar wind in a similar principle that sailboat which uses the wind in the Earth.

The solar wind is characterized by high velocity of ionized gas (hydrogen plasma), of mean value 500 [km/s] at 1 [AU] of distance from the sun, but very low density (12 particles/cm³). In the hypothesis of a direct use of this wind and in order to obtain a sufficient thrust (of order of 1 Newton), the size of the sail has to be of the order of tens of kilometers.

Independently on the technical problems for the deployment of the sail and its resistance against the bodies that hit on it, a large sail corresponds to a large mass, at the expenses of the obtainable acceleration. The magnetic solar sails represent a brilliant alternative, as the material sail is substituted by a magnetic field. In fact, the solar wind is formed by completely ionized material, namely protons and ions alone, therefore their trajectory can be modified by a magnetic field. This field can be created by a very large coil, but the problems of deploying the sail and its mass still remain. A more efficient solution is represented by the plasma sails. In this case the coil is substituted by a cloud of plasma circulating around the spacecraft. In this way, the technical aspects related to the mass and the deployment are avoided, but many aspects remain to clarify, such as the inflation of the cloud of plasma and its interaction with the solar wind. The detailed understanding of all the phenomena occurring in the magnetic solar sails is far beyond the scope of this study, but it is worth to show how the paradigm of the cylinder could be applied in this case. In particular, the process of inflating the sail and the assessment of the obtainable thrust are analyzed.

2 MHD equations

2.1 General form of MHD equations

The MHD applications are governed by fluid dynamics equations combined with the Maxwell's equations. The Ohm's law characterizes the electrical behaviour of the fluid. In general, in MHD the operating fluid is assumed electrically neutral, and the time constants allow to neglect the influence of the displacement current. Furthermore, by adopting an operating fluid in liquid phase, a relevant simplification ensues. In the first part of this dissertation, the working fluid is assumed to be a liquid metal. The differences in the formulation deriving from different hypotheses will be introduced where necessary. In the light of the above, the MHD processes are governed by the main following equations:

- Navier-Stokes Equation:

$$\rho \frac{\partial \mathbf{V}}{\partial t} = -\nabla P + \mu_d \nabla^2 \mathbf{V} + \mathbf{J} \times \mathbf{B} \quad (2.1)$$

The term ρ is the fluid density and \mathbf{V} the vector velocity, P is the pressure, μ_d is the fluid dynamic viscosity and, finally, $\nabla^2 \mathbf{V}$ is the Laplacian of the velocity vector. \mathbf{J} is the current density, and \mathbf{B} is the magnetic induction field. The last addend is the Laplace volume force, and it is responsible of the coupling between the fluid dynamic and magnetic phenomena.

- Continuity equation:

$$\frac{\partial \rho}{\partial t} + \nabla \cdot (\rho \mathbf{V}) = 0 \quad (2.2)$$

that for liquids ($\rho \equiv \text{const}$) becomes:

$$\nabla \cdot \mathbf{V} = 0 \quad (2.3)$$

- The Maxwell's equations:

$$\nabla \times \mathbf{E} = -\frac{\partial \mathbf{B}}{\partial t} \quad (2.4)$$

$$\nabla \cdot \mathbf{B} = 0 \quad (2.5)$$

where \mathbf{E} is the electrical field.

$$\nabla \times \mathbf{B} = \mu \mathbf{J} \quad (2.6)$$

- The local form Ohm's law:

$$\mathbf{J} = \mathbf{qV} + \sigma(\mathbf{E} + \mathbf{V} \times \mathbf{B}) \quad (2.7)$$

resulting simplified by limiting the study to the case of no free charge:

$$\mathbf{J} = \sigma(\mathbf{E} + \mathbf{V} \times \mathbf{B}) \quad (2.8)$$

where σ is the electrical conductivity.

- Equation of Magnetic Induction:

$$\frac{\partial \mathbf{B}}{\partial t} = \nabla \times (\mathbf{V} \times \mathbf{B}) + \frac{1}{\mu\sigma} \nabla^2 \mathbf{B} \quad (2.9)$$

that comes by combining the Maxwell's equations (2.4) and (2.6), with the Ohm's law (2.7).

Below are the other equations used in the first part of this work.

- Equation of Continuity of Current

$$\nabla \cdot \mathbf{J} = 0 \quad (2.10)$$

that derives by the equation (2.7), with the assumption of isotropic and homogeneous permeability.

- Vector potential equation

$$\mathbf{B} = \nabla \times \mathbf{A} \quad (2.11)$$

2.2 The Non-Dimensional Analysis

In this section, the non dimensional form for the equations involved in the model is deduced by considering the physical quantities reported in **Errore. L'origine riferimento non è stata trovata.**1 as reference scales.

Table 2.1: Independent reference scales

Symbol	Description	Unit	Reference value
V_0	Reference velocity	[m/s]	independent
D	Reference length	[m]	independent
B_0	Reference magnetic field	[T]	independent
t_0	Reference time	[s]	D/V_0
ρ_0	Reference density	[kg/m ³]	$\sigma B_0^2 D_0 / V_0$

In Table 2.1 the symbol σ represents the electrical conductivity of the fluid, which is assumed to be isotropic. In the following, the symbols in bold represent vector quantities.

2.2.1 Navies-Stokes equation

$$\rho \frac{\partial \mathbf{V}}{\partial t} = -\nabla P + \mu_d \nabla^2 \mathbf{V} + \mathbf{J} \times \mathbf{B} \quad (2.1)$$

In equation (2.1) \mathbf{V} , ρ and P are respectively the fluid velocity, *density* and pressure, μ_d is the dynamic viscosity, t is the time, \mathbf{J} is the electrical current density and \mathbf{B} is the magnetic field. The Navier-Stokes equation can be reformulated considering the *normalized variables*:

$$\rho = \rho_0 \rho', \quad \mathbf{V} = V_0 \mathbf{V}', \quad P = P_0 P', \quad \mathbf{J} = J_0 \mathbf{J}', \quad \mathbf{B} = B_0 \mathbf{B}', \quad t = t_0 t'$$

The prime symbols indicate the normalized variables, and the subscript "0" indicates the reference values. On these assumptions, the (2.1) writes:

$$\rho' \rho_0 \frac{\partial (V_0 \mathbf{V}')}{\partial (t_0 t')} = -\frac{1}{D} \nabla (P_0 P') + \frac{1}{D^2} \mu_d \nabla^2 (V_0 \mathbf{V}') + J_0 \mathbf{J}' \times B_0 \mathbf{B}' \quad (2.11)$$

By dividing by $\frac{\rho_0 V_0}{t_0}$ and considering the reference expression of the time t_0 (see Table 1), the following form is obtained:

$$\rho' \frac{\partial (\mathbf{V}')}{\partial (t')} = -\frac{P_0}{\rho_0 V_0^2} \nabla (P') + \frac{\mu_d}{D \rho_0 V_0} \nabla^2 (\mathbf{V}') + \frac{J_0 B_0 D}{\rho_0 V_0^2} (\mathbf{J}' \times \mathbf{B}') \quad (2.12)$$

In order to make the (2.12) formally identical to (2.1), using the reference expressions reported in Table 1, the following relations have to be fulfilled:

$$\begin{aligned} \frac{P_0}{\rho_0 V_0^2} = 1 &\Rightarrow P_0 = \rho_0 V_0^2 \\ \mu_d' = \frac{\mu_d}{D \rho_0 V_0} = \frac{\mu_d V_0}{\sigma B_0^2 D^2} = \frac{V_0}{Ha^2} \\ \frac{J_0 B_0 D}{\rho_0 V_0^2} = 1 &\Rightarrow J_0 = \frac{\rho_0 V_0^2}{B_0 D} = \sigma B_0 V_0 \end{aligned} \quad (2.13)$$

where $Ha = B_0 D \sqrt{\frac{\sigma}{\mu_d}}$ is the dimensionless Hartmann's number (see below). The last assumption exploits one degree of freedom to define a relation that will be useful below.

2.2.2 The continuity equation (incompressible fluid)

The continuity equation for incompressible fluid does not need to define new parameters:

$$\nabla \cdot \mathbf{V}' = 0 \quad (2.14)$$

2.2.3 Vector potential equation

$$\mathbf{B} = \nabla \times \mathbf{A} \quad (2.3)$$

In equation (2.3) the magnetic field \mathbf{B} is defined in terms of magnetic potential vector \mathbf{A} .

By imposing $\mathbf{B} = B_0 \mathbf{B}'$ and $\mathbf{A} = A_0 \mathbf{A}'$, and considering the length D that derives by non-dimensional rotor, the (2.3) writes:

$$\frac{B_0 D}{A_0} \mathbf{B}' = \nabla \times \mathbf{A}' \quad (2.15)$$

from which the condition for the formal equivalence between (2.3) and (2.15) is:

$$\frac{B_0 D}{A_0} = 1 \Rightarrow A_0 = B_0 D \quad (2.16)$$

2.2.4 Ohm's law

$$\mathbf{J} = \sigma(\mathbf{E} + \mathbf{V} \times \mathbf{B}) \quad (2.4)$$

The generalized Ohm's law becomes a non-dimensional equation by imposing $\mathbf{J} = J_0 \mathbf{J}'$, $\sigma = \sigma_0 \sigma'$, $\mathbf{V} = V_0 \mathbf{V}'$, $\mathbf{E} = E_0 \mathbf{E}'$ and $\mathbf{B} = B_0 \mathbf{B}'$. The following equation is then obtained:

$$J_0 \mathbf{J}' = \sigma_0 \sigma' (E_0 \mathbf{E}' + V_0 \mathbf{V}' \times B_0 \mathbf{B}') \quad (2.17)$$

then, by assuming $E_0 = V_0 B_0$:

$$\mathbf{J}' = \frac{V_0 B_0 \sigma_0}{J_0} \sigma' (\mathbf{E}' + \mathbf{V}' \times \mathbf{B}') \quad (2.18)$$

which is formally equal to (2.4) provided that:

$$V_0 B_0 \sigma_0 = J_0 \quad (2.19)$$

2.2.5 Faraday-Neumann-Lenz equation

$$\nabla \times \mathbf{E} = -\frac{\partial \mathbf{B}}{\partial t} \quad (2.5)$$

The electromagnetic induction phenomenon is described by the equation (2.5) where \mathbf{E} is the electrical field. By imposing $\mathbf{E} = E_0 \mathbf{E}'$ and $\mathbf{B} = B_0 \mathbf{B}'$ the (2.5) writes:

$$\frac{1}{D} \nabla \times (E_0 \mathbf{E}') = -\frac{\partial (B_0 \mathbf{B}')}{\partial (t_0 t')} \Rightarrow \frac{E_0 t_0}{D B_0} \nabla \times \mathbf{E}' = -\frac{\partial \mathbf{B}'}{\partial t'} \quad (2.20)$$

from which, the condition for the formal equivalence between (2.5) and (2.20) is:

$$\frac{E_0 t_0}{DB_0} = 1 \Rightarrow \frac{E_0}{B_0 V_0} = 1 \Rightarrow E_0 = B_0 V_0 \quad (2.21)$$

2.2.6 Ampère's law

$$\nabla \times \mathbf{B} = \mu_0 \mu_r \mathbf{J} \quad (2.6)$$

where μ_0 is the vacuum permeability and μ_r the relative permeability of the mean. Let assume $\mathbf{J} = J_0 \mathbf{J}'$, $\mathbf{B} = B_0 \mathbf{B}'$. The (2.6) writes:

$$\frac{1}{D} \nabla \times B_0 \mathbf{B}' = \mu_0 \mu_r J_0 \mathbf{J}' \quad (2.22)$$

which becomes formally equal to (2.6) by defining:

$$\mu'_0 = \mu_0 \frac{DJ_0}{B_0}. \quad (2.23)$$

Taking into account the equivalence condition (2.13):

$$\mu'_0 = DV_0 \sigma_0 \mu_0 = R_m \quad (2.24)$$

where R_m is the Magnetic Reynolds number. It can be demonstrated that it is equal to the ratio between the two terms in the right-hand side of the equation of magnetic induction (2.10), which represent respectively the advection term and the diffusion term of the magnetic field. The advective term is negligible and the magnetic field propagates by diffusion effect, without being affected by the velocity field, when $R_m \ll 1$. The diffusive term is negligible, and the streamlines of the magnetic field are determined by the velocity field when $R_m \gg 1$. This second operative condition is defined as *frozen condition*.

2.2.7 Continuity equations

The non-dimensional expressions of the continuity of both current density and the magnetic field maintain the same form of the dimensional ones, without the need to state new assumptions:

$$\nabla \cdot \mathbf{J}' = 0; \quad \nabla \cdot \mathbf{B}' = 0 \quad (2.25)$$

2.2.8 Equation of the Magnetic Induction

$$\frac{\partial \mathbf{B}}{\partial t} = \nabla \times (\mathbf{V} \times \mathbf{B}) + \frac{1}{\mu\sigma} \nabla^2 \mathbf{B} \quad (2.10)$$

Also in this case, the equation can be reformulated considering the normalized variables:

$$\mathbf{B} = B_0 \mathbf{B}' \quad \mathbf{V} = V_0 \mathbf{V}', \quad t = t_0 t'$$

$$\frac{\partial \mathbf{B}_0 \mathbf{B}'}{\partial t_0 t'} = \frac{1}{D} \nabla \times (\mathbf{V}_0 \mathbf{V}' \times \mathbf{B}_0 \mathbf{B}') + \frac{1}{\mu \sigma D^2} \nabla^2 \mathbf{B}_0 \mathbf{B}' \quad (2.26)$$

and then, dividing by B_0/t_0 and considering the reference expression of the time $t_0 = D/V_0$, one obtains:

$$\frac{\partial \mathbf{B}'}{\partial t'} = \nabla \times (\mathbf{V}' \times \mathbf{B}') + \frac{1}{R_m} \nabla^2 \mathbf{B}' \quad (2.27)$$

The equation (2.27) does not need new assumptions to be formally identical to the equation of the magnetic induction (2.10), as this result is obtained as a consequence of the previous definitions.

In Table 2.2 the dependent quantities used as reference scales are reported.

Table 2.2: Dependent reference scales.

Symbol	Description	unit	Reference value
P_0	Reference pressure	[Pa]	$\rho_0 V_0^2$
J_0	Reference density current	[A/m ²]	$\frac{\rho_0 V_0^2}{B_0 D} = \sigma_0 B_0 V_0$
σ_0	Reference conductivity	[S/m]	σ
E_0	Reference electric field	[C/m]	$B_0 V_0$
A_0	Reference magnetic vector potential	[V · s/m]	$B_0 D$

2.3 Non-dimensional numbers: fundamental aspects and applications

The non-dimensional equations allow one to extend the validity of a study to the entire class of systems that share the same non-dimensional parameters. The MHD dimensionless equations involves three independent non dimensional parameters, they are

- **Reynolds number**

$$R_e = \frac{\rho V D}{\mu_d} \quad (2.27)$$

where: μ_d is the dynamic viscosity of fluid. This number represents the ratio between inertia and viscous forces, and it is the main reference to establish if a fluid-dynamic regime is laminar or turbulent.

- **Magnetic Reynolds number**

$$R_m = \mu \sigma V D \quad (2.28)$$

- **Interaction parameter**

$$N = \frac{\sigma B_0^2 D}{\rho V} \quad (2.29)$$

This number represents the ratio between electromagnetic and inertia forces. A high value of this parameter implies that the magnetic field acts on the velocity fields significantly.

These three dimensionless numbers control completely the physics of the MHD problem.

Two other important dimensionless numbers, combination of the three above nondimensional number, are the following:

- **Alfvén number**

$$\alpha = \frac{V}{v_a} \quad (2.30)$$

represents the ratio between the fluid velocity V and the Alfvén's velocity $v_a = B/\sqrt{\rho\mu}$. This number that characterizes the propagation of the small magnetic disturbance is such as:

$$\alpha^2 = R_m/N \quad (2.31)$$

- **Hartmann number**

$$Ha = B_0 D \sqrt{\frac{\sigma}{\mu_d}} = \sqrt{N Re} \quad (2.32)$$

The Hartmann number represents the ratio between magnetic and viscous forces.

Table 2.3: Main dimensionless parameters.

Name parameter	Reynolds number Re	Magnetic Reynolds number R_m	Interaction parameter N
Definition	$\frac{D\rho V}{\mu_d}$	$DV_0\sigma_0\mu_0$	$\frac{\sigma B_0^2 D}{\rho V_0}$

Table 2.4: Derived dimensionless parameters.

Name parameter	Alfvén number	Hartmann number Ha
Definition	$\alpha = \frac{V}{v_a}$	$B_0 D \sqrt{\frac{\sigma}{\mu_d}}$

Table 2.5 gives the dimensionless form for each physical parameter involved in the model, and the Table 2.6 is the dimensionless form of MHD equations

Table 2.5: Variables parameters.

Name parameter	Normalized density	Normalized dynamic viscosity	Normalized electrical conductivity	Normalized vacuum permeability
Definition	$\rho' = \frac{\rho}{\rho_0} = \frac{\rho}{\frac{\sigma B_0^2 D}{V_0}}$ $= \frac{\rho V_0}{\sigma B_0^2 D} = \frac{1}{N}$	$\mu_d' = \frac{\mu_d}{D \rho_0 V_0} =$ $= \frac{\mu_d V_0}{\sigma B_0^2 D^2} = \frac{V_0}{Ha^2}$	$\sigma' = \frac{\sigma}{\sigma_0} = 1$	$\mu_0' = R_m$

Table 2.6: Dimensionless equations

Name equation	Expression
Navies Stokes equation	$\rho' \frac{\partial(\mathbf{V}')}{\partial(t')} = -\nabla(P') + \frac{1}{Re} \nabla^2(\mathbf{V}') + N(\mathbf{J}' \times \mathbf{B}')$
Continuity equations	$\nabla \cdot \mathbf{J}' = 0; \quad \nabla \cdot \mathbf{B}' = 0$
Magnetic Induction equation	$\frac{\partial \mathbf{B}'}{\partial t'} = \nabla \times (\mathbf{V}' \times \mathbf{B}') + \frac{1}{R_m} \nabla^2 \mathbf{B}'$

3 MHD flow analysis of a conductive fluid around a cylinder

3.1 General aspects

The motion of the fluids around obstacles is a very important phenomenon that involves many Physical aspects. Such motions concern ocean current, air circulation, solar wind, at industrial applications: aerospace, energy conversion systems, energy production systems, a fluid, gaseous or liquid, interacting with obstacles of any shape.

The study of hydrodynamics around obstacles, pressure distribution, formation of vortices and interference with the obstacle and the magnetic field, are some examples that deserve the present study. In this work, a numerical model of a cylindrical obstacle swept by liquid metal submitted to the influence of magnetic field has been developed and studied as a paradigm for more complex MHD systems.

The Fluid-Dynamic model consists of a two-dimensional domain representing a duct, which contains a liquid metal moving around a cylindrical obstacle. A magnetic field is applied to the entire domain induced by two sheets of currents such that the magnetic streamlines of the field have the same direction of the velocity of undisturbed fluid flow. The choice of the two-dimensional model aims to reduce the computational burden. On the other hand, this kind of model introduces important approximations with respect to a more realistic three-dimensional one. The axisymmetric model is not suitable, because the problem at hand does not have this property.

In general, when a fluid encounters an obstacle, its flow configuration changes in function of the shape of the obstacle, its size, the fluid properties If a magnetic field is applied to such a system, the flow configuration is modified in function of the intensity and direction of the magnetic field. The interaction generates Lorentz's Forces by the way of the induced currents. The magnetic properties of the obstacle are also important parameters of the process in the sense that they can modify the applied magnetic field distribution.

In the following, the main assumptions in the model development are highlighted, and the numerical results are compared with the theory and the experimental results retrieved from the literature.

3.2 Fluid dynamic analysis

3.2.1 Types of motion

The main physical properties used in this study are *Compressibility*, *Density* ρ [kg/m^3], and *Viscosity* μ [$Pa \cdot s$].

Generally speaking, the fluid flow can be laminar or turbulent.

The regime is laminar if the current can be subdivided into thin layers, so that the stream lines never cross the faces of the layers. In this regime, the velocity can change in space and time. These changes may also depend on global geometry or modifications of external conditions (e.g. pressure, forces, etc.).

The motion of a fluid is turbulent if the stream lines have irregular course in time and space. Physical kinematic quantities (position, speed, and acceleration), dynamics (pressures, tangential stresses) and thermal (temperature, thermal flows) vary in time and space without precise laws.

3.2.2 Reynolds number

The Reynolds number is of great importance in Fluid-dynamics. The term comes from the mathematician and engineer Osborne Reynolds (1883), which expresses the dependence of the motion type, laminar or turbulent, from the velocity of the fluid, its density, dynamics viscosity and diameter D of the pipe in which is flowing the fluid.

$$R_e = \frac{\rho V D}{\mu} \quad (3.1)$$

Experiments conducted by Reynolds also showed that there is not a precise value of this parameter at which the motion shift from laminar to turbulent, but there is a range of transition values of the number R_e , whose width could depend on the experimental conditions. In general:

- for $R_e < 2000$ the motion is *laminar*
- for $R_e > 4000$ the motion is *turbulent*

The study of the motion in the transition zone is in general troublesome.

Also, the modality of the test could affect the movement. For example, replicating the experience of Reynolds, starting from $R_e < 2000$ and increasing the velocity of flow gradually without any disturbances, it is possible to achieve a laminar motion for values of R_e significantly greater than 4000.

3.2.3 Vortex Shedding

In the problem under study, downstream the obstacle and even for small Reynolds numbers, the flow exhibits the formation of vortices that constitute the characteristic von Karman streets [1]. For a wide range of the Reynolds number, the regime of the vortices is laminar. The vortices originate from the sides of the obstacle, with a characteristic rate related to the parameters of the experimental setup. The detachment of vortices is a very complex and widely studied phenomenon [1]. In fact, the presence of the wake due to the take off the boundary layer is responsible for the resistance that the objects oppose to the flow; in the obstacles with aerodynamic shape, the flow tends to follow the body profile and do not exhibit streets of vortices [2].

When the body shape is stocky (squat bodies), the flow separates from the object and vortices are formed. In particular, when a fluid hits a bluff body, like a cylindrical obstacle, their interaction gives rise to the flow separation. The separation takes place within the boundary layer, where the viscous effects are predominant and the tangential efforts determine high velocity gradients. The current, near the wall, does not have sufficient inertia to overcome the adverse pressure gradient; therefore it is not able to follow the surface of the body in the posterior region. In these conditions, a wake downstream of the object is generated, which is characterized by recirculation of flow and the formation of vortices, which detach from the body.

The point of separation of the vortices is not constant but it depends on the type of boundary layer that develops near the surface of the cylinder, which depends on the Reynolds number. In Fig. 3.1 the separation of the flow, for a circular section is shown [3].

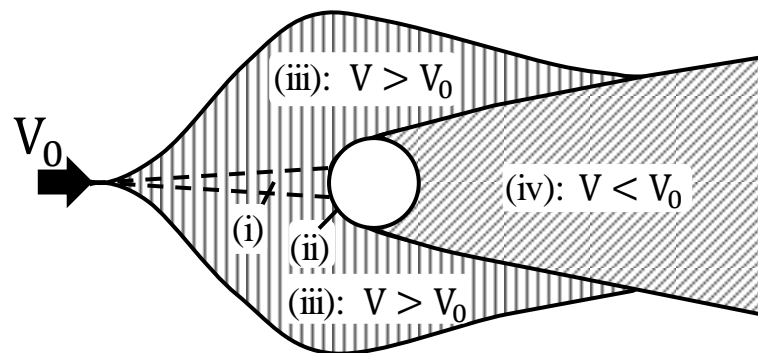


Figure 3.1: Flow separation from a fixed cylinder [3]

Close to the cylinder, four zones with different characteristics are identified

- i. : Flow retarded
- ii: Boundary layer

iii: Accelerated flow

iv: Wake region

Vortex Shedding phenomenon is governed essentially by the Reynolds number which controls the weak and so the Strouhal number (see paragraph 3.2.4). Other factors, not related to fluid-dynamics, which modify the system, may be present, like the roughness of cylinder, and the distance from the back wall characterized by the confinement ratio. Referring to literature, various types of regimes can be defined (Fig. 3.2).

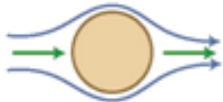

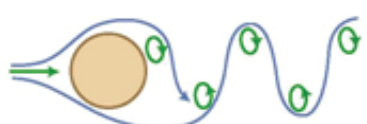
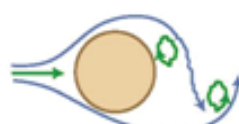
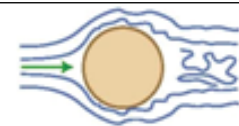
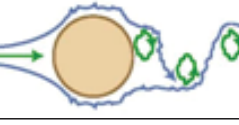
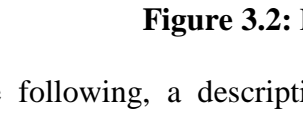
	$Re < 5$	Regime of unseparated flow
	$5 - 15 < Re < 40$	A fixed pair of vortices in wake SUBCRITICAL
	$40 < Re < 150$	Two regimes in which vortex street is laminar SUBCRITICAL
	$150 < Re < 300$ Transition to turbulence	Transition range to turbulence in vortex street SUBCRITICAL
	$300 < Re < 3 \cdot 10^5$	Vortex street is fully turbulent SUBCRITICAL
	$3 \cdot 10^5 < Re < 3 \cdot 10^6$	Laminar boundary has undergone turbulent transition and wake is narrower and disorganized TRANSCRITICAL
	$3 \cdot 10^6 < Re$	Re-establishment of turbulent vortex street UPPER-TRANSCRITICAL

Figure 3.2: Flow on a circular cylinder with a smooth wall [4].

In the following, a description of the main parameters governing the Von Karman streets behavior is given.

3.2.4 Trochal number

The rate at which the vortices are produced has a frequency f [Hz] equal to:

$$f = \frac{St \cdot D}{v_m} \quad (3.2)$$

where:

S_t is the Strouhal number.

D is the diameter of cylinder

V_m is the undisturbed velocity value

The Strouhal number is a dimensionless parameter that depends on both the fluid-dynamic regime and the shape of the obstacle. Within certain intervals of values of the Reynolds number, for any shape of obstacle, it is possible to define a relation between the Strouhal and the Reynolds numbers. Generally, and especially when the range of Reynolds number is wide, the values of S_t have to be determined experimentally. In Fig. 3.3, the diagram of S_t versus Re is shown. As it can be seen, for very high values of the Reynolds number, the determination of the Strouhal number is affected by high uncertainty.

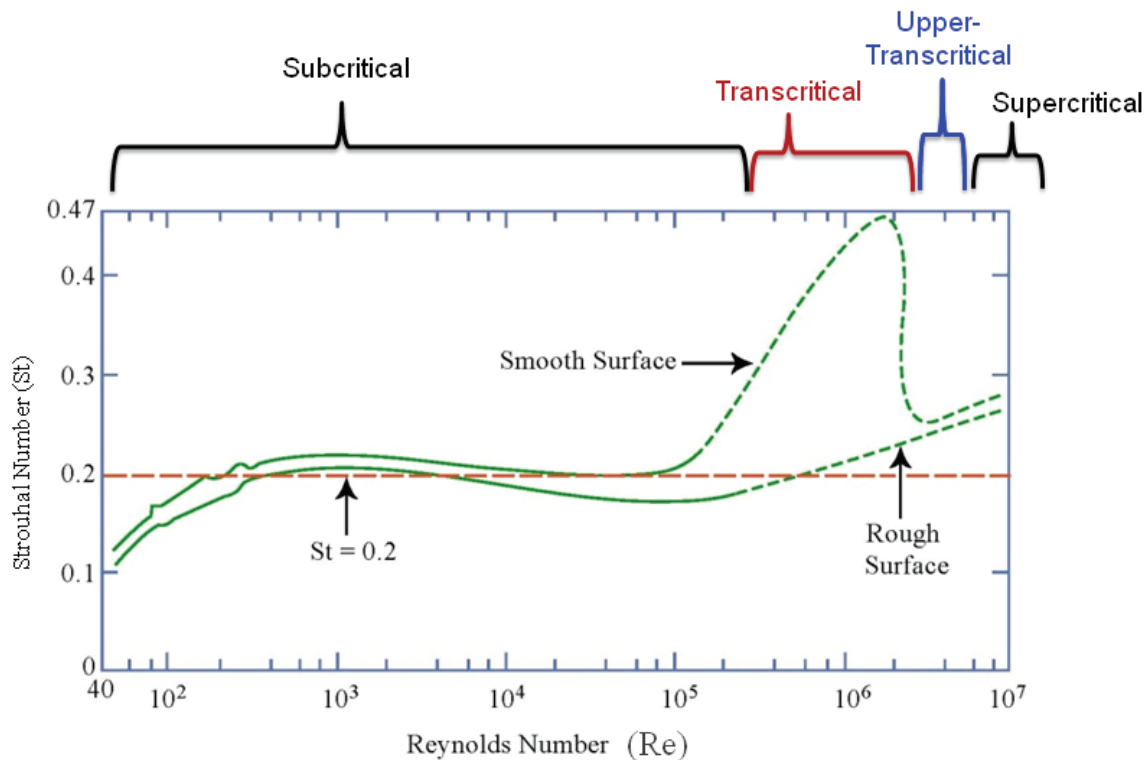


Figure 3.3: Strouhal number vs Reynolds number [5]

In Fig. 3.4, the comparison of Strouhal number versus Reynolds number for unbounded flow around a circular cylinder with different results in the literature is reported [6].

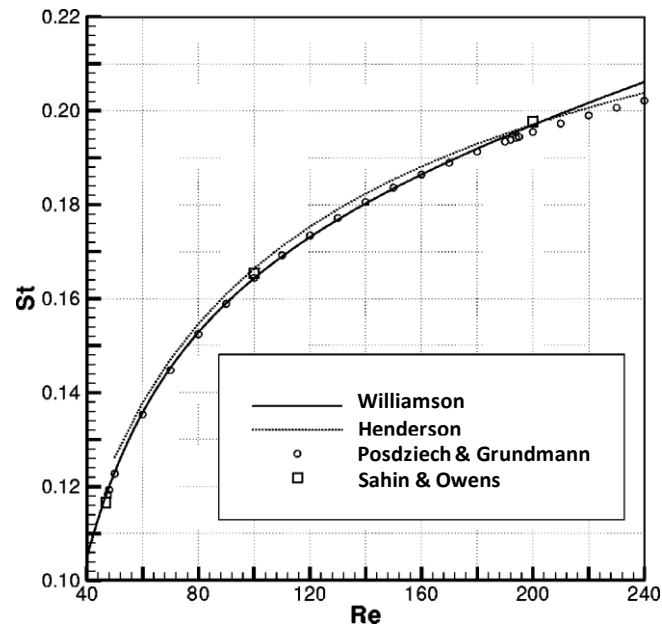


Figure 3.4: Comparison of Strouhal number versus Reynolds number for unbounded flow around a circular cylinder with different results in the literature: (—), experimental work of Williamson [7]; (...), numerical results of Henderson [8]; (○), numerical results of Posdziech and Grundmann [9]; (□) numerical results of Sahin and Owens [6].

3.2.5 Detachment point

The position where the boundary layer takes off from the obstacle is shown on Fig. 3.5 where the dependency with Reynolds number is represented for one cylinder.

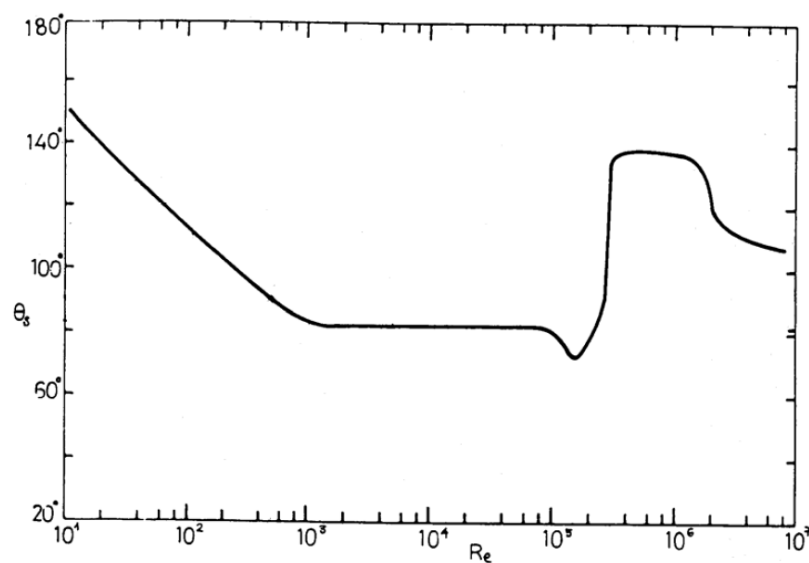


Figure 3.5: Diagram of the angle of detachment vs the Reynolds number [10] [11]

The angle of detachment is of great importance in the resistance of the obstacle to the flow, as it strongly affects the integral of the pressure along the profile of the surface. It can be noticed that the Strouhal number varies almost linearly for values of Reynolds number less than 1000, which is the range of interest of this study.

3.2.6 Dragging Force

The drag force is given principally by the difference of pressure between upstream and downstream the object, and for another part by the friction around the obstacle.

In a streamlined body, such as an airfoil, the stream of fluid tends to remain attached to the profile, and then the difference of pressure can be neglected. Therefore, the tangential forces provide the main contribution of the resistance force. In squat bodies, such as the cylinder and the sphere, the resistance of shape due to the difference in pressure is considerable and the tangential forces are negligible.

The Resistance Force or *Dragging Force* is a force parallel to the velocity of incident flow:

$$F_d = \frac{1}{2} C_d \rho V^2 S \quad (3.3)$$

where C_d is the drag coefficient, ρ is the density of fluid, V is the velocity of fluid, S is the front area of the object. Let P_θ indicate the pressure on the surface of the cylinder in function of the angular position, and dF the Pressure force exerted on an element dS of surface. One can write:

$$dF = P_\theta dS \mathbf{n} \quad (3.4)$$

Where \mathbf{n} is the unit vector perpendicular to the surface of the cylinder.

The component of the drag force in the direction of the velocity field writes:

$$F_d = \int_0^{2\pi} P_\theta R \cos\theta d\theta \quad (3.5)$$

where R is the radius of cylinder.

By combining (3.3) and (3.5), the expression of the drag coefficient C_d is obtained:

$$C_d = \frac{\int_0^{2\pi} P_\theta R \cos\theta d\theta}{\rho V^2} \quad (3.6)$$

In Fig. 3.6, the trend of the drag coefficient with respect to the Reynolds number is shown. It is worth to notice that at very low values of the Reynolds number, the resistance of the sphere is higher than that one of the cylinder, but there is a crossover at very low value ($Re = 10$). In the

range of interest for this study, the resistance is higher for the cylinder. Experimental studies showed that the roughness of the surface of the obstacle strongly affect the value of the coefficient.

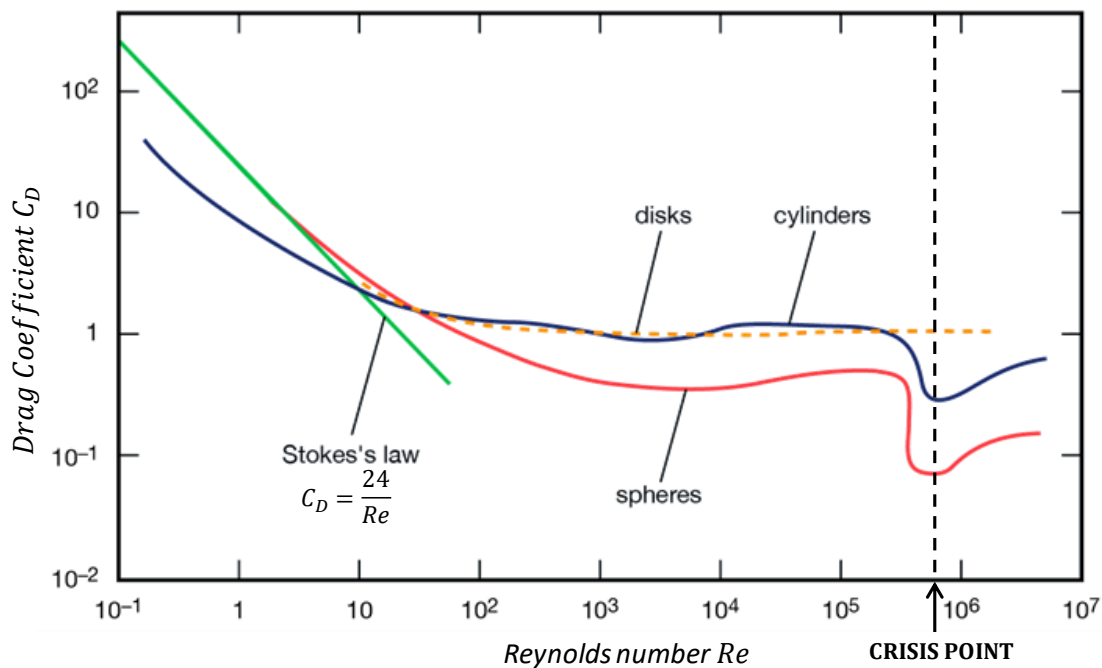


Figure 3.6: Variation of drag coefficient with Reynolds number for spheres, cylinders, and disks [12]

3.3 Analysis of the effects of an axial magnetic field

The effect of magnetic fields on the flow of a conducting fluid around an obstacle concerns a large number of applications in the MHD field. For this reason, that problems are of key concern for MHD, from both a theoretical and experimental point of view, with a special attention to the case of the magnetic field perpendicular to the velocity at infinity. The case of the magnetic field aligned with the velocity flow has been less studied [13].

These studies mostly concern the evolution of the flow configuration and drag coefficient for large value of the interaction parameter N , while the few works which are presented in literature concern small or moderate values of N [14] [15]. Among the effects of magnetic field found in these studies, the main ones are the evolution of Von Karman street, which results in a modification of the drag coefficient.

In this section, the main features of the numerical model of the problem are given. To do this, the experimental setup described in [16] will be used as main reference. In this study, using a liquid

metal as fluid, it was observed a strong modification of the wake, with a disappearance of the vortices for an interaction parameter near to 0.5 and, when the Alfvén number is lower than 1.

Starting from experimental results obtained in [16] and [17], this work analyses the interactions between an electrically conductive fluid, flowing around a cylinder into a regular domain, and an aligned magnetic field. Considering different values of Reynolds number, a procedure has been developed to determine the critical value of interaction parameter N at which the vortices disappear.

Up to now, only the homogeneous situation such as the cylinder has the same magnetic permeability than the fluid have been considered. In the present work, the homogeneous situation is firstly analysed, but successively the impact of the variation of magnetic permeability of the cylinder with respect to that one of the fluid has been investigated. In fact, the ratio between the magnetic permeabilities of the cylinder and the fluid is one of the important governing parameters. Also, the dependency between the dimensionless parameters: Strouhal number, Reynolds number and interaction parameter N , has been studied.

The system has been modeled with Finite Elements Method (FEM) Comsol® software. Using the multi-physics approach, several configurations have been examined, with different values of the Reynolds number, and different ratios between the magnetic permeabilities of the fluid and the cylinder. In all tests, the critical interaction parameter N has been determined, and the connection between the Strouhal number and Reynolds number has been evaluated for the different cases.

3.3.1 *Numerical model description*

In this part of the thesis, the main assumptions for the development of the numerical model are described. The system consists of a regular duct, of length L and width H , inside which flows a conductive and incompressible fluid, with density ρ , dynamic viscosity μ_d , conductivity σ and relative magnetic permeability μ_r , around a cylinder of radius R . A sheet of current representing the coil I produces a magnetic field aligned with the velocity field. The domain has a restricted width but a length sufficient to observe the MHD interactions. In Table 3.1 the geometrical parameters of the model are given.

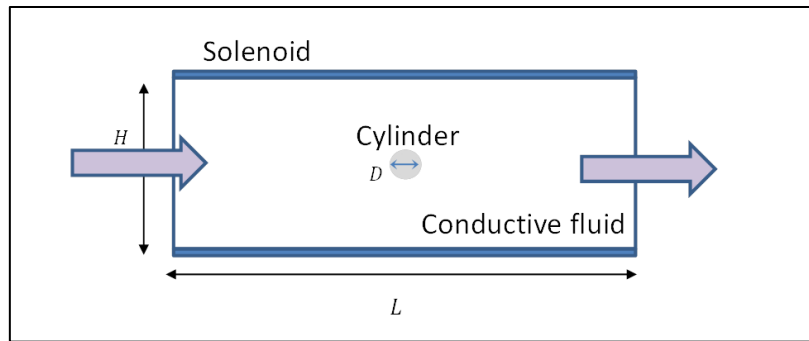


Figure 3.7: Geometry of the model

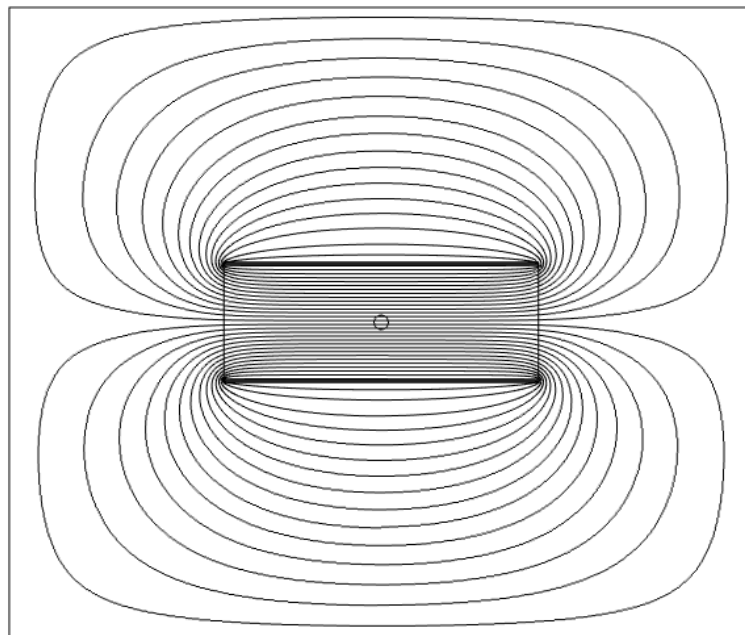


Figure 3.8: Magnetic field distribution

Table 3.1: Geometrical parameters.

Physical quantity	Symbol	Value [units]	Dimensionless value
Radius of cylinder	R	0.05 [m]	$0.05/0.1=0.5$
Length of the pipe	L	2.2 [m]	$2.2/0.1=22$
Width of the pipe	H	0.8 [m]	$0.8/0.1=8$
Solenoid section	a	0.01 [m]	$0.01/0.1=0.1$

As stated above, the magnetic field is obtained by means of a sheet of current with the same axis of the duct. As the model does not correspond exactly to an axisymmetric system, rather than a system with unitary depth, the distribution of the magnetic induction generated by system of currents is a little different with respect to the one generated by a solenoid. For instance, the radial distribution of the induction is not constant in the midpoint of the duct, but the field is stronger near the walls. The aim of the experiments is to have streamlines parallel to the axis of the duct, therefore the length of the duct has to be such that the ends effect is negligible in the region where the results are evaluated.

In Table 3.2 the electromagnetic parameters of the fluid in which the magnetic field is propagated are reported.

Table 3.2: Electromagnetic parameters

Physical quantity	Symbol	[units]
Electrical permittivity	ε	[F/m]
Magnetic permeability	μ	[H/m]
conductivity	σ	[S/m]

To reproduce some operating conditions of the experimental study in [16], the Mercury has been considered as operating fluid, and an electrically isolated cylinder as an obstacle.

As a first step, the fluid behavior without applied magnetic field is considered, with different values of the Reynolds number. In particular, the dependence of the Strouhal number and the C_d coefficient of the Reynolds number are considered. Secondly, a magnetic field is applied to the fluid at rest, to determine its distribution, the diffusion time, the distribution to varying of the magnetic permeability in the fluid and in the cylinder.

The successive step consists in analysing the combination of the fluid dynamics and magnetic field. In particular, the study concerns the MHD configuration of the system for several values of the Reynolds number and interaction parameter. For the last parameter in particular, the critical values N_c , corresponding to the disappearance of the von Karmann street have been identified. As explained before, three situations have been considered:

- a) Magnetic permeability of the fluid equal to that one of the cylinder;
- b) Magnetic permeability of the fluid less than that one of the cylinder;
- c) Magnetic permeability of the fluid greater than that one of the cylinder;

3.3.2 Equations and initial conditions

The study of the time-dependent interaction between the laminar flow and the magnetic field, is based on the equations described in Section 2.1 in particular, the Continuity equation, the Navier Stokes equation and the Magnetic Induction Equation.

Table 3.3: MHD equations.

Name equation	Dimension expression	Dimensionless expression
Navies Stokes equation	$\rho \frac{\partial \mathbf{V}}{\partial t} = -\nabla P + \mu_d \nabla^2 \mathbf{V} + \mathbf{J} \times \mathbf{B}$	$\rho' \frac{\partial (\mathbf{V}')}{\partial (t')} = -\nabla (P') + \frac{1}{Re} \nabla^2 (\mathbf{V}') + N(\mathbf{J}' \times \mathbf{B}')$
Continuity equation	$\nabla \cdot \mathbf{V} = 0$	$\nabla \cdot \mathbf{V}' = 0$
Magnetic Induction equation	$\frac{\partial \mathbf{B}}{\partial t} = \nabla \times (\mathbf{V} \times \mathbf{B}) + \frac{1}{\mu\sigma} \nabla^2 \mathbf{B}$	$\frac{\partial \mathbf{B}'}{\partial t'} = \nabla \times (\mathbf{V}' \times \mathbf{B}') + \frac{1}{R_m} \nabla^2 \mathbf{B}'$

Considering a spatial cylindrical reference system (r, θ, z) the components of the vector terms of the previous equations are reported in Table 3.4.

Table 3.4: Vector parameters of Navier Stokes equation

Vector term	Symbol	Components
Velocity	$\mathbf{u} = \mathbf{u}(r, \theta, z)$	u_r : radial component u_θ : tangential component $u_z = 0$: normal component
Current density	$\mathbf{J} = \mathbf{J}(r, \theta, z)$	$J_r = 0$: radial component $J_\theta = 0$: tangential component J_z : normal component
Magnetic Field	$\mathbf{B} = \mathbf{B}(r, \theta, z)$	B_r : radial component B_θ : tangential component $B_z = 0$: normal component

Where the normal component of fluid velocity and magnetic field applied are assumed equal to zero and the applied current density has only the normal component J_z .

Let $\mathbf{B}_{app} = \mathbf{B}(r, \theta, 0)$ be the external magnetic field, generated by the current \mathbf{J} , and $\mathbf{B}_{tot} = \mathbf{B}_{tot}(r, \theta, 0)$ the total magnetic field, after interaction with the fluid, it is defined by $\mathbf{B}_{tot} = \mathbf{B}_{app} + \mathbf{b}$, where $\mathbf{b} = \mathbf{b}(r, \theta, 0)$ is the magnetic field generated by the induced currents.

With this hypothesis, the previous equations have been written first in cylindrical coordinates and then in dimensionless form.

The dimensional and dimensionless equations in cylindrical coordinates obtained using the dimensionless analysis (see Section 2) and in particular by imposing the following normalized variables:

$$r = r'R; \quad u_r = u'_r u_0; \quad u_\theta = u'_\theta u_0; \quad t = \frac{t'R}{u_0}; \quad P = P_0 P' = \rho u_0^2 P'$$

$$B_r = B_{0r} + b_r; \quad B_\theta = B_{0\theta} + b_\theta; \quad b_r = b'_r B_0; \quad b_\theta = b'_\theta B_0$$

where R is the cylinder radius, are reported in the following Tables.

Table 3.5: Continuity equation

Dimensional form	Dimensionless form
$\frac{\partial(ru_r)}{\partial r} + \frac{\partial u_\theta}{\partial \theta} = 0$	$\frac{\partial(r'u'_r)}{\partial r'} + \frac{\partial u'_\theta}{\partial \theta} = 0$

Table 3.6: Navier Stokes equations

Dimensional form
$\frac{\partial u_r}{\partial t} + u_r \frac{\partial u_r}{\partial r} + \frac{u_\theta}{r} \frac{\partial u_r}{\partial \theta} - \frac{u_\theta^2}{r} = -\frac{1}{\rho} \frac{\partial P}{\partial r} + \gamma \left[\frac{1}{r} \frac{\partial}{\partial r} \left(r \frac{\partial u_r}{\partial r} \right) + \frac{1}{r^2} \frac{\partial^2 u_r}{\partial \theta^2} - \frac{u_r}{r^2} - \frac{2}{r^2} \frac{\partial u_\theta}{\partial \theta} \right] + f_r$
$\frac{\partial u_\theta}{\partial t} + u_r \frac{\partial u_\theta}{\partial r} + \frac{u_\theta}{r} \frac{\partial u_\theta}{\partial \theta} + \frac{u_r u_\theta}{r} = -\frac{1}{\rho r} \frac{\partial P}{\partial \theta} + \gamma \left[\frac{1}{r} \frac{\partial}{\partial r} \left(r \frac{\partial u_\theta}{\partial r} \right) + \frac{1}{r^2} \frac{\partial^2 u_\theta}{\partial \theta^2} + \frac{2}{r^2} \frac{\partial u_r}{\partial \theta} - \frac{u_\theta}{r^2} \right] + f_\theta$
Dimensionless form
$\frac{\partial u'_r}{\partial t'} + u'_r \frac{\partial u'_r}{\partial r'} + \frac{u'_\theta}{r'} \frac{\partial u'_r}{\partial \theta} - \frac{u'^2_\theta}{r'} = -\frac{1}{\rho} \frac{\partial P'}{\partial r'} + \frac{1}{R_e} \left[\frac{1}{r'} \frac{\partial}{\partial r'} \left(r' \frac{\partial u'_r}{\partial r'} \right) + \frac{1}{r'^2} \frac{\partial^2 u'_r}{\partial \theta^2} - \frac{u'_r}{r'^2} - \frac{2}{r'^2} \frac{\partial u'_\theta}{\partial \theta} \right] - \frac{\alpha^2 B'_\theta}{r'} \left[\frac{\partial(r'b'_\theta)}{\partial r'} - \frac{\partial b'_r}{\partial \theta} \right]$
$\frac{\partial u'_\theta}{\partial t'} + u'_r \frac{\partial u'_\theta}{\partial r'} + \frac{u'_\theta}{r'} \frac{\partial u'_\theta}{\partial \theta} + \frac{u'_r u'_\theta}{r'} = -\frac{1}{r'} \frac{\partial P'}{\partial \theta} + \frac{1}{R_e} \left[\frac{1}{r'} \frac{\partial}{\partial r'} \left(r' \frac{\partial u'_\theta}{\partial r'} \right) + \frac{1}{r'^2} \frac{\partial^2 u'_\theta}{\partial \theta^2} + \frac{2}{r'^2} \frac{\partial u'_r}{\partial \theta} - \frac{u'_\theta}{r'^2} \right] + \alpha^2 \frac{B'_r}{r'} \left[\frac{\partial(r'b'_\theta)}{\partial r'} - \frac{\partial b'_r}{\partial \theta} \right]$

In the dimensional form of Navier Stokes equations γ is the kinematic viscosity; f_r and f_θ are obtained by considering the Laplace force $\mathbf{F} = \mathbf{J} \times \mathbf{B}$, that accounts for the MHD interaction, and calculating the following reports:

$$\begin{aligned} \text{rot}\mathbf{B} &= \text{rot}(\mathbf{B}_0 + \mathbf{b}) = \mu \mathbf{J} & \text{with} & \quad \text{rot}(\mathbf{B}_0) = 0 \\ \mathbf{J} &= \frac{1}{\mu} \text{rot}\mathbf{b} & \text{from witch:} & \quad \mathbf{J} \times \mathbf{B} = \frac{1}{\mu} \text{rot}\mathbf{b} \times \mathbf{B} = f_r \mathbf{i} + f_\theta \mathbf{j} + 0 \mathbf{k} \\ f_r &= -\frac{B_\theta}{\mu r} \left[\frac{\partial(r b_\theta)}{\partial r} - \frac{\partial(b_r)}{\partial \theta} \right] & f_\theta &= \frac{B_r}{\mu r} \left[\frac{\partial(r b_\theta)}{\partial r} - \frac{\partial(b_r)}{\partial \theta} \right] & \alpha^2 &= \frac{R_m}{N} \end{aligned}$$

Table 3.7: Magnetic Induction equations

Dimensional expression
$\begin{aligned} &\frac{\partial(B_{0r} + b_r)}{\partial t} + u_r \frac{\partial(B_{0r} + b_r)}{\partial r} + \frac{u_\theta}{r} \frac{\partial(B_{0r} + b_r)}{\partial \theta} \\ &= (B_{0r} + b_r) \frac{\partial u_r}{\partial r} + (B_{0\theta} + b_\theta) \frac{\partial u_r}{r \partial \theta} + \frac{1}{\mu \sigma} \left[\frac{\partial^2(B_{0r} + b_r)}{\partial r^2} + \frac{1}{r} \frac{\partial(B_{0r} + b_r)}{\partial r} + \frac{1}{r^2} \frac{\partial^2(B_{0r} + b_r)}{\partial \theta^2} \right] \end{aligned}$
$\begin{aligned} &\frac{\partial(B_{0\theta} + b_\theta)}{\partial t} + u_r \frac{\partial(B_{0\theta} + b_\theta)}{\partial r} + \frac{u_\theta}{r} \frac{\partial(B_{0\theta} + b_\theta)}{\partial \theta} \\ &= (B_{0r} + b_r) \frac{\partial u_\theta}{\partial r} + (B_{0\theta} + b_\theta) \frac{\partial u_\theta}{r \partial \theta} + \frac{1}{\mu \sigma} \left[\frac{\partial^2(B_{0\theta} + b_\theta)}{\partial r^2} + \frac{1}{r} \frac{\partial(B_{0\theta} + b_\theta)}{\partial r} + \frac{1}{r^2} \frac{\partial^2(B_{0\theta} + b_\theta)}{\partial \theta^2} \right] \end{aligned}$
Dimensionless expression
$\begin{aligned} &\frac{\partial(B'_{0r} + b'_r)}{\partial t'} + u'_r \frac{\partial(B'_{0r} + b'_r)}{\partial r'} + \frac{u'_\theta}{r'} \frac{\partial(B'_{0r} + b'_r)}{\partial \theta} \\ &= (B'_{0r} + b'_r) \frac{\partial u'_r}{\partial r'} + (B'_{0\theta} + b'_\theta) \frac{\partial u'_r}{r' \partial \theta} \\ &+ \frac{1}{R_m} \left[\frac{\partial^2(B'_{0r} + b'_r)}{\partial r'^2} + \frac{1}{r'} \frac{\partial(B'_{0r} + b'_r)}{\partial r'} + \frac{1}{r'^2} \frac{\partial^2(B'_{0r} + b'_r)}{\partial \theta^2} \right] \end{aligned}$
$\begin{aligned} &\frac{\partial(B'_{0\theta} + b'_\theta)}{\partial t'} + u'_r \frac{\partial(B'_{0\theta} + b'_\theta)}{\partial r'} + \frac{u'_\theta}{r'} \frac{\partial(B'_{0\theta} + b'_\theta)}{\partial \theta} \\ &= (B'_{0r} + b'_r) \frac{\partial u'_\theta}{\partial r'} + (B'_{0\theta} + b'_\theta) \frac{\partial u'_\theta}{r' \partial \theta} \\ &+ \frac{1}{R_m} \left[\frac{\partial^2(B'_{0\theta} + b'_\theta)}{\partial r'^2} + \frac{1}{r'} \frac{\partial(B'_{0\theta} + b'_\theta)}{\partial r'} + \frac{1}{r'^2} \frac{\partial^2(B'_{0\theta} + b'_\theta)}{\partial \theta^2} \right] \end{aligned}$

The equations in Table 3.7 can be simplified if $R_m \ll 1$ and if $b \ll B$, $\frac{b}{B} \ll 1$, $b_r \ll B_r$, and $b_\theta \ll B_\theta$, obtaining the equations reported in Table 3.8.

Table 3.8: Simplification of Magnetic Induction equations.

Dimensional form
$\frac{\partial B_{0r}}{\partial t} + u_r \frac{\partial B_{0r}}{\partial r} + \frac{u_\theta}{r} \frac{\partial B_{0r}}{\partial \theta} = B_{0r} \frac{\partial u_r}{\partial r} + B_{0\theta} \frac{\partial u_r}{r \partial \theta} + \frac{1}{\mu\sigma} \left[\nabla^2 b_r - \frac{B_{0r}}{r^2} - \frac{2}{r^2} \frac{\partial B_{0\theta}}{\partial \theta} \right]$
$\frac{\partial B_{0\theta}}{\partial t} + u_r \frac{\partial B_{0\theta}}{\partial r} + \frac{u_\theta}{r} \frac{\partial B_{0\theta}}{\partial \theta} = B_{0r} \frac{\partial u_\theta}{\partial r} + B_{0\theta} \frac{\partial u_\theta}{r \partial \theta} + \frac{1}{\mu\sigma} \left[\nabla^2 b_\theta - \frac{B_{0\theta}}{r^2} + \frac{2}{r^2} \frac{\partial B_{0r}}{\partial \theta} \right]$
Dimensionless form
$\frac{\partial B'_r}{\partial t'} + u'_r \frac{\partial B'_r}{\partial r'} + \frac{u'_\theta}{r'} \frac{\partial B'_r}{\partial \theta} = B'_r \frac{\partial u'_r}{\partial r'} + B'_\theta \frac{\partial u'_r}{r' \partial \theta} + \frac{1}{R_m} \left[R \frac{\partial^2 b'_r}{\partial r'^2} + \frac{1}{r'} \frac{\partial b'_r}{\partial r'} + \frac{1}{r'^2} \frac{\partial^2 b'_r}{\partial \theta^2} - \frac{B'_r}{r'^2} - \frac{2}{r'^2} \frac{\partial B'_\theta}{\partial \theta} \right]$
$\frac{\partial B'_\theta}{\partial t'} + u'_r \frac{\partial B'_\theta}{\partial r'} + \frac{u'_\theta}{r'} \frac{\partial B'_\theta}{\partial \theta} = B'_r \frac{\partial u'_\theta}{\partial r'} + B'_\theta \frac{\partial u'_\theta}{r' \partial \theta} + \frac{1}{R_m} \left[R \frac{\partial^2 b'_\theta}{\partial r'^2} + \frac{\partial b'_\theta}{r' \partial r'} + \frac{1}{r'^2} \frac{\partial^2 b'_\theta}{\partial \theta^2} - \frac{B'_\theta}{r'^2} + \frac{2}{r'^2} \frac{\partial B'_r}{\partial \theta} \right]$

The hypotheses used for solving the problem are described in the following steps:

1. At initial time the fluid enters on the left section of the domain with velocity V_0 .
To reduce the effect of the confinement the walls of the domain are moving at the same velocity as the incoming fluid $V_0 = V_{walls}$ (see Fig. 3.9). Motion of fluid was assumed laminar.
2. The fluid-dynamic flow regime is reached. This condition is almost instantly but the duration of the phase was chosen longer: $t = 15 \text{ s} \gg \frac{L}{V_0}$ (typical transfer time) and $t' = \frac{t}{t_0} = \frac{t}{D} V_0$ (dimensionless time).
3. At the instant $t = 15 \text{ s}$ a current I is applied to the internal walls of the domain (solenoid) which generates a magnetic field B that penetrates by diffusion into the conducting fluid with a diffusion time equal to $\tau_d = \mu\sigma L^2$.
4. The MHD Multiphysics study starts when the magnetic field reaches the steady-state condition (for $R_m \ll 1$, for high values of magnetic Reynolds number the steady state condition is never reached). This last phase persists 15 s ($t' = \frac{t}{D} V_0$).

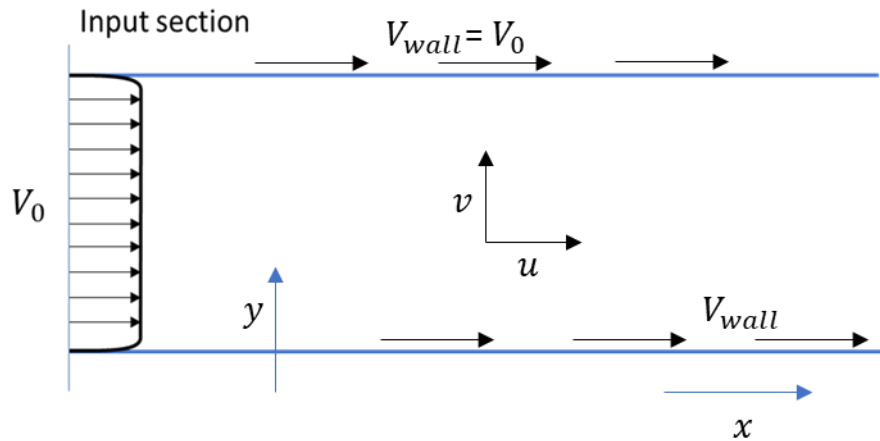


Figure 3.9: Profile of velocity in the input section

3.3.3. Characterisation of the magnetic field distribution for small R_m and for any value of the permeabilities ratio: μ_{flu}/μ_{cyl}

The following conditions are expressed only to small values of the magnetic Reynolds number. If R_m is very small, the ratio between induced magnetic field and the applied one (due to the electric current in the conducting walls) is such as:

$$\frac{b}{B} = R_m \ll 1$$

Therefore, it is possible to neglect the induced field. In this condition and referring to the induction equation (2.10) the distribution of the magnetic field is controlled by the Laplace equation $\nabla^2 B = 0$.

Another important consequence related to small values of the magnetic Reynolds number is that it decouples the hydrodynamics of the flow from the magnetic field distribution. As a consequence, the first part of the boundary conditions concerns the magnetic field distribution on the frontiers of the domain that includes the surface of the cylinder itself. This problem is not trivial and needs to take into account the discontinuity generated by the gap of magnetic permeability outside and inside the cylinder.

To take into account this discontinuity there are two methods. The first one is to solve the Laplace equation in the both domains inside and outside of the cylinder and to identify the magnetic induction at the interface assuming the magnetic permeability's discontinuity between the two domains.

Another solution, which has been used in this thesis, is to remark that the gap of magnetic permeability at the interface is characterised by a discontinuity of the tangential component of the magnetic induction such as:

$$\frac{B_{\theta(cyl)}}{B_{\theta(fluid)}} = \frac{\mu_{fluid}}{\mu_{cyl}}$$

while the normal component is characterised by a discontinuity of the magnetic field such as:

$$\frac{H_{n(cyl)}}{H_{n(fluid)}} = \frac{\mu_{fluid}}{\mu_{cyl}}$$

The discontinuity of the tangential component of the magnetic induction can be characterised by a magnetic induction vortex line at the interface and the discontinuity of the magnetic field can be characterised by a magnetic field source line, which correspond respectively to surface distribution of current in the direction orthogonal to the plane of the domain, and a surface distribution of magnetic dipoles with radial orientation.

The intensity Γ of the current density is such as:

$$\Gamma = \frac{B_{\theta(fluid)}}{\mu_{fluid}} \left(1 - \frac{\mu_{fluid}}{\mu_{cyl}} \right) \quad (3.7)$$

where $B_{\theta(fluid)}$ is the component of the magnetic field in the tangential direction with respect to the surface of the cylinder. This implies that the value of Γ varies along the surface of the cylinder.

Similarly, the intensity of the dipole q is

$$q = H_{r(fluid)} \left(1 - \frac{\mu_{fluid}}{\mu_{cyl}} \right) \quad (3.8)$$

These two distributions allow one to determine the distribution of the magnetic field as the medium has homogeneous permeability, and the contribution due to the different permeability between fluid and cylinder is calculated as the superposition of the two distributed sources Γ and q .

In each point of the domain, the magnetic field is given by the sum of the contributions of the currents in the walls (that are the source of magnetic field in the domain) and the contribution of the discontinuity of magnetic permeability at the interface that are represented by a current and a magnetic dipole depending on local values..

3.3.3.1 Contribution to the magnetic field due to the walls

In this section, the calculation of component B_x and B_y in a generic point M , generated by a current in two walls sections, is reported.

Referring to Fig. 3.10 and considering an element of current $dI = J(\xi, \eta) \cdot d\xi d\eta$ located at point $P(\xi, \eta)$ on the upper wall of the domain, the contribution of magnetic field in a generic point $M(x, y)$ can be obtained by applying the Ampère's law:

$$2\pi r \cdot dB = \mu \cdot dI = \mu \cdot J(\xi, \eta) \cdot d\xi d\eta$$

and then:

$$dB = \frac{\mu J(\xi, \eta) d\xi d\eta}{2\pi \sqrt{(x-\xi)^2 + (\eta-y)^2}} \quad (3.9)$$

where μ is the magnetic permeability of the fluid.

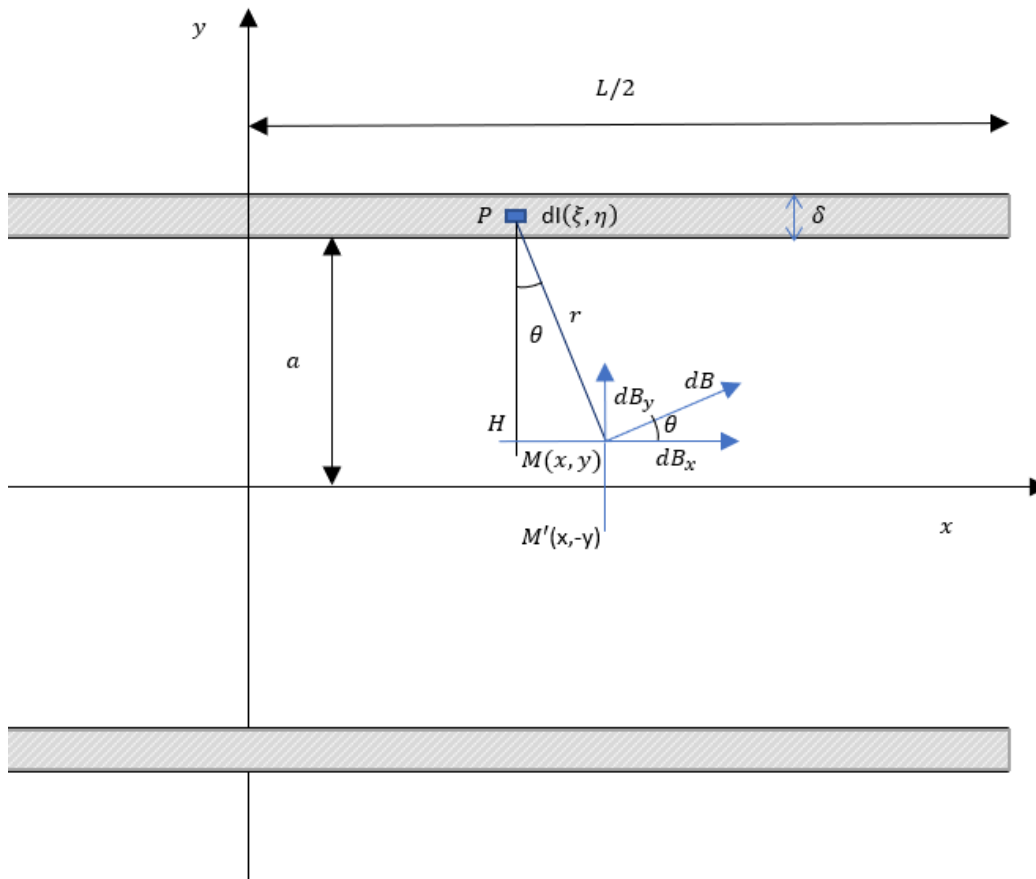


Figure 3.10: Magnetic field generated by the small element on the upper wall

Let $dB_x = dB\cos\theta$ and $dB_y = dB\sin\theta$ be the components along the x -axis and y -axis respectively, by integrating all along the solenoid, the contribution of the wall to the magnetic field in a generic point M , can be calculated.

Here, only the final results are reported. See Appendix 1 for the details.

$$B_x = \frac{\mu J}{4\pi} \left\{ \left(x - \frac{L}{2} \right) \ln \left(1 + \frac{\delta^2 - 2y\delta + 2a\delta}{\left(x - \frac{L}{2} \right)^2 + (a-y)^2} \right) - \left(x + \frac{L}{2} \right) \ln \left(1 + \frac{\delta^2 - 2y\delta + 2a\delta}{\left(x + \frac{L}{2} \right)^2 + (a-y)^2} \right) + \right. \\ \left. + 2(a + \delta - y) \left[\operatorname{atan} \left(\frac{x - \frac{L}{2}}{a + \delta - y} \right) - \operatorname{atan} \left(\frac{x + \frac{L}{2}}{a + \delta - y} \right) \right] - 2(a - y) \left[\operatorname{atan} \left(\frac{x - \frac{L}{2}}{a - y} \right) - \operatorname{atan} \left(\frac{x + \frac{L}{2}}{a - y} \right) \right] \right\} \quad (3.10)$$

$$B_y = \frac{\mu J}{4\pi} \left\{ (a + \delta - y) \ln \left[\frac{\left(x - \frac{L}{2} \right)^2 + (a + \delta - y)^2}{\left(x + \frac{L}{2} \right)^2 + (a + \delta - y)^2} \right] - (a - y) \ln \left[\frac{\left(x - \frac{L}{2} \right)^2 + (a - y)^2}{\left(x + \frac{L}{2} \right)^2 + (a - y)^2} \right] + \right. \\ \left. + 2 \left(x - \frac{L}{2} \right) \left[\operatorname{atan} \left(\frac{a + \delta - y}{x - \frac{L}{2}} \right) - \operatorname{atan} \left(\frac{a - y}{x - \frac{L}{2}} \right) \right] - 2 \left(x + \frac{L}{2} \right) \left[\operatorname{atan} \left(\frac{a + \delta - y}{x + \frac{L}{2}} \right) - \operatorname{atan} \left(\frac{a - y}{x + \frac{L}{2}} \right) \right] \right\} \quad (3.11)$$

\mathbf{J} is the current density in the walls, which is constant in the cross section, and it has opposite values in the two walls. To calculate the contribution, in the same point M , due to the lower wall, the symmetry condition of the domain was exploited.

Let consider the Fig. 3.11. In the point $M(x, y)$ the component of magnetic field generated by the upper wall is $B_x^{up}(M)$ is superimposed with the component generated by the lower wall is $B_x^{low}(M)$.

For symmetry, the value of magnetic field generated by the lower wall in the point $M(x, y)$, will be equal to the value of magnetic field generated by the upper wall in the point $M'(x, -y)$:

$$B_x^{low}(M) = B_x^{up}(M')$$

A similar reasoning leads to deduce the following relation for the y component:

$$B_y^{low}(M) = -B_y^{up}(M')$$

where the y component of magnetic field in the point $M(x, -y)$ generated by the upper wall is negative for reverse direction of magnetic field lines.

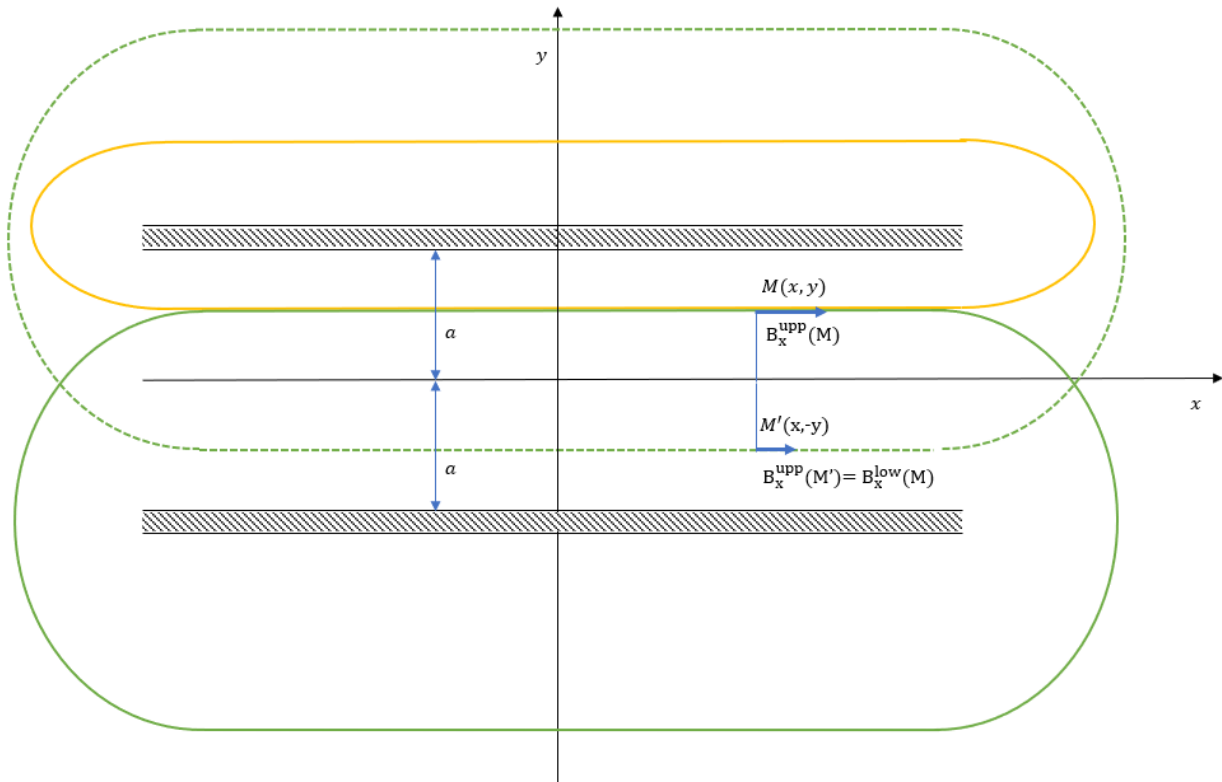


Figure 3.11: Contribution to the Magnetic field due to the two walls.

Therefore, the total magnetic field components, due to the contribution of the two planes will be:

$$\begin{cases} B_x(x, y) = B_x^{up}(x, y) + B_x^{up}(x, -y) \\ B_y(x, y) = B_y^{up}(x, y) - B_y^{up}(x, -y) \end{cases} \quad (3.12)$$

3.3.3.2 Contribution of magnetic field due to the discontinuity of magnetic permeability.

Due to the different permeability between fluid and cylinder, a discontinuity is observed, at the interface, of both the tangential component of the induction B and the normal component of the magnetic field H . The effects of the discontinuity of permeability are reproduced by suitable equivalent surface currents and magnetic dipoles distributed all along the surface of the cylinder.

Let assume that an element of current $dI = \Gamma R d\alpha$ circulates in a small arc of the cylinder surface $ds = R d\alpha$ (see Fig. 3.12). The current density Γ has to reproduce the same discontinuity of the tangential component of the induction due to the discontinuity of the permeability.

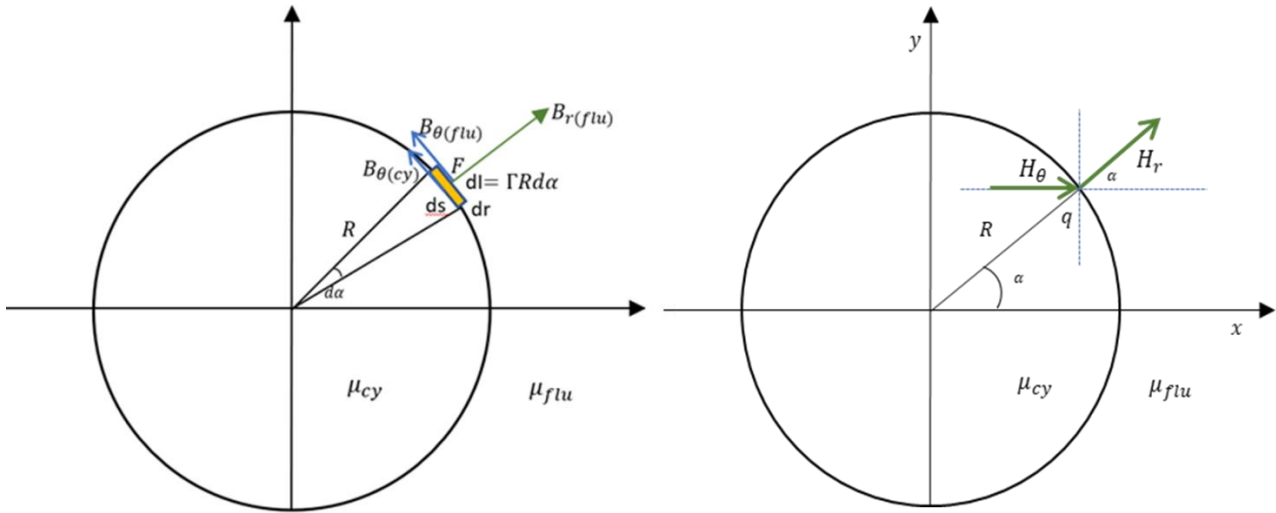


Figure 3.12: Discontinuity of tangential component of the magnetic induction and of radial component of magnetic field

$$B_{\theta(flu)} = \frac{\Gamma}{2}$$

In the same way the contribution of the dipole produces a radial magnetic field such as:

$$q = H_{r(flu)} \left(1 - \frac{\mu_{flu}}{\mu_{cy}} \right) \text{ and } H_r(flu) = \frac{q}{2}$$

The expression of density current $\Gamma(\alpha)$ and dipole $q(\alpha)$ of magnetic field are reported hereunder. The calculations of these formulas are reported in Appendix 2.

$$\Gamma(\alpha) =$$

$$\frac{J}{4\pi} \left(1 - \frac{\mu_{flu}}{\mu_{cy}} \right) \left\{ 2 \operatorname{atan} \left[\frac{\frac{L}{2} \pm R \cos \alpha}{a \pm R \sin \alpha} \right] \sin \alpha - \left[\ln \frac{\left(\frac{L}{2} - R \cos \alpha \right)^2 + (a - R \sin \alpha)^2}{\left(\frac{L}{2} + R \cos \alpha \right)^2 + (a - R \sin \alpha)^2} + \ln \frac{\left(\frac{L}{2} + R \cos \alpha \right)^2 + (a + R \sin \alpha)^2}{\left(\frac{L}{2} - R \cos \alpha \right)^2 + (a + R \sin \alpha)^2} \right] \cos \alpha \right\} \quad (3.13)$$

$$q(\alpha) =$$

$$\frac{J}{4\pi} \left(1 - \frac{\mu_{flu}}{\mu_{cy}} \right) \left\{ 2 \operatorname{atan} \left[\frac{\frac{L}{2} \pm R \cos \alpha}{a \pm R \sin \alpha} \right] \cos \alpha + \left[\ln \frac{\left(\frac{L}{2} - R \cos \alpha \right)^2 + (a - R \sin \alpha)^2}{\left(\frac{L}{2} + R \cos \alpha \right)^2 + (a - R \sin \alpha)^2} + \ln \frac{\left(\frac{L}{2} + R \cos \alpha \right)^2 + (a + R \sin \alpha)^2}{\left(\frac{L}{2} - R \cos \alpha \right)^2 + (a + R \sin \alpha)^2} \right] \sin \alpha \right\} \quad (3.14)$$

Referring to the Fig. 3.13, the contribution to the magnetic field, in a generic point M of the distribution of current $\Gamma(\alpha)$ can be calculated.

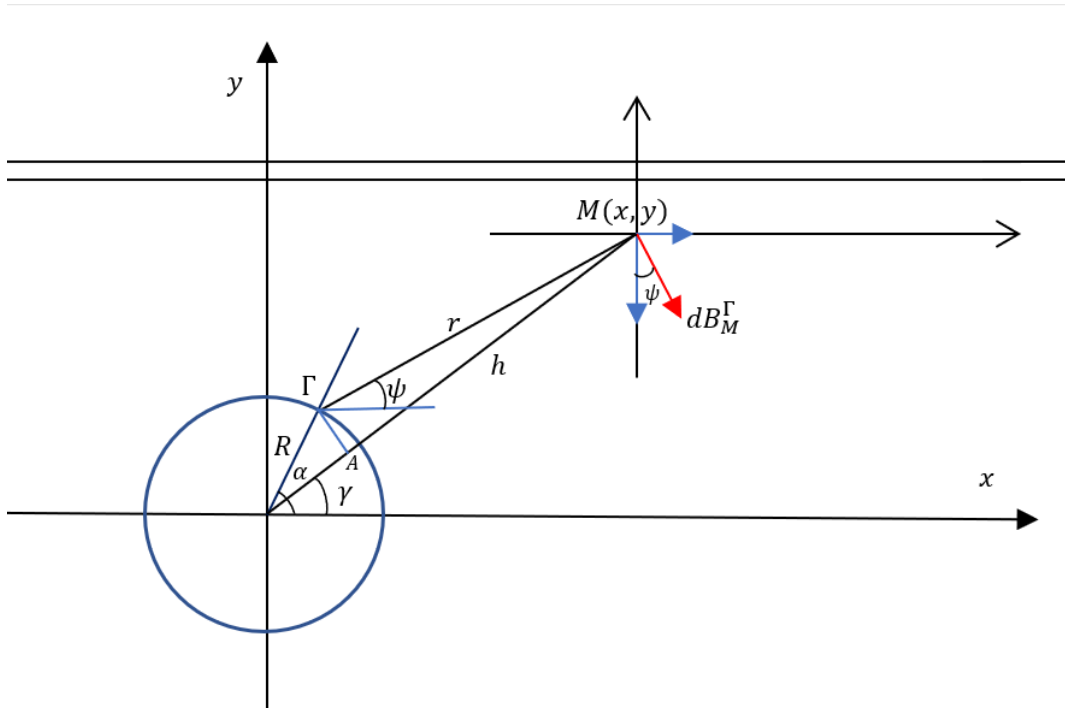


Figure 3.13: Magnetic field in a generic point M of the domain due of the distribution $\Gamma(\alpha)$.

Let be $dl = \Gamma(\alpha)Rd\alpha$ an element of current on the surface of the cylinder at distance r from the point $M(x, y)$ that produces, in the point M , an induction field such that:

$$dB_M^\Gamma = \frac{\mu_{ftu} \Gamma(\alpha) R d\alpha}{2\pi r} \quad (3.15)$$

The horizontal and vertical components can be calculated by projecting dB_M^Γ along the horizontal and vertical directions:

$$dB_{M,x}^\Gamma = dB_M^\Gamma \sin\psi = \frac{\mu_{ftu} \Gamma(\alpha) R d\alpha}{2\pi r} \sin\psi \quad (3.16)$$

$$dB_{M,y}^\Gamma = -dB_M^\Gamma \cos\psi = -\frac{\mu_{ftu} \Gamma(\alpha) R d\alpha}{2\pi r} \cos\psi \quad (3.17)$$

Being:

$$r^2 = [h - R\cos(\alpha - \gamma)]^2 + R^2 \sin^2(\alpha - \gamma) = h^2 - 2hR\cos(\alpha - \gamma) + R^2$$

$$\begin{cases} x = R\cos\alpha + r\cos\psi \\ y = R\sin\alpha + r\sin\psi \end{cases} \quad \begin{cases} x = h\cos\gamma \\ y = h\sin\gamma \end{cases}$$

where:

$$\sin\psi = \frac{y - R\sin\alpha}{\sqrt{h^2 - 2hR\cos(\alpha - \gamma) + R^2}} \quad \cos\psi = \frac{x - R\cos\alpha}{\sqrt{h^2 - 2hR\cos(\alpha - \gamma) + R^2}}$$

we can write:

$$dB_{M,x}^{\Gamma} = \frac{\mu_{flu} R \Gamma(\alpha) (h \sin \gamma - R \sin \alpha)}{2\pi [h^2 - 2hR \cos(\alpha - \gamma) + R^2]} d\alpha \quad (3.18)$$

$$dB_{M,y}^{\Gamma} = -\frac{\mu_{flu} R \Gamma(\alpha) (h \cos \gamma - R \cos \alpha)}{2\pi [h^2 - 2hR \cos(\alpha - \gamma) + R^2]} d\alpha \quad (3.19)$$

The total values of $B_{M,x}^{\Gamma}$ and $B_{M,y}^{\Gamma}$ are obtained by integrating along the angle α . For symmetry reasons, the integral can be evaluated in the interval $[-\pi, \pi]$:

$$B_{M,x}^{\Gamma} = \frac{\mu_{flu} R}{2\pi} \int_{-\pi}^{\pi} \frac{\Gamma(\alpha) (h \sin \gamma - R \cos \alpha)}{[h^2 - 2hR \cos(\alpha - \gamma) + R^2]} d\alpha \quad (3.20)$$

$$B_{M,y}^{\Gamma} = -\frac{\mu_{flu} R}{2\pi} \int_{-\pi}^{\pi} \frac{\Gamma(\alpha) (h \cos \gamma - R \cos \alpha)}{[h^2 - 2hR \cos(\alpha - \gamma) + R^2]} d\alpha \quad (3.21)$$

Referring to the Fig. 3.14, the contribution of the distribution of magnetic dipoles $q(\alpha)$ to the magnetic field, in a generic point M of the domain can be calculated as follows.

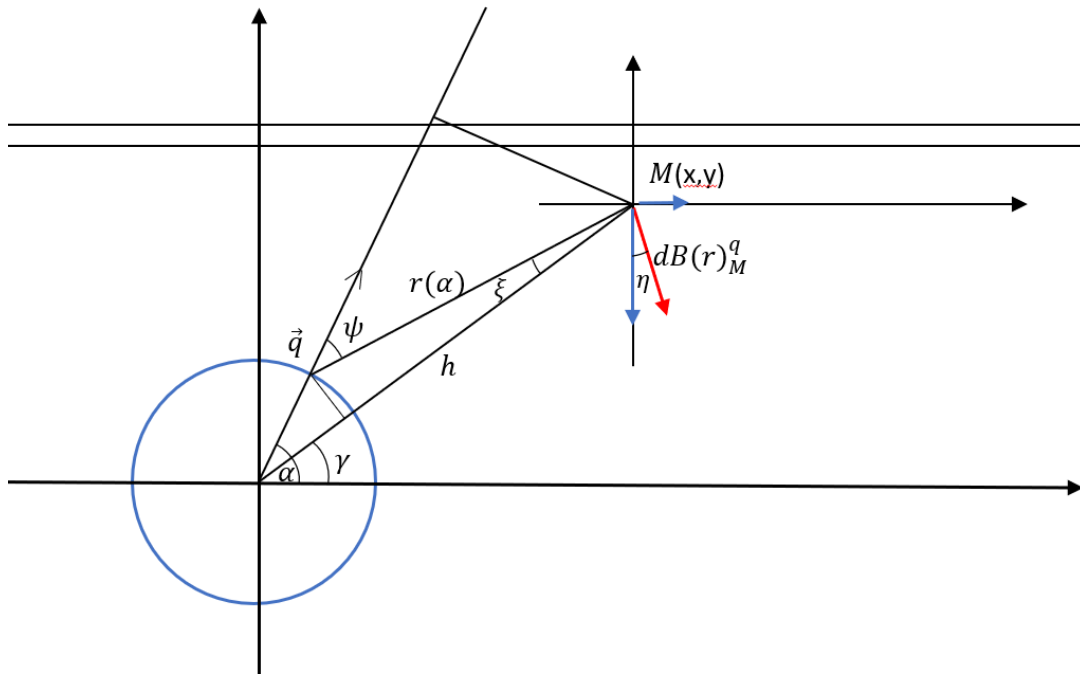


Figure 3.14: Magnetic field in a generic point M of the domain due of the distribution $q(\alpha)$

The magnetic field, due to the dipole distribution $q(\alpha)$, in the generic point M of the domain is:

$$dB^q(\vec{r}) = \frac{\mu_{flu}}{4\pi} \left[\frac{3\vec{r} + (\vec{q} \cdot \vec{r})}{r^5} - \frac{\vec{q}}{r^3} \right] \quad (3.25)$$

$$r^2 = h^2 - 2hR \cos(\alpha - \gamma) + R^2$$

$$(\vec{q} \cdot \vec{r}) = q(\alpha) r(\alpha) \cos[\psi(\alpha)]$$

$$h \sin(\alpha - \gamma) = r \sin \psi \quad h^2 \sin^2(\alpha - \gamma) = r^2 (1 - \cos^2 \psi)$$

$$\sin \psi = \frac{h}{r} \sin(\alpha - \gamma) \quad \cos \psi = \sqrt{1 - \frac{h^2}{r^2} \sin^2(\alpha - \gamma)}$$

The horizontal and vertical components can be calculated projecting dB_M^q along the horizontal and vertical direction:

$$dB_{M,x}^q(\mathbf{r}_x) = dB^q(\vec{\mathbf{r}}) \sin \eta = \frac{\mu_{flu}}{4\pi} \left[\frac{3r \cos(\alpha - \psi) + qr \cos \psi}{r^5} - \frac{q \cos \alpha}{r^3} \right] \sin \eta \quad (3.26)$$

$$dB_{M,y}^q(\mathbf{r}_y) = dB^q(\vec{\mathbf{r}}) \cos \eta = \frac{\mu_{flu}}{4\pi} \left[\frac{3r \sin(\alpha - \psi) + qr \cos \psi}{r^5} - \frac{q \sin \alpha}{r^3} \right] \cos \eta \quad (3.27)$$

The total values of $B_{M,x}^q$ and $B_{M,y}^q$ are obtained by integrating along the angle α . For symmetry reasons, the integral can be evaluated in the interval $[-\pi, \pi]$:

$$B_{M,x}^q(\mathbf{r}_x) = \frac{\mu_{flu}}{4\pi} \int_{-\pi}^{\pi} \left[\frac{3r \cos(\alpha - \psi) + qr \cos \psi}{r^5} - \frac{q \cos \alpha}{r^3} \right] \sin \eta \, d\alpha \quad (3.28)$$

$$B_{M,y}^q(\mathbf{r}_y) = \frac{\mu_{flu}}{4\pi} \int_{-\pi}^{\pi} \left[\frac{3r \sin(\alpha - \psi) + qr \cos \psi}{r^5} - \frac{q \sin \alpha}{r^3} \right] \cos \eta \, d\alpha \quad (3.29)$$

Finally, the components of magnetic distribution ($B_\theta; B_r$), in the horizontal and vertical directions due to the interface discontinuity are given by:

$$B_{M,x}^{\Gamma+q} = \frac{\mu_{flu} R}{2\pi} \int_{-\pi}^{\pi} \frac{\Gamma(\alpha) (h \sin \gamma - R \cos \alpha)}{[h^2 - 2hR \cos(\alpha - \gamma) + R^2]} d\alpha + \frac{\mu_{flu}}{4\pi} \int_{-\pi}^{\pi} \left[\frac{3r \cos(\alpha - \psi) + qr \cos \psi}{r^5} - \frac{q \cos \alpha}{r^3} \right] \sin \eta \, d\alpha \quad (3.33)$$

$$B_{M,y}^{\Gamma+q} = -\frac{\mu_{flu} R}{2\pi} \int_{-\pi}^{\pi} \frac{\Gamma(\alpha) (h \cos \gamma - R \sin \alpha)}{[h^2 - 2hR \cos(\alpha - \gamma) + R^2]} d\alpha + \frac{\mu_{flu}}{4\pi} \int_{-\pi}^{\pi} \left[\frac{3r \sin(\alpha - \psi) + qr \cos \psi}{r^5} - \frac{q \sin \alpha}{r^3} \right] \cos \eta \, d\alpha \quad (3.43)$$

The analytical solving of these integrals is beyond the scope of this study. Furthermore, the calculation of the contribution due to the dipole q entails the solving of elliptical integrals that have to be solved numerically.

Finally, by adding the contribution of the walls (upper and lower) and the contributions of the vortex and source at the interface it is possible to express the magnetic field distribution over the whole domain.

$$B_{M,x_{tot}} = B_{M,x}^{up} + B_{M,x}^{low} + B_{M,x}^{\Gamma+q}$$

$$B_{M,y_{tot}} = B_{M,y}^{up} + B_{M,y}^{low} + B_{M,y}^{\Gamma+q}$$

Table 5.1 in Appendix 3 summarizes all the boundary conditions for the magnetic induction field.

3.3.4 *Characterisation of the magnetic field distribution for a generic value of magnetic Reynolds number.*

The above paragraph has assumed that $R_m \ll 1$, and then the induced field was very small compared with the applied one:

$$\frac{b}{B} = R_m \ll 1$$

In the case of high value of R_m , the boundary conditions become more complex in particular for the magnetic field. The reason is that the magnetic field in this situation depends on the induced current resulting of the interaction between velocity field and magnetic induction field. In these conditions, the non-steady state of the Von Karmann Street generated by the cylinder makes non stationary the magnetic field.

As a consequence, the boundary conditions are difficult to express due to the implicit relationship between velocity and induced magnetic field and the dynamic evolution of the phenomenon.

Therefore, the iterative method is necessary. It consists in the following steps:

1. Expressing the boundary conditions of magnetic field by using the formulation described in the previous paragraph (small R_m).
2. Superimposing the velocity field to the magnetic field distribution obtained in the step 1.
3. Deducing from the interaction of the velocity with the magnetic field the current density distribution.
4. Integrating all magnetic field sources: the upper and lower wall electric current distribution and the magnetic source due to the magnetic permeability gap between external to internal values at the frontier of the cylinder and finally the magnetic source due to the current density induced in the fluid.
5. Comparing the obtained magnetic and velocity fields with those ones of the previous iteration. In case the solution appears do not be stabilized, the procedure is iterated from the step 1.
6. This procedure must be performed at each instant to obtain the time dependent evolution of the process.

In this work this problem has been solved using the FEM Comsol® software.

3.3.5 Fluid-dynamic boundary conditions

To write the velocity boundary condition we introduced the stream function of velocity ψ :

$$\mathbf{V} = \nabla \times \psi \Rightarrow V_y = \frac{\partial \psi}{\partial x} \quad \text{and} \quad V_x = -\frac{\partial \psi}{\partial y}$$

The boundary values of the stream function are show in Table 3.9.

Table 3.9: Boundary condition of Vector Potentials of Velocity.

Velocity boundary condition				
Symbol	Vector potentials	Components	Parameters	
$\mathbf{V} = V_x \vec{i} + V_y \vec{j}$ $\mathbf{V} = -\frac{\partial \psi}{\partial y} \vec{i} + \frac{\partial \psi}{\partial x} \vec{j}$	Upper wall $\psi = v_0 a$	$\frac{\partial \psi}{\partial x} = 0$ $\frac{\partial \psi}{\partial y} = V_0$	x	$y = a$
	Lower wall $\psi = -v_0 a$	$\frac{\partial \psi}{\partial x} = 0$ $\frac{\partial \psi}{\partial y} = V_0$	x	$y = -a$
	Cylinder	$\frac{\partial \psi}{\partial x} = 0$ $\frac{\partial \psi}{\partial y} = 0$	x	y
	Inlet: $\psi = v_0 y$	$\frac{\partial \psi}{\partial x} = 0$ $\frac{\partial \psi}{\partial y} = V_0$	$x = -\frac{L}{2}$	y
	Outlet	$p = 0$	$x = \frac{L}{2}$	y

In Fig. 3.15 a representation of vector potential within the boundaries of the domain is shown.

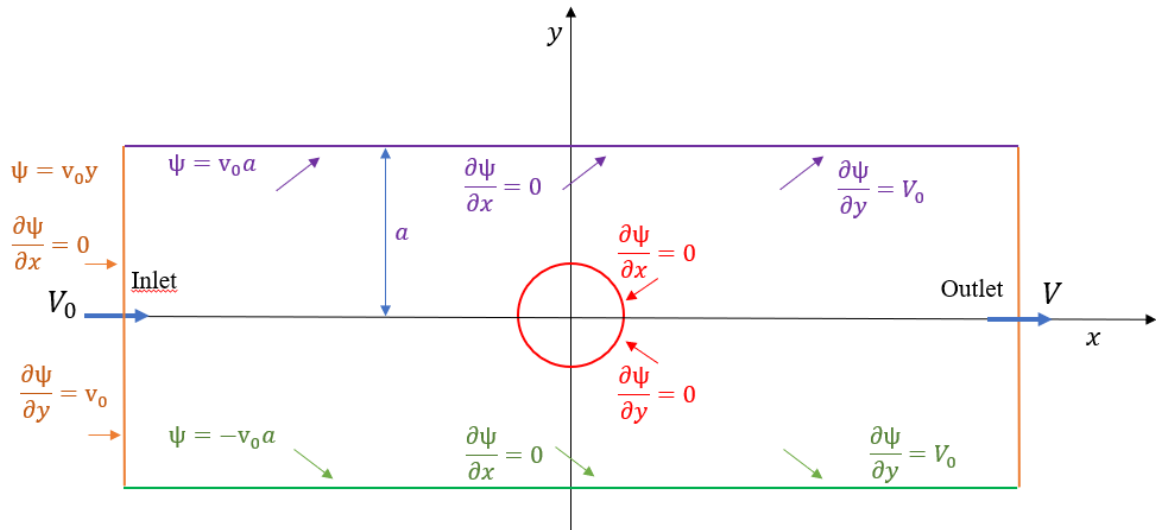


Figure 3.15: Hydrodynamic boundary conditions.

Navier Stokes and continuity equations is a system of three equations with three variables (x component of the velocity, V_x , y component of the velocity V_y , and the pressure P) that constitute a closed system able to characterise the three variables of the systems. In the hypothesis of small magnetic Reynolds number the magnetic field distribution is totally independent from the hydrodynamics distribution, but the converse is not true as hydrodynamics is strongly influenced by the magnetic field.

This work about the magnetic boundary conditions for small magnetic Reynolds number has the only objective to verify if the physics of the system is well posed. In reality these boundary conditions are included in the Comsol software and does not necessitates the analytic expression of the boundary conditions. Only the conditions expressed below are required.

3.4 FEM model

The studied MHD system combines many different phenomena: fluid mechanics, electromagnetism, mass transport.

A simplified 2D FEM analysis of the interaction between the magnetic field and the flowing liquid has been performed assuming the classical MHD model. Heat transfer and transport phenomena have been neglected. The studied 2D domain (Fig. 3.16) has been set as a general rectangle (with length $L = 5.2\text{ m}$ and width $H = 4.2\text{ m}$), inside which, a duct with length $L = 2.2\text{ m}$ and width $H = 0.8\text{ m}$, is included. An electrically insulated cylinder, with radius $R = 0.01\text{ m}$ is positioned at the center of the duct. A coil, made by a 0.01 mm copper wire and crossed by a

current I , generates the magnetic field. A conductive liquid hits the cylinder, the flow coming from the left side of the pipe. A triangular, extremely fine, physics-controlled mesh has been chosen (Fig. 3.17)

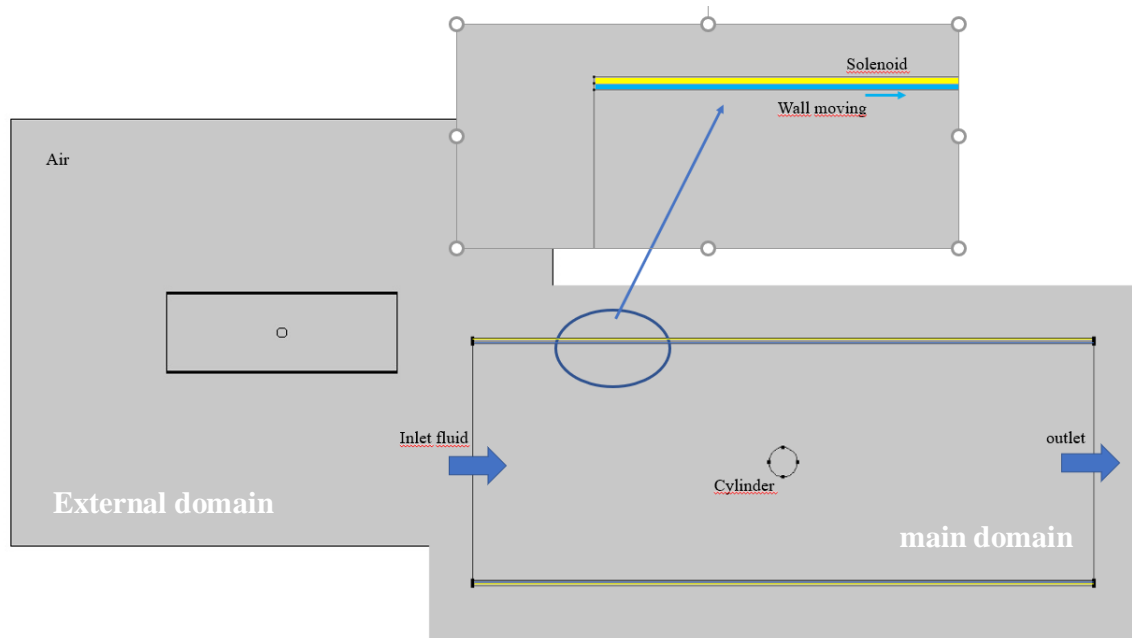


Figure 3.16: FEM Study: geometry.

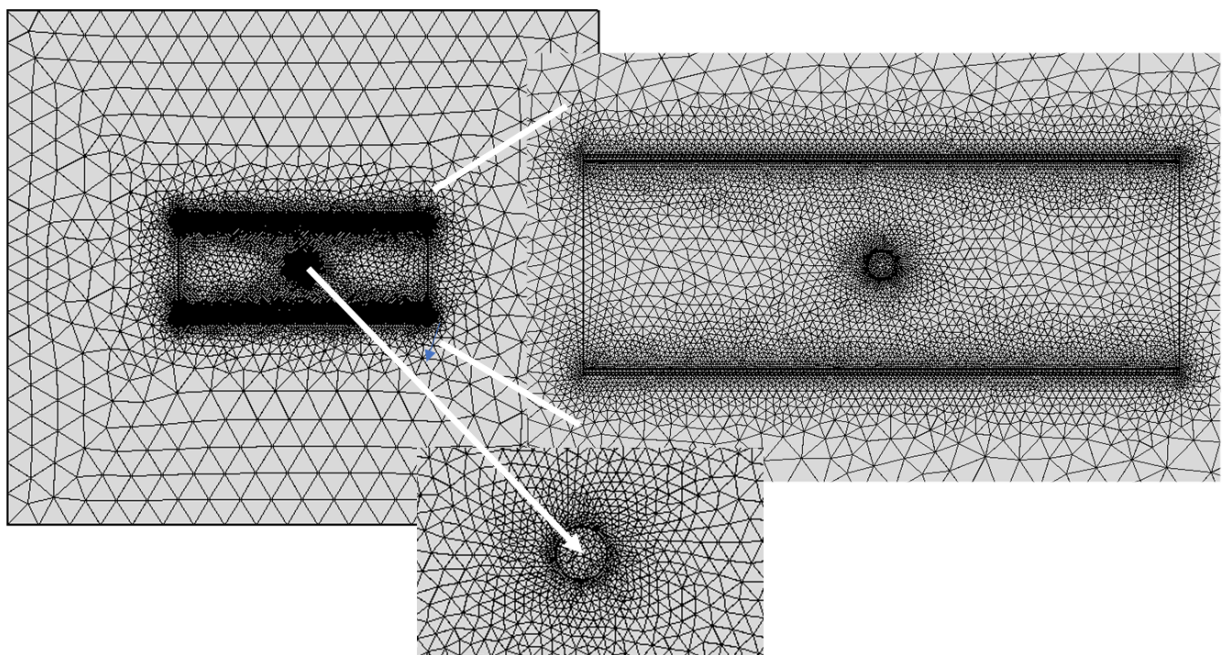


Figure 3.17: FEM Study: mesh.

Air is assumed in the external domain. Several MHD simulations have been performed by means of the commercial software COMSOL Multiphysics[®] [18]. By using the *Laminar Flow regime* the velocity and the pressure fields for a single-phase fluid has been computed.

In this thesis, the Laminar Flow regime has been also assumed for values of Reynolds number in the transition range, due to the fact witnessed in the literature and confirmed in the present study, that the presence of the magnetic field is able to reduce the turbulence.

3.4.1 FEM analysis of the Fluid-Dynamics aspects

The MHD configuration for several values of Reynolds number has been studied to characterize the hydrodynamics of the flow upstream and downstream of the cylinder, the distribution of pressure, the Von Karman wake, the Strouhal number S_t and the drag coefficient C_d .

A first fluid-dynamics analysis has been performed for $Re = 200$ and 1000 .

In Table 3.10 the main parameters of the setup and the inlet condition (at $t = 0$) are reported.

In the Fig. 3.18 the velocity distribution in the domain is shown; this test, lasting $t = 500$ s, refers to the case $Re = 200$. The theoretical zones indicated in this figure can be clearly recognizable. The walls slide with the same velocity of the undisturbed field, which avoids the creation of a boundary layer before the obstacle. This assumption has been assumed to compare the results of the simulation with the experimental results in [16], whose setup consists into a cylinder falling into a vertical duct filled with a liquid at rest. It can be noticed that the wake is formed by two sequences of vortices leaving the surface of the obstacle.

Table 3.10: Constant parameters of system.

Name	Value	Dimensionless value	Description
R	0.05 [m]	0.5	cylinder radius
L	2.2 [m]	22	solenoid length
H	0.8 [m]	8	domain height
A		$D/H = 0.125$	cylinder diameter/domain scale ratio
V_0	0.2, 1 [m/s]	0.2, 1	velocity inlet
P_o	0 [Pa]		pressure outlet
ρ_{flu}	13700 [kg/m ³]	$\rho'_{flu} = \frac{\rho_{flu}}{\rho_0}$	fluid density
ρ_{cyl}	8000 [kg/m ³]	$\rho'_{cyl} = \frac{\rho_{cyl}}{\rho_0}$	cylinder density
μ_d	1.37 [Pa · s]	$\mu'_d = \frac{\mu_d}{D\rho_0 V_0}$	dynamic viscosity of fluid

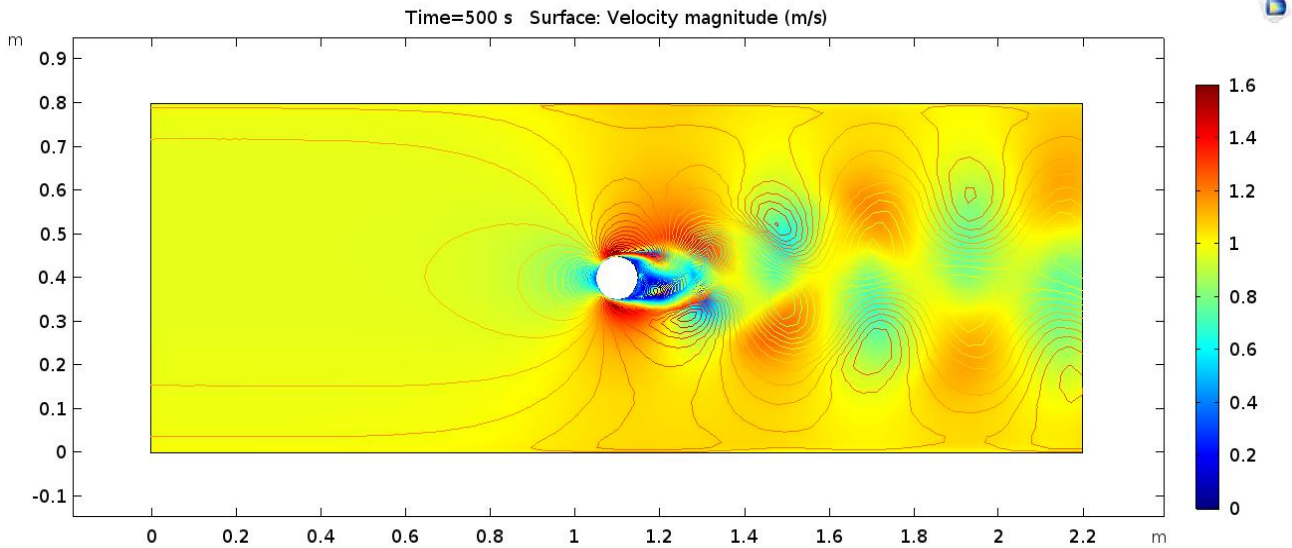


Figure 3.18: Velocity field and formation of Von Karman’s wake behind the cylinder ($Re=200$)

The Fig. 3.19 shows the fluid pressure profile along the surface of cylinder refers to the case $Re = 1000$. The zero of the abscissa corresponds to the stagnation point on axis of the duct, and it corresponds to the maximum value of the pressure. The diagram also shows the transitions from positive to negative pressure. These transitions correspond to the points where the boundary layer takes off; therefore they correspond to the origin of the downstream wake.

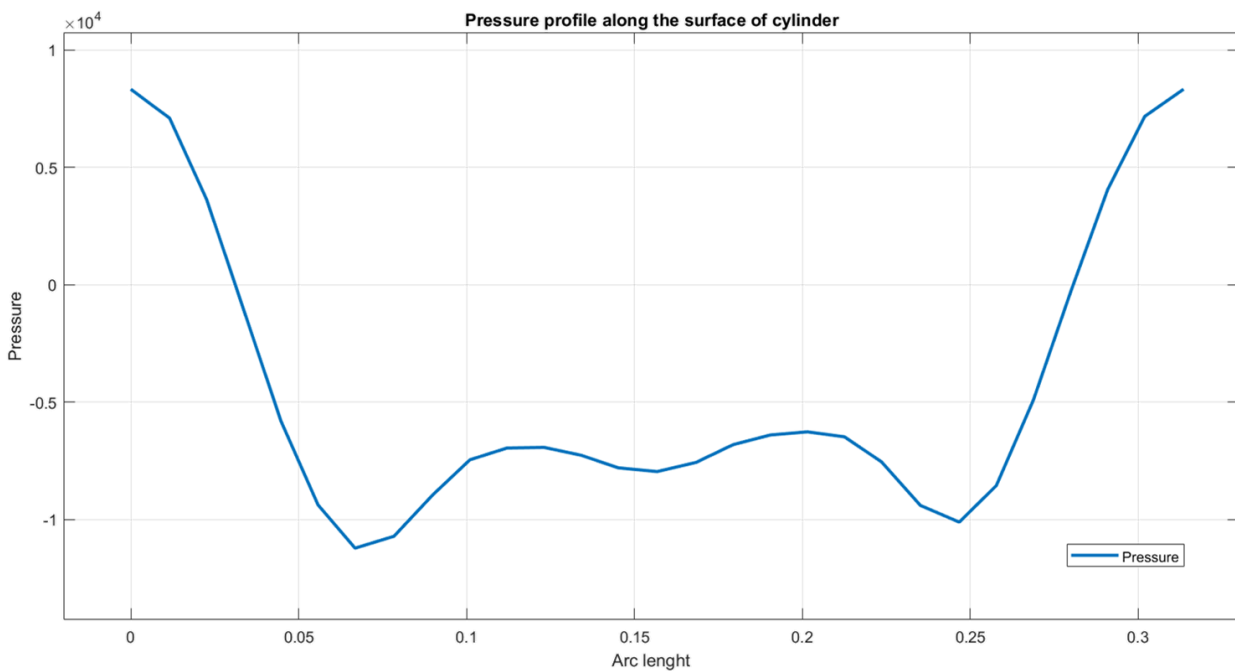


Figure 3.19: Fluid pressure profile along the surface of cylinder.

The projection of the pressure in the direction of the axis gives the contribution of a point to the dragging force, whose total value is calculated by integrating those projections all along the surface of the cylinder. Both the balance between positive pressures on the left side and negative pressures on the right side give the contribution to the dragging force. As the location corresponding to the boundary separation point affects the value of the integral, any factor able to modify such location is could affect the dragging force or, equivalently, the resistance of the obstacle to the fluid motion.

The dragging force is expressed by using the drag coefficient C_d which allows to characterize the force in function of the undisturbed flow velocity and the parameters of the system:

$$F_d = \frac{1}{2} C_d \rho V^2 S \quad (3.3)$$

By calculating the dragging force by means of the above mentioned integral, the (3.3) allows one to determine the drag coefficient C_d . In Fig. 3.20, the above method has been used to trace the time diagram of C_d . At the beginning, the drag coefficient has a peak, which is a consequence of the initial transient and it reduces near to zero in a short time, and then it maintains an oscillating behavior due to the Von Karman eddies. The value of C_d dynamically converges around the value 1.0 which is in agreement with most of the results given in the literature.

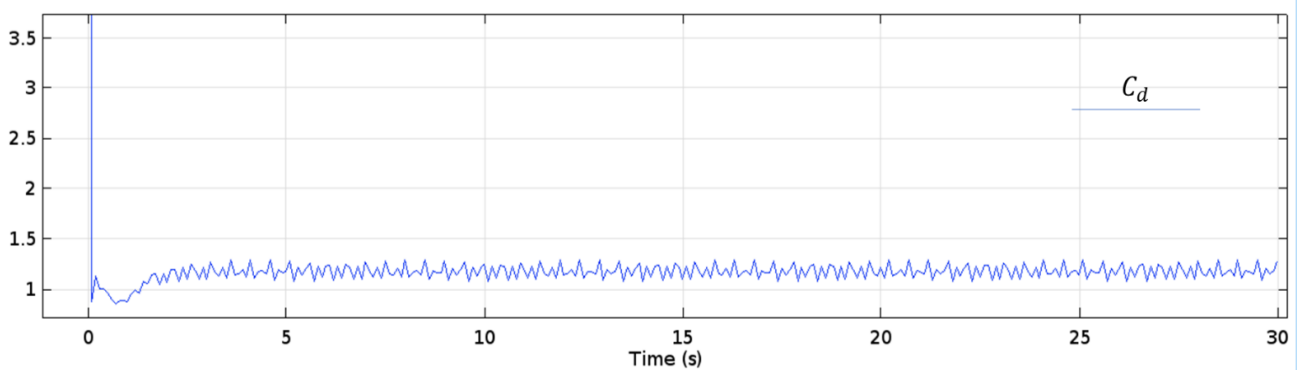


Figure 3.20: Drag coefficient ($V = 1 \text{ m/s}$, $R_e = 1000$)

It is also interesting to see how the axial component of the velocity is distributed upstream and downstream the cylinder. In Fig. 3.21 the profile of the velocity is shown for two distinct cross sections respectively on the left and on the right of the cylinder. The profile upstream the cylinder is affected by the obstacle, slowing down the flow in the axis of the duct, and giving rise to an acceleration close to the wall, to save the continuity. It can be also seen that the walls impose the value of the velocity, which is the same of the undisturbed flow, slowing down slightly the fluid with respect to the maximum velocity near the walls. The profile on the right of the cylinder is

totally different. First of all, the profile is not stationary, due to the presence of eddies. Anyway, for continuity, a positive distribution is always coupled with a negative one. Also in this case, it is possible to see the boundary layers on the walls, which force the fluid to have the same velocity of the undisturbed flow. As it can be seen, the boundary layer is thin with respect to the height of the duct, which supports the hypothesis that the bulk of the flow is slightly affected by the presence of the walls.

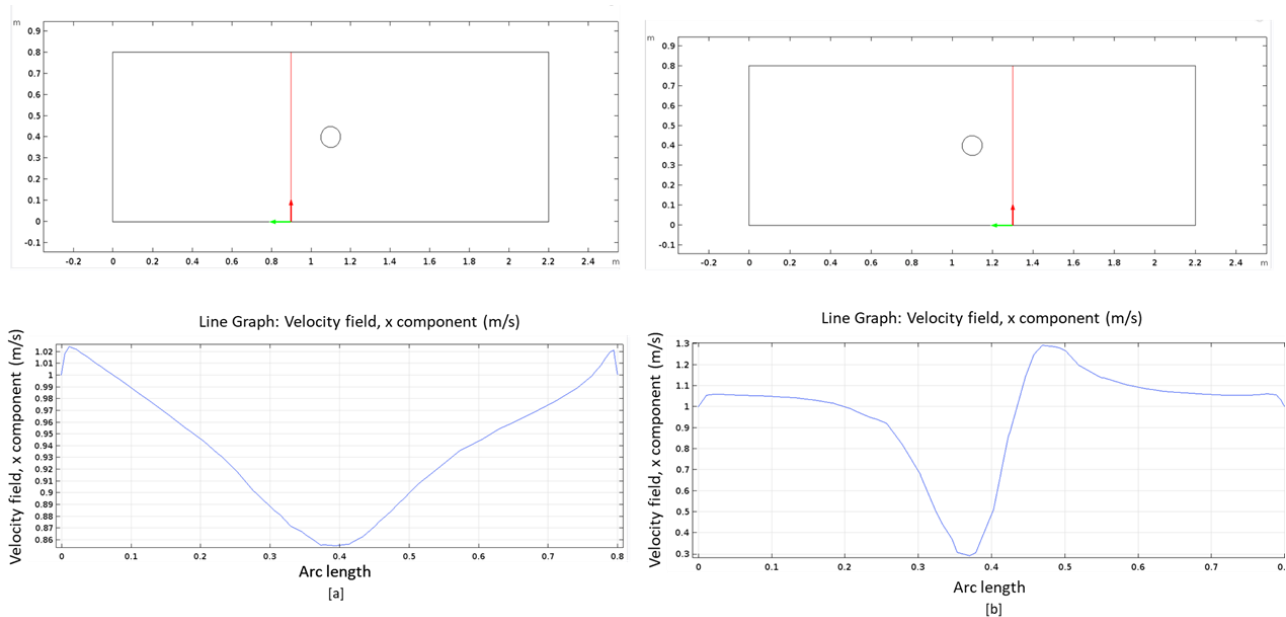


Figure 3.21: Velocity profile upstream [a] and downstream [b] of the cylinder.

To determine the Strouhal number, the frequency of vortex detachment has been evaluated for an appropriate reference time interval (200 s). The obtained rate of two consecutive vortices for second, is in agreement with the results retrieved from the literature [5], where a Strouhal number $S_t = 0.2$, is obtained for $Re = 200, 1000, 10000$ as shown in Table 3.11.

Table 3.11: Tests results.

Re	V_{flu} [m/s]	S_t	Calculated values C_d	Literature values C_d [5]
200	0.2	0.2	1.67	1.45
1000	1	0.2	1	1
10000	10	0.2	1.45	1.35

3.5 Results for small Magnetic Reynolds number

In this section, the results of MHD interaction are reported for different Reynolds numbers and for different values of interaction parameter N . Several cases have been analyzed, by

considering both the case of liquid and cylinder having the same magnetic permeability, and the case of different magnetic permeabilities.

In Table 3.12 and in Table 3.13 the main dimension and dimensionless variables respectively are shown. The density and the dynamic viscosity of mercury have been assumed for the liquid, and the cylinder has been assumed electrically insulating.

Table 3.12: Constant dimension parameters.

Name	Dimension value	Dimensionless value	Description
ρ_{flu}	13700 [kg/m ³]	$\rho'_{flu} = \frac{\rho_{flu}}{\rho_0}$	fluid density
ρ_{cyl}	8000 [kg/m ³]	$\rho'_{cyl} = \frac{\rho_{cyl}}{\rho_0}$	cylinder density
σ_{cyl}	0 [S/m]	$\sigma'_{cyl} = \frac{\sigma_{cyl}}{\sigma_0} = 0$	electrical conductivity of the cylinder
P_o	0 [Pa]		Pressure outlet
ϵ_r		1	Relative permittivity

Table 3.13: Dimension and dimensionless variables.

Name	Dimension value	Dimensionless value	Description
V_0	0.2, 1, 2, 10 [m/s]	0.2, 1, 2, 10	Velocity inlet
μ_d	1.37 [Pa · s]	$\mu'_d = \frac{\mu_d}{D\rho_0 V_0}$	Dynamic viscosity of fluid
$\mu_{r_{flu}}$	1	1	Relative permeability of fluid
$\mu_{r_{cyl}}$	1, 100, 0.01	1, 100, 0.01	Relative permeability of cylinder
σ_{flu}	$4.9 \cdot 10^6, 1 \cdot 10^6, 0.5 \cdot 10^6, 0.1 \cdot 10^6$ [S/m]	$\sigma'_{flu} = \frac{\sigma_{flu}}{\sigma_0}$	Electrical conductivity of fluid
J	$3 \cdot 10^6 \div 3 \cdot 10^8$ [A/m ²]	3÷300	External current density

3.5.1 First case: $M = 1$

This first test describes the magnetohydrodynamic behavior of the system when the cylinder and the fluid have the same magnetic permeability: $M = \mu_{r_{cyl}}/\mu_{r_{flu}} = 1 \Rightarrow \mu_{r_{cyl}} = \mu_{r_{flu}}$.

The distribution of magnetic induction \mathbf{B} , generated by a current I applied in the solenoid is show in Fig. 3.22. As can be seen, the streamlines of magnetic field are not modified inside de cylinder.

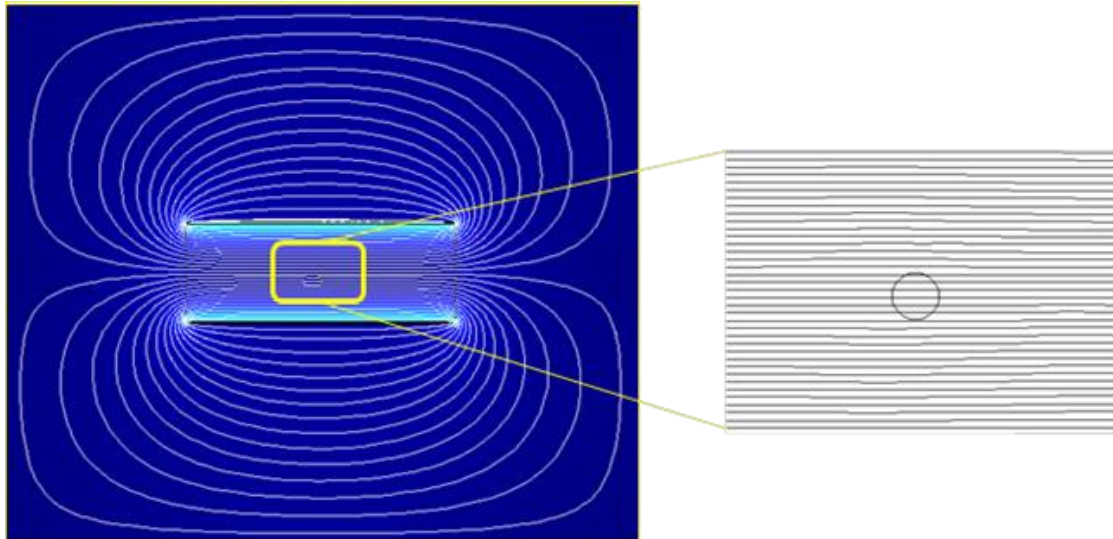


Figure 3.22: Distribution of magnetic field: $\mu_{cyl} = \mu_{flu}$

This analysis has been conducted for the following values of the Reynolds numbers: 200, 1000, 2000, 10000. Some important parameters used in the analysis are reported in the Table 3.14.

Table 3.14: Parameters in the tests

$Re = \frac{D\rho V_{flu}}{\mu_d}$	V_{flu}		σ_{flu}		$R_m = DV_{flu}\sigma_{flu}\mu_0$	$N = \frac{\sigma B^2 D}{\rho V_{flu}}$	$\alpha = \sqrt{\frac{R_m}{N}}$
	[m/s]	w/o dimension $V_{flu} = V_0$	[S/m]	w/o dimension $\sigma_{flu} = \sigma_0$			
200	0.2	0.2	$4.9 \cdot 10^6$	1	0.125	$0.1 < N < N_c$	$0.6 < \alpha < 1.2$
1000	1	1	$1 \cdot 10^6$	1	0.125	$0.1 < N < N_c$	$0.6 < \alpha < 1.2$
2000	2	2	$5 \cdot 10^5$	1	0.125	$0.1 < N < N_c$	$0.6 < \alpha < 1.2$
10000	10	10	$1 \cdot 10^5$	1	0.125	$0.1 < N < N_c$	$0.6 < \alpha < 1.2$

The Reynolds number is modified by changing the velocity and, at the same time, the conductivity of the fluid has been adapted to maintain constant the value of R_m . For sake of comparison with the literature [13], a fixed value of R_m equal to 0.125 has been assumed.

The behavior of fluid flowing at low Reynolds number ($V = 0.2$ [m/s]; $Re = 200$), is shown in Fig. 3.23. Behind the cylinder, the Von Karman's wake formation can be observed, with the presence of alternating vortices in the upper and lower region of the domain, where the velocity of the fluid increases and a central trail of fluid with reduced velocity is formed.

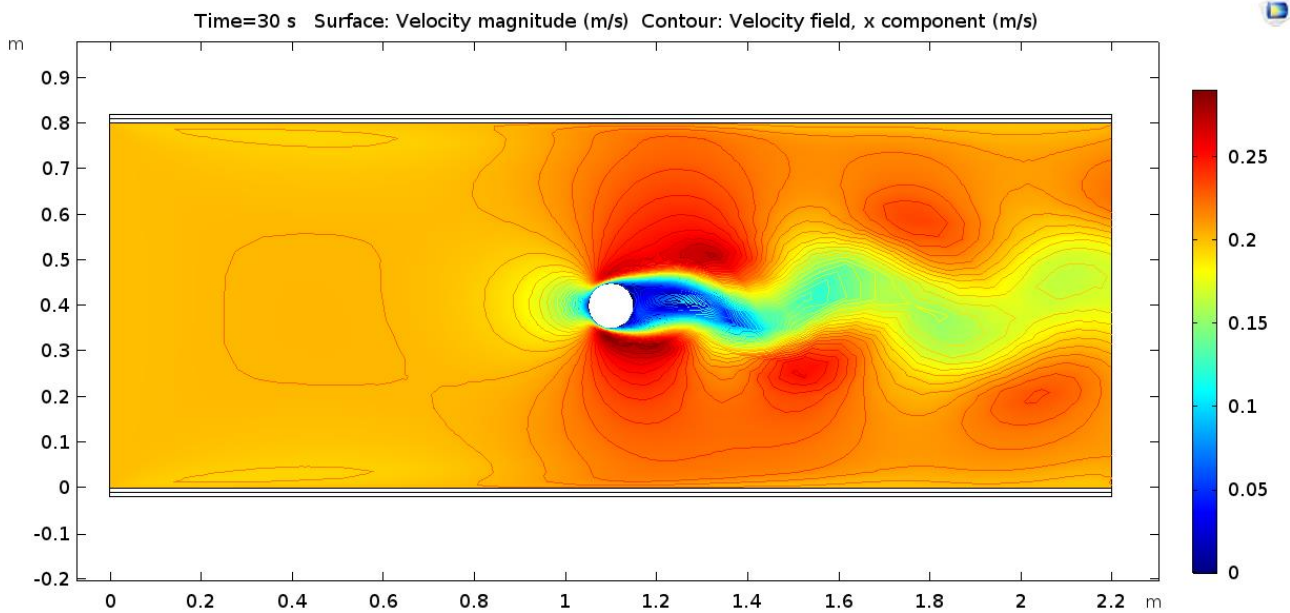
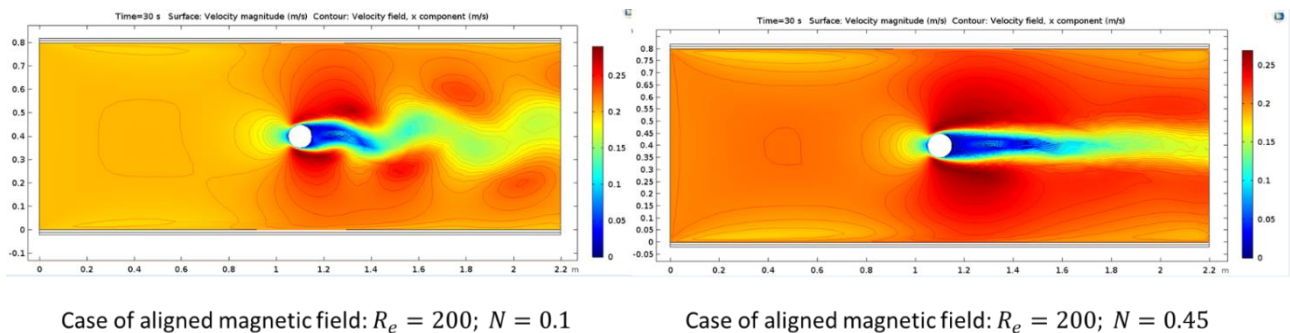


Figure 3.23: Von Karman's wake in the fluid dynamic system ($N = 0$).

A magnetic field aligned with the velocity of the fluid can change the configuration of the system, according to the Reynolds number and the interaction parameter N (see Fig. 3.24).



Case of aligned magnetic field: $R_e = 200$; $N = 0.1$

Case of aligned magnetic field: $R_e = 200$; $N = 0.45$

Figure 3.24: Hydrodynamic configuration modified by magnetic field.

All tests carried out include the study of the system in the following three configurations: a) flow without magnetic field; b) magnetic field with fluid at rest; c) flow and magnetic field together.

In the Multiphysics test, by varying the Reynolds number, a specific value of the magnetic induction \mathbf{B} that depends on the variation of interaction parameter N , has been applied. Furthermore a value of \mathbf{J} has been added in order to find the value of N_c for which eddies disappear.

Finally, for each value of N , also the Strouhal number $S_{tr} = fD/V$, which refers to the frequency of detachment of vortices to form the Von Karman wake, and the Alfven number $\alpha = \sqrt{R_m/N} = V_{flu}/v_a$ (where $v_a = B/\sqrt{\rho\mu}$), have been calculated.

A value of α lower than or close to 1 has been assumed for all the configurations examined. The velocity values are applied along the inlet cross section. The magnetic induction values have been considered in the center of the cylinder. The velocity and magnetic field values have been also checked in different sections upstream and downstream of the cylinder.

In Table 3.15 a glance of the obtained results is given.

Table 3.15: Test results

Re	V_{flu} [m/s]	N	B [T]		S_t		α	Vortices
			$V = 0$	$V > 0$	$B = 0 ; V > 0$	$B, V > 0$	$\sqrt{\frac{R_m}{N}}$	
200	0.2	0.1	0.02352	0.02311	0.185	0.178	1.118	yes
		0.2	0.03306	0.03241		0.166	0.790	yes
		0.3	0.04086	0.04003		0.166	0.645	yes
		0.4	0.04691	0.04618		0.164	0.559	yes
		0.45	0.05129	0.05041			0.527	no
$0.4 < N_c < 0.45$								
1000	1	0.1	0.11863	0.11695	0.2	0.2	1.118	yes
		0.2	0.16554	0.16290		0.166	0.790	yes
		0.3	0.20284	0.19901		0.166	0.645	yes
		0.4	0.23465	0.22985		0.166	0.559	yes
		0.45	0.25022	0.24560			0.527	no
$0.4 < N_c < 0.45$								
2000	2	0.1	0.23503	0.2316	0.2	0.2	1.118	yes
		0.2	0.33183	0.32661		0.166	0.790	yes
		0.3	0.40568	0.39790		0.166	0.645	yes
		0.4	0.46918	0.46036		0.166	0.559	yes
		0.45	0.49911	0.4898			0.527	no
$0.4 < N_c < 0.45$								
10000	10	0.1	1.17272	1.15566	0.2	0.2	1.118	yes
		0.2	1.65941	1.63235		0.1666	0.790	yes
		0.25	1.85013	1.81385		0.1567	0.645	yes
		0.4	2.36827	2.32648		0.1566	0.559	yes
		0.45	2.48957	2.47314			0.527	no
$0.4 < N_c < 0.45$								

The magnetic field slightly decreases as a consequence of induced currents that generate an induced magnetic field \mathbf{b} opposite to the applied one.

The disappearance of vortices occurs when the value of the interaction parameter N is between 0.4 and 0.45. Before reaching the critical value N_c , the vortices stretch and their longitudinal axis rotates until it is aligned with the duct axis.

The Strouhal number for laminar flow is of the order of 0.2 as the literature studies (a little smaller in the case $Re = 200$). The test shows that, after the interaction between the fluid and the magnetic field, the Strouhal number is less than its value measured in the fluid dynamics test; moreover it tends to decrease also when the value of the interaction parameter N increases. It has been observed that the frequency of detachment of the vortices decreases as the field \mathbf{B} increases.

In conclusion, when the cylinder and the fluid have the same permeability, the disappearance of the vortices occurs when N is between 0.4 and 0.45. In all examined cases, the Alfvén number, which depends on the Reynolds Magnetic number and on the interaction parameter N , has a value close to the unit; therefore the velocity of the fluid is close to the Alfvén velocity.

3.5.1.1. Evolution of drag coefficient

For each considered Reynolds number, the trend of the coefficient C_d in the time, and therefore of the dragging force have been observed when the interaction parameter N increases.

The plots in Fig. 3.25, all referring to $Re = 2000$, show respectively, in the time interval $0 < t < 15$, the trend of the coefficient C_d for the laminar flow; subsequently, in the second interval $15 < t < 30$ the variation of C_d during the interaction between the magnetic field and the laminar flow. The dragging force of the fluid on the cylinder exhibits a downward trend for interaction parameter values below the critical value, and a rising trend for values above the critical one.

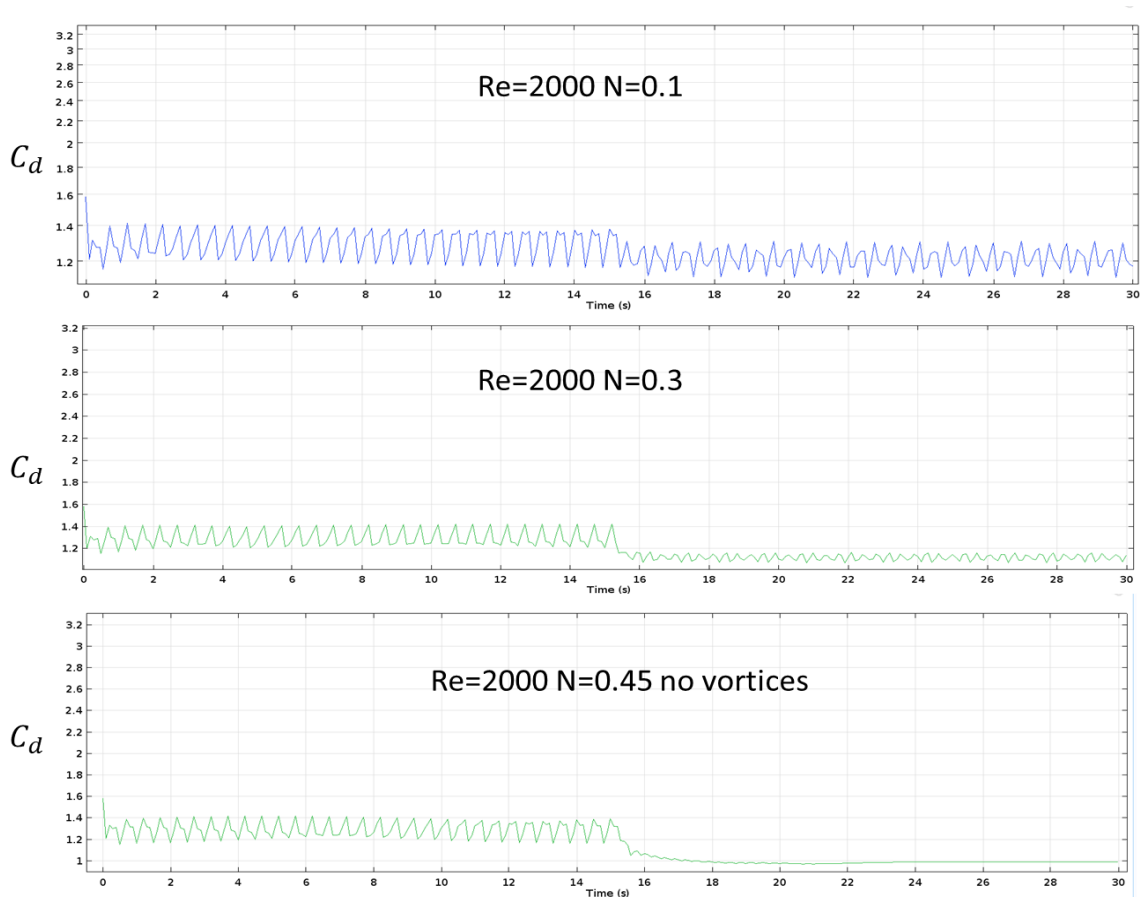


Figure 3.25: C_d coefficient for different values of N when $Re = 2000$.

In Fig. 3.26 the time average of pressure profile along the cylinder surface is reported for different values of the interaction parameter N .

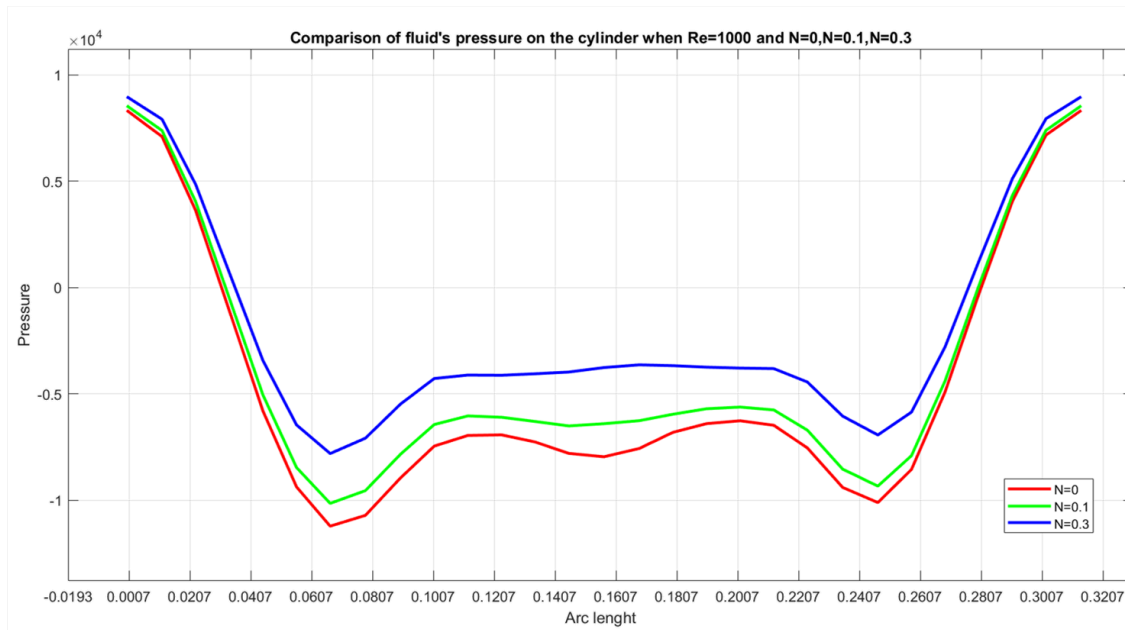


Figure 3.26: Time average of fluid pressures on the cylinder versus N .

Considering that:

$$C_d = \frac{\int_0^{2\pi} P_\theta R \cos\theta d\theta}{\rho V^2}$$

it can be noted that as N and then the applied magnetic field increases, there is a slight increase of upstream pressure, but a more significant decrease of the downstream vacuum, which combined effect give rise to a reduction of the total dragging force.

When the interaction parameter N reaches its critical value N_c and the vortices disappear, the value of C_d is always smaller than or equal to unit.

This trend has been confirmed in all examined tests, for several Reynolds number and when the interaction parameter N increases. The interaction parameter N has been increased up to the critical value, which was always smaller by 0.45 and in some case also the value $N = 1$ was investigated.

Fig. 3.27 shows the results obtained in the present study, in particular the evolution of drag coefficient versus the interaction parameter, for several values of Reynolds number. This last result confirms the literature data [17] for which, for small values of the interaction parameter ($N < 1$), C_d and the dragging force decrease as the interaction parameter N increases (see curves (a) and (b) in Fig. 3.27).

Until reaching the range of variability of the critical value of N the dragging force decreases when the interaction parameter N increases; above this value, the dragging force increases with N .

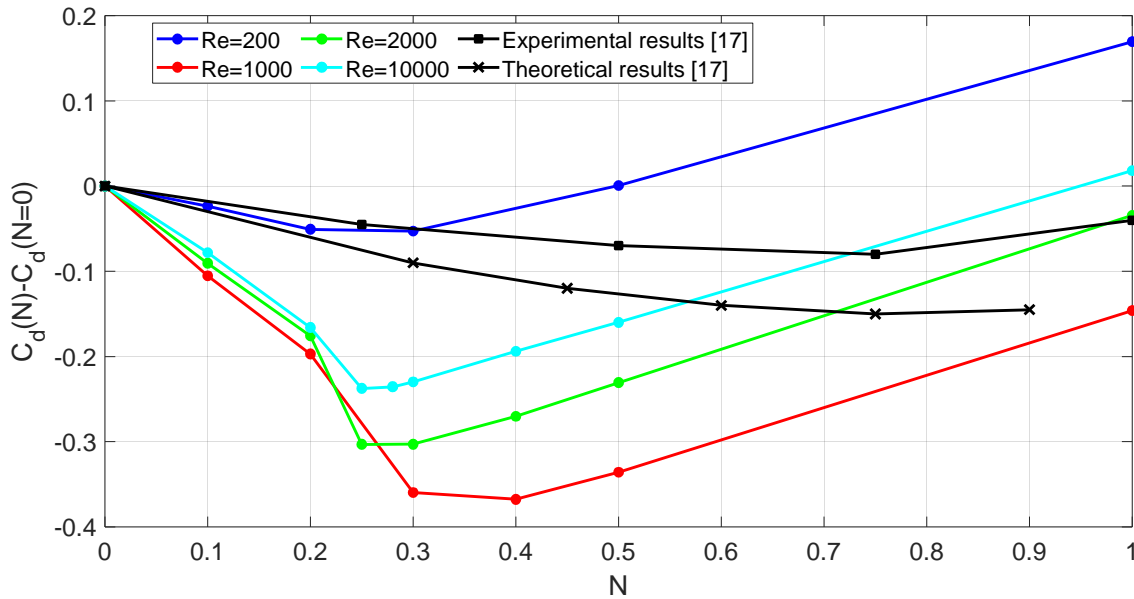


Figure 3.27: Trends of the drag coefficient for several Reynolds number versus interaction parameter N compared with experimental (a) and theoretical (b) results [17].

As can be noted in Fig. 3.28, the C_d evolution for $N = 20$ when $Re = 1000$ exhibits a trend still growing for big values of N .

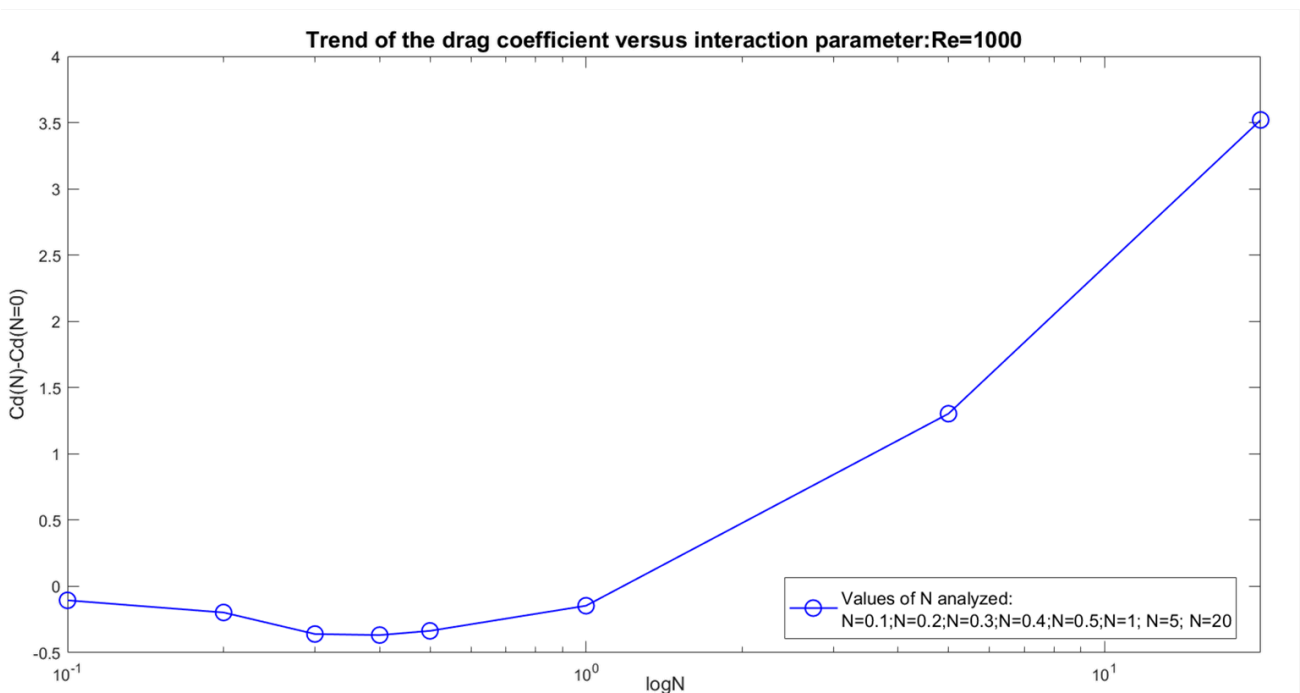


Figure 3.28: Trends of the drag coefficient versus interaction parameter for $Re = 1000$.

Neglecting the influence of the viscosity externally to the boundary layer and taking into account the rotational of the linearized form of the Navier Stokes equations under the steady state

hypothesis, the simple expression connecting the y component of the velocity to the vorticity ω is given:

$$\frac{\partial \omega}{\partial x} = -N \left(\frac{\partial V'_y}{\partial x'} + O(R_m) \right) \mathbf{k}$$

from which, assuming $\omega = 0$ at infinity, we obtain:

$$\omega = -N(V'_y + O(R_m)) \mathbf{k}$$

This trend depends to the presence of electromagnetic forces that generate the vorticity on the fluid. For very small values of Magnetic Reynolds number $R_m = b/B \ll 1$ we obtain

$$N = \frac{B^2 D \sigma}{\rho V} = R_m / \alpha^2 \ll 1.$$

The vorticity increases the fluid velocity downstream of the cylinder and decreases it upstream, as shown in Fig. 3.29. This phenomenon produces a downstream displacement of the separation point of the boundary layer in which results a decreasing in the drag coefficient. For large value of N this phenomenon is not visible. For higher values of N the increasing of pressure upstream, due to the electromagnetic forces, dominates the drag evolution which increases when N increases.

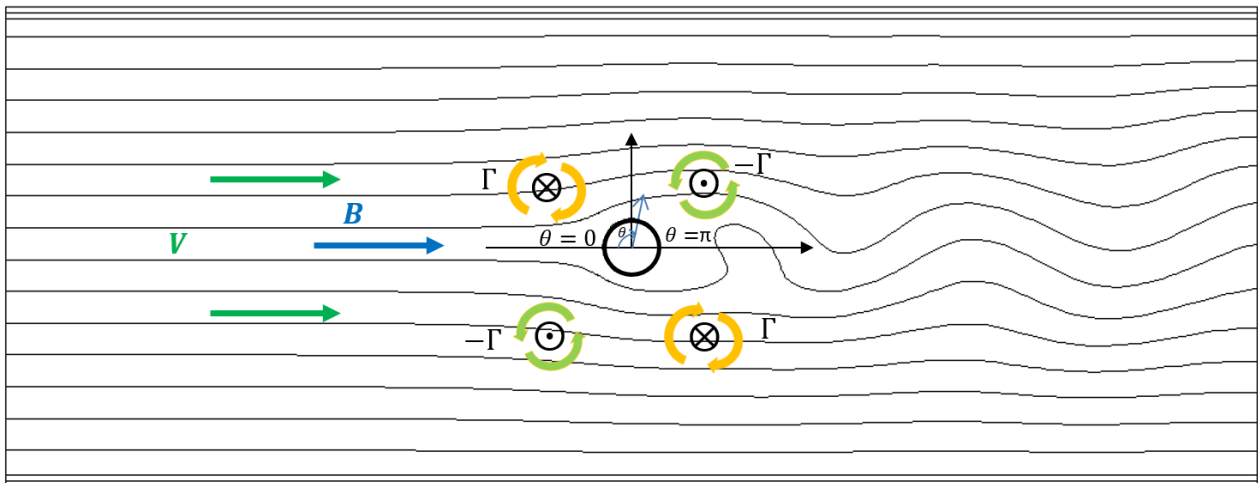


Figure 3.29: Distribution of vorticity for small values of N

3.5.1.2 Evolution of detachment point

In the Fig. 3.30 the detachment angles, calculated for N equal to 0, 0.1, 0.2, 0.3, 0.4, 1 and 20, are shown.

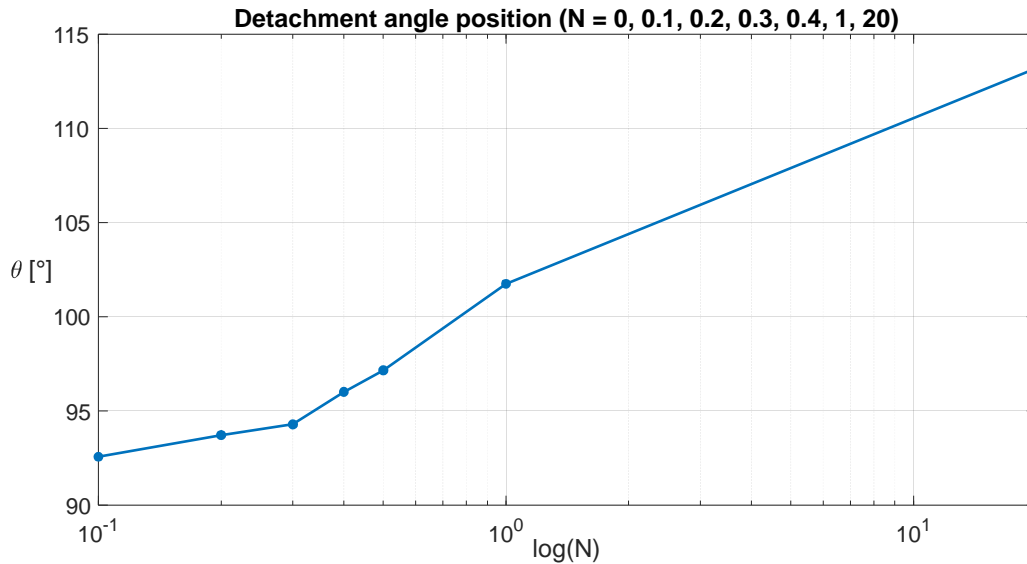


Figure 3.30: Angular position of the boundary layer separation point from the stagnation point

The separation point corresponds to the location on the surface where the derivative in the radial direction of tangential velocity becomes null. These values have been obtained, for each value of N , through the analysis of the tangential velocities in a time interval controlled by the Strouhal number.

It has been observed that for very small values of the interaction parameter N the oscillations of the separation point are very strong (see Fig. 3.31). These decrease when N increases to stabilize when N reaches its critical values ($0.4 < N < 0.45$).

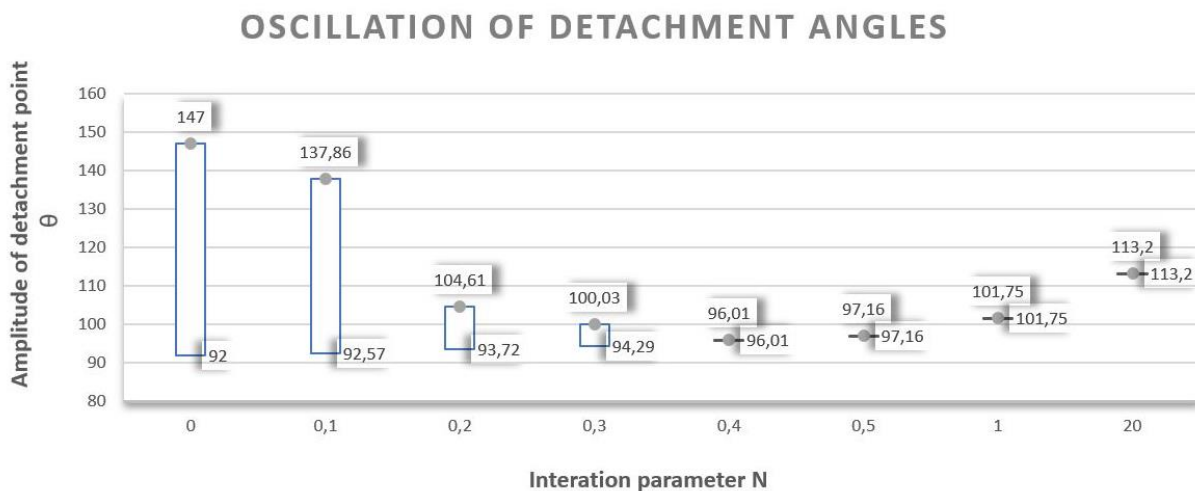


Figure 3.31: Oscillation of detachment point versus N .

The evolution of tangential velocity of fluid was also analysed in case $N = 20$, for which the angular position of the detachment point was 113° . Considering that from $N = 1$ to $N = 20$ the angle increases only by 12° , this result could confirm that for large values of N the angle of separation point of the fluid tend to be constant.

In spite the fact that the angle of detachment point is monotonic with N , one can observe that this is not the behaviour of the dragging coefficient. This is due to the fact that the vacuum behind the cylinder, due to the detachment of the vein fluid (Fig. 3.32), is not the only phenomenon that causes the dragging force. A second phenomenon, due to the interaction between magnetic field and fluid velocity, is also responsible of the dragging force.

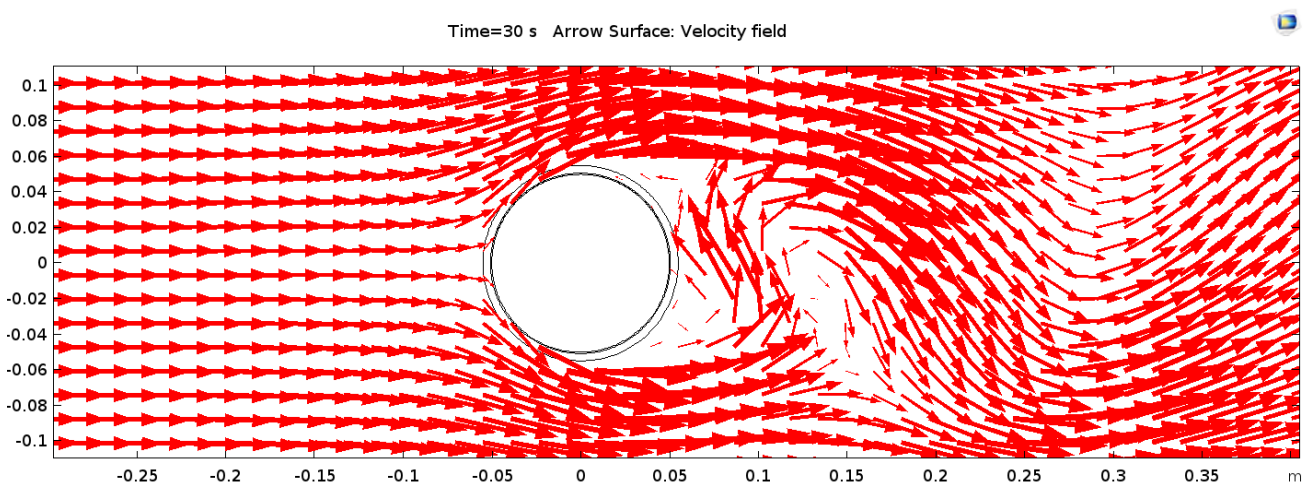


Figure 3.32: fluid vein detachment mechanism.

This phenomenon is depicted in Fig. 3.33. As the streamlines of the fluid reaches the cylinder, they are forced to turn, assuming a vertical component of the velocity. This interacts with the magnetic field, giving rise to a reaction force, which pushes the fluid towards the axis of the duct (down in the top, up in the bottom). This produce an over pressure upstream the cylinder, which is not present for null or weak magnetic fields, and that is not compensated by a corresponding pressure downstream the cylinder, as in this region the fluid is not obliged to follow a trajectory with a vertical direction. For high values of N , which means high magnetic field, this force of electromagnetic nature becomes predominant with respect to the dragging force of fluid dynamic

origin, and this explains the trend of the observed trend of the dragging coefficient with respect to the interaction parameter N .

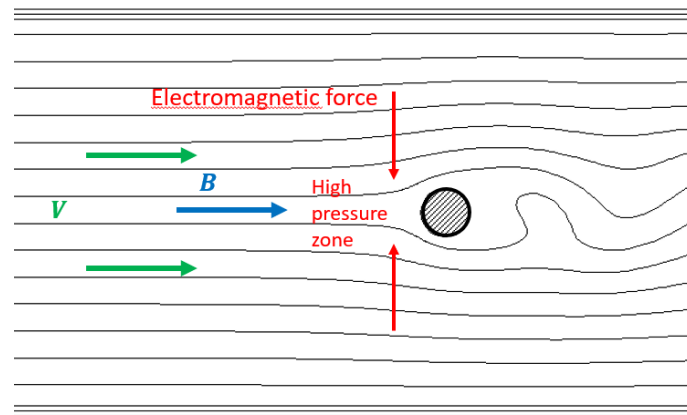


Figure 3.33: Elettromagnetic force effect.

To summarize, the evolution of the drag versus the interaction parameter depends on the overlap of two phenomena: for small N the displacement of the boundary layer separation point reduce the size of the wake downstream that tend to diminishing the drag but for high value of N the improvement of the pressure up stream tends to increase the drag and becomes dominant.

3.5.1.3 Cavity at low velocity of fluid

In all studied configurations, the formation of a cavity, downstream of the cylinder, characterized by low values of the velocity of fluid, was observed after the disappearance of the vortices, for $N > N_c$. In fact, at the frontier of the cavity, due to the effect of the viscosity, the internal fluid is driving by the external part. The stream lines are closing on the form of a vortex formed inside the cavity on both part (upper and lower) of the central axis.

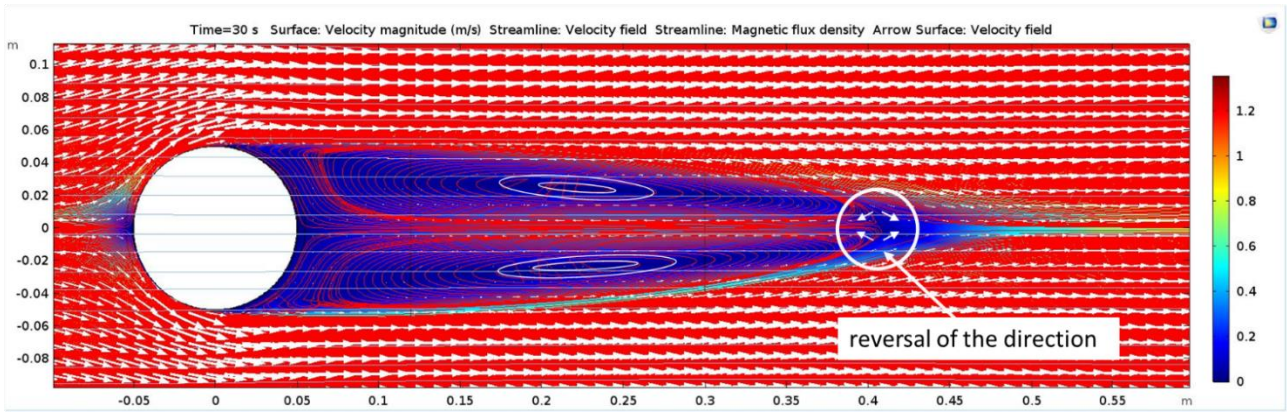


Figure 3.34: Cavity and stagnation point of velocity in case $R_e = 1000$ for $N = 1$.

In the Fig. 3.35 and 3.36, the streamline of velocity and magnetic field, inside and outside the cavity, in case in case $R_e = 1000$, for $N = 5$ and for $N = 20$, are shown. It can be observed that the velocity stream lines tend to follow the magnetic stream lines taking a parallel direction.

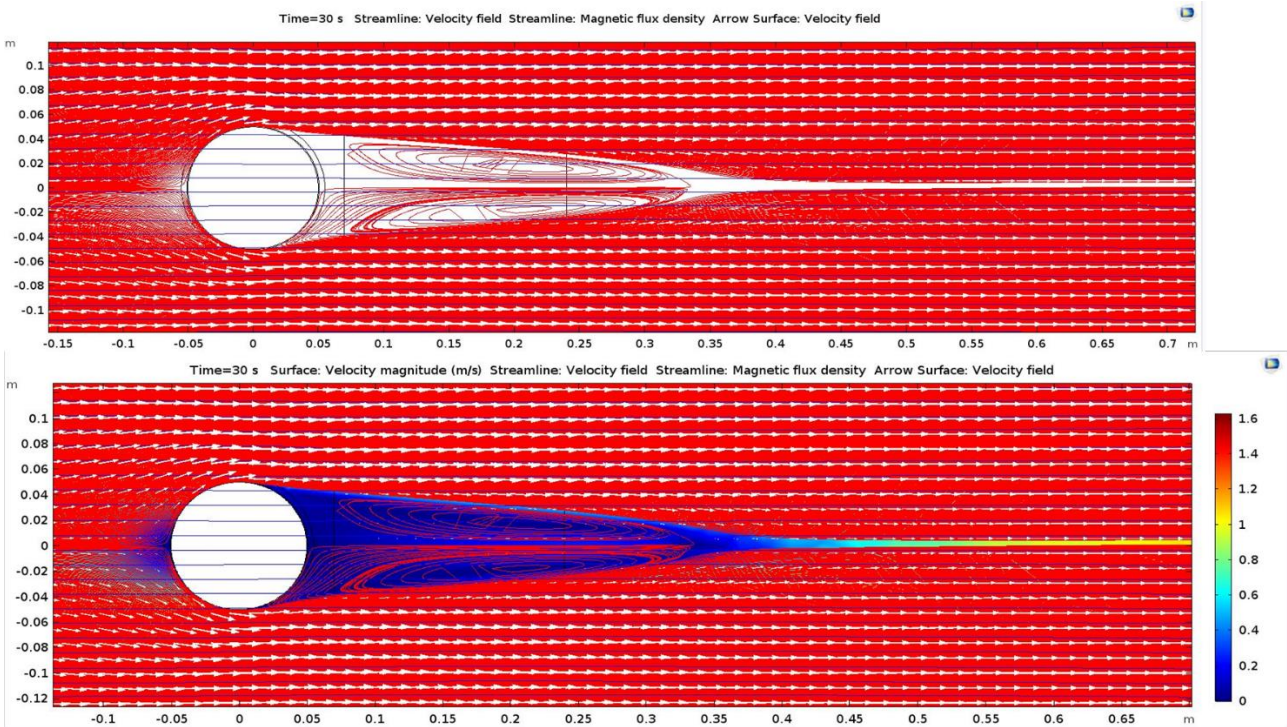


Figure 3.35: Streamline of velocity and magnetic field inside and outside the cavity for $N = 5$

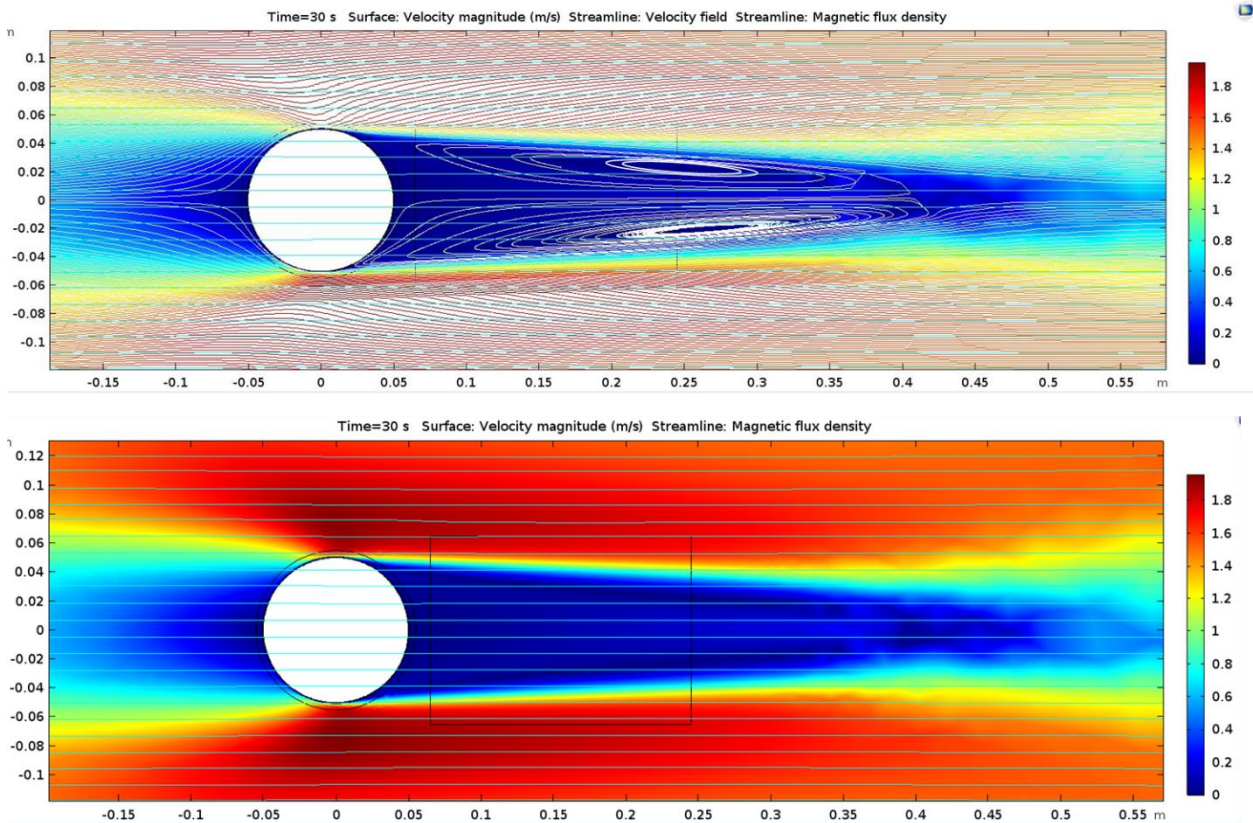


Figure 3.36: Streamline of velocity and magnetic field inside and outside the cavity for $N = 20$

3.5.2 Dependency of the interaction parameter N on fluid confinement

In this analysis, the confinement condition of the fluid is modified, in order to evaluate the effects on the hydrodynamics of the flow, in particular on the critical value of the interaction parameter. The test parameters are shown in the Table 3.16.

Table 3.16: Main parameters of test

$Re = D\rho V_{flu} / \mu_d$	$V_{flu} [m/s]$	$\sigma_{flu} [S/m]$	$R_m = DV_{flu}\sigma_{flu}\mu_0$
10000	10	10^5	0.125

Three different studies have been performed, in correspondence to as many values of the aspect ratio, $C = \frac{D}{H}$ (Table 3.17).

Table 3.17: Values of the duct height

Domain height	Value [units]	$C = D/H$
H	0.3 [m]	$0.1/0.3 = 0.5$
	0.45 [m]	$0.1/0.45 = 0.22$
	0.8 [m]	$0.1/0.8 = 0.125$

Two configurations of system, when $H = 0.3$, are shown in Fig 3.37. For $N = 0.25$ (Fig 3.37[a]), the magnetic field is not able to modify the fluid-dynamic configuration, while when B rises and $N = 0.7$ (Fig 3.37[b]), the vortices disappear completely.

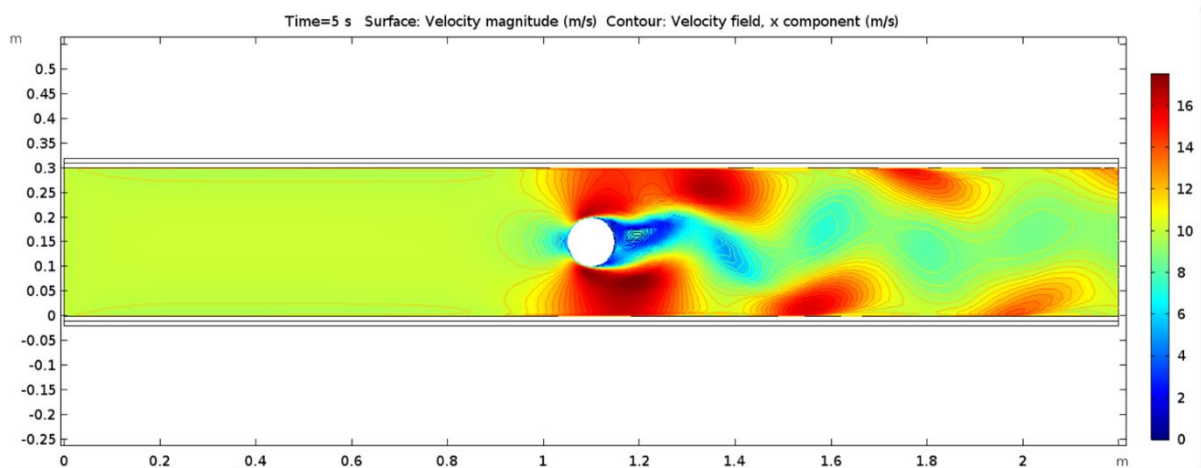
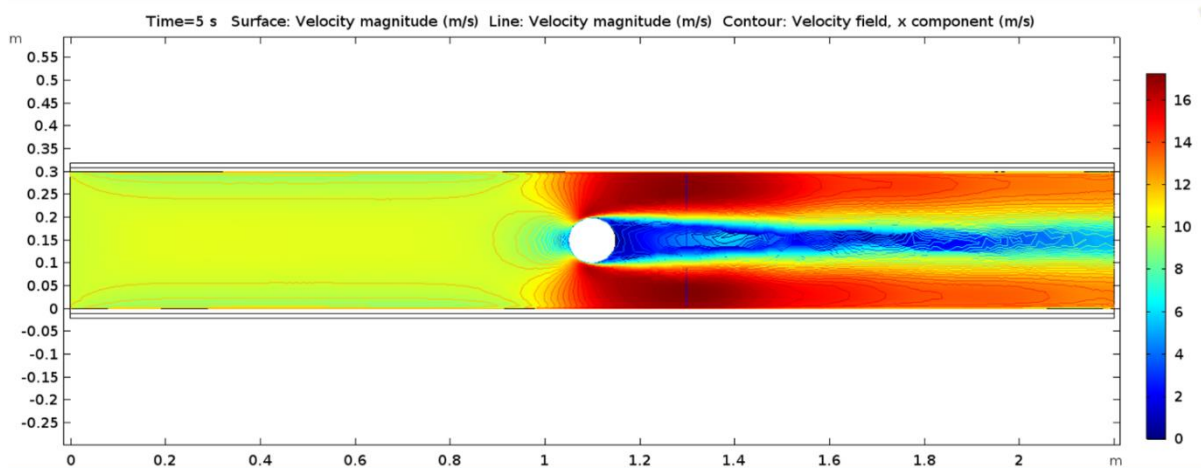
[a] Fluid with an aligned magnetic field. $Re=10000$; $N=0.25$ [b] Fluid with an aligned magnetic field. $Re=10000$; $N=0.7$

Figure 3.37: Interactions Magneto Fluid Dynamic.

The tests results for three configurations in Table 3.17 are shown in Table 3.18, where it can be seen that the critical value of interaction parameter N_c ranges from 0.25 to 0.7.

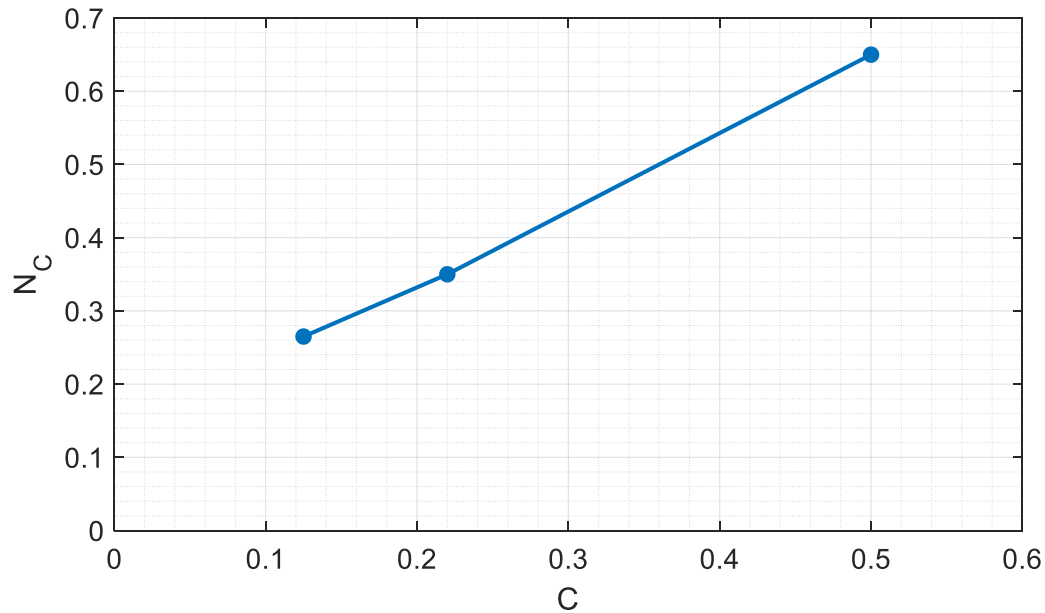
Table 3.18: Test results

R_e	N	V_{flu}	R_m	B		S_t		H	C $C = \frac{D}{H}$	α $\sqrt{\frac{R_m}{N}}$	Vortices
				$V = 0$	$V > 0$	$B = 0$	$B > 0$				
10000	0.1	10	0.125	1.1727	1.1548	0.2	0.2	0.8	0.125	1.118	Yes
	0.2			1.6594	1.6313		0.166			0.790	Yes
	0.25			1.8501	1.8128		0.156			0.707	Yes
	0.28			1.9690	1.9281					0.668	No
$0.25 < N_c < 0.28$											
10000	0.25	10	0.125	1.7056	1.684	0.2	0.2	0.45	0,22	0.707	yes
	0.3			2.0277	2.000		0.2			0.645	yes
	0.4			2.3409	2.304					0.559	no
$0.3 < N_c < 0.4$											
10000	0.25	10	0.125	1.8504	1.8341	0.25	0.25	0.3	0.5	0.707	yes
	0.4			2.3666	2.3431		0.25			0.559	yes
	0.5			2.61581	2.5890		0.25			0.5	yes
	0.6			2.85897	2.8296		0.2			0.456	<i>aligned with the axis</i>
	0.7			3.09723	3.0654					0.422	no
$0.6 < N_c < 0.7$											

In the following, the variability of N_c when the value of C increases, is analyzed.

Table 3.19: Evolution of critical value of N with the height of domain.

H	$C = \frac{D}{H}$	N_c
0.8 [m]	0.125	$0.25 < N_c < 0.28$
0.45 [m]	0.22	$0.3 < N_c < 0.4$
0.3 [m]	0.5	$0.6 < N_c < 0.7$

**Figure 3.38:** Evolution of N_c with the growth of C .

The critical value N_c of the interaction parameter grows with C .

The tighter the confinement of fluid, the larger the parameter N (then the magnetic field) required to suppress the vortices.

The dependencies of the C_d parameter on the fluid confinement and on the interaction parameter N are shown in the following. The cases with $N = 0.25$ for the three cases of confinement considered, $H = 0.8 \text{ m}$, $H = 0.45 \text{ m}$, $H = 0.3 \text{ m}$ are shown in Figg. 3.39, 3.40 and 3.41.

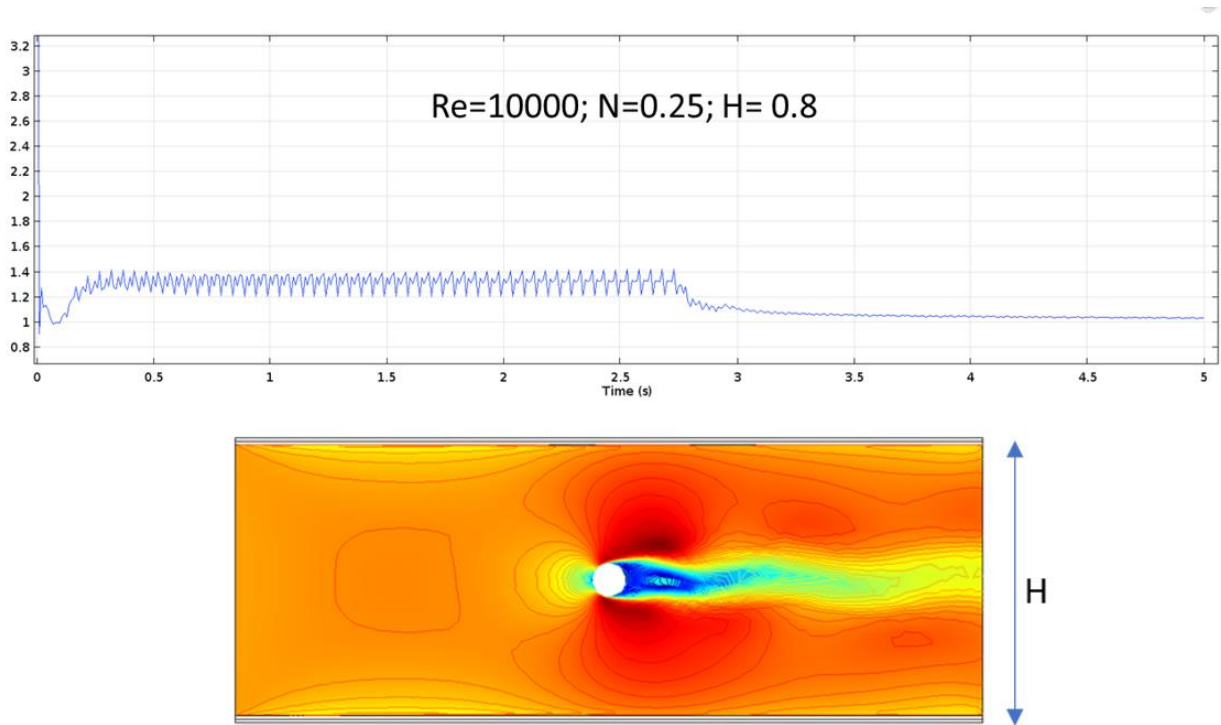


Figure 3.39: Values of C_d for $H = 0.8 m$.

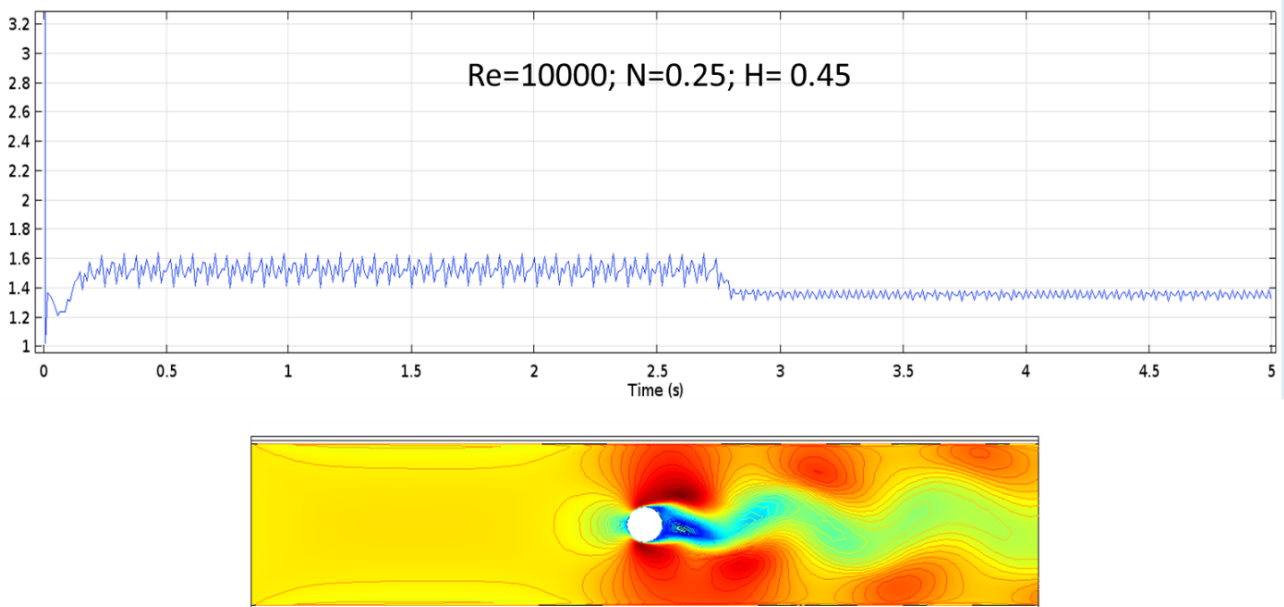


Figure 3.40: Values of C_d for $H = 0.45 m$.

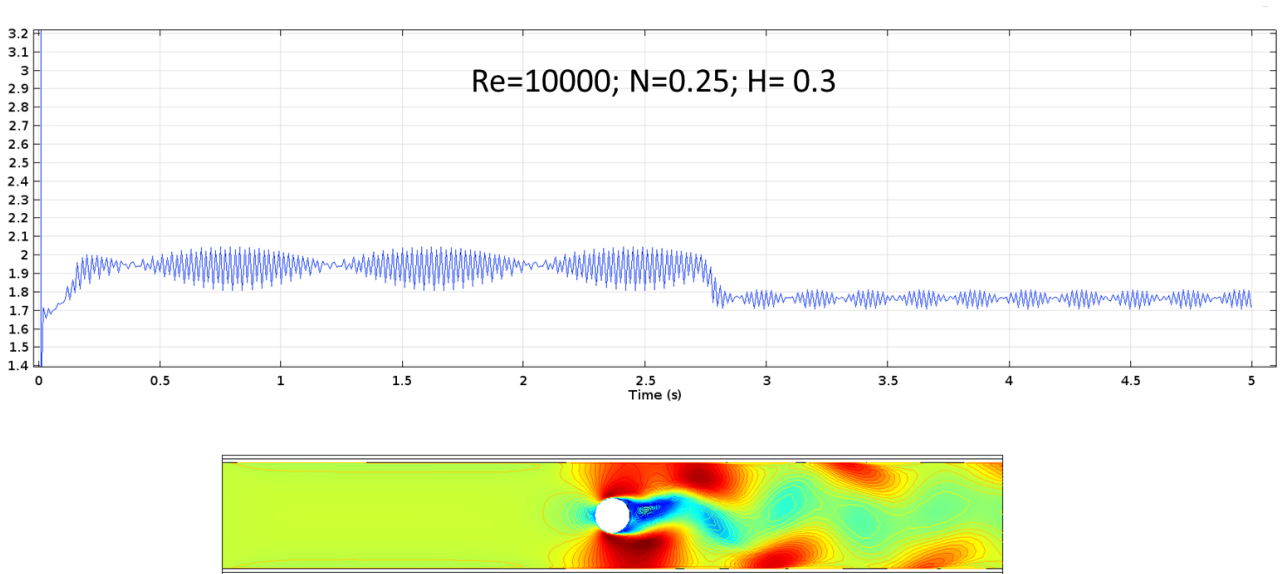


Figure 3.41: Values of C_d for $H = 0.3 m$.

The figures show that, when the confinement increases, keeping the interaction parameter N constant (for $N=0.25$ the magnetic field reduces the vortices but it is not yet able to extinguish them completely), so B constant, the value of the C_d coefficient increases. This means that the dragging force is affected by the presence of walls and by their distance. On the other hand, one can observe that the dragging coefficient grows with the ratio C also when no magnetic field is applied. This is due to the fact that as C grows, the ratio between the crossing areas before and in correspondence of the cylinder diminishes, and then the velocity of the fluid, over and under the cylinder, must be higher for the continuity of the flow. Anyway, it is worth to note that the effect of magnetic field on the C_d , namely the ratio between the values with and without the magnetic field, is lowered by the confinement. On the other hand, it has been shown above that the critical value of the interaction parameter N grows with C , which means that the low values of the height H , the Von Karman street is not yet completely extinguished for the applied magnetic field. As a conclusion, one can state that the confinement affects the way how the magnetic field changes the dragging coefficient, and that higher values of the interaction parameter N are needed to obtain the same reduction.

It can be also noted that, when $H = 0.3 m$, the ripple of the dragging coefficient is modulated by a low-frequency function. A resonance phenomenon is occurring, which is caused by the combination of the geometrical parameters of the system and the characteristics of the fluid. It can be also observed that the effect of the magnetic field is to reduce the modulating amplitude and to increase the frequency, as if increases the stiffness of the system. A complete understanding of this phenomenon requires an in-depth analysis, which is beyond the scope of this study.

3.5.3 Second case: $M = 1000$

In this second configuration, with $M = \mu_{r_{cyl}}/\mu_{r_{flu}} = 1000$, each test of the system, with $Re = 200$, $Re = 1000$ and $Re = 10000$, as in the first case, is studied in the three above described configurations: a) flow without magnetic field, b) magnetic field with fluid at rest, c) flow and magnetic field together.

When the magnetic permeability of the cylinder is greater than that of the fluid, magnetic field streamlines converge inside the cylinder (see Fig. 3.42).

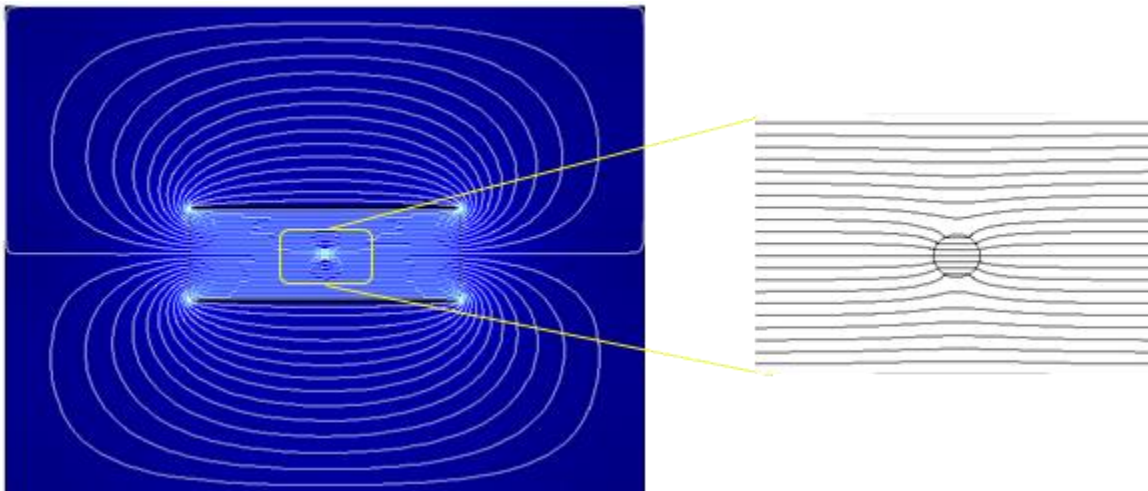


Figure 3.42: Distribution of magnetic field \mathbf{B} when $\mu_{cyl} > \mu_{flu}$.

As a reference value of magnetic field the average value of induction field \mathbf{B} in a vertical section of the domain, upstream of cylinder, is assumed.

The main parameters in Table 3.14 are maintained; the conductivity of fluid is modified to maintain the value of Reynolds Magnetic number constant: $R_m = DV_{flu}\sigma_{flu}\mu_0 = 0.125$.

Table 3.20: Main parameters of the test

$Re = D\rho V_{flu} / \mu_d$	V_{flu} [m/s]	σ_{flu} [S/m]	$R_m = DV_{flu}\sigma_{flu}\mu_{flu}$	$N = \sigma B^2 D / \rho V_{flu}$	$\alpha = \sqrt{\frac{R_m}{N}}$
200	0.2	$5 \cdot 10^6$	0.125	$0.1 < N < N_c$	$0.6 < \alpha < 1.2$
1000	1	$1 \cdot 10^6$	0.125	$0.1 < N < N_c$	$0.6 < \alpha < 1.2$
2000	2	$5 \cdot 10^5$	0.125	$0.1 < N < N_c$	$0.6 < \alpha < 1.2$
10000	10	$1 \cdot 10^5$	0.125	$0.1 < N < N_c$	$0.6 < \alpha < 1.2$

Also Alfven's number values do not change for the corresponding N values of the previous test. The results are show in the follow Table 3.21.

The results show that, when the magnetic permeability of the fluid is less than that one of the cylinder, the critical value of interaction parameter is reached for smaller values with respect to the case of same permeability of fluid and cylinder. In fact, when the magnetic permeability of cylinder is strong enough, the magnetic field near the cylinder increases and its effect of interaction with the vortices is evident earlier.

In this test, the Strouhal number appears to be constant for different values of Reynolds number. The critical value of N is always reached for $0.25 < N < 0.4$, so there is no evidence of the effect on the Strouhal number when B increases.

Table 3.21: Test results.

Re	$V_{flu}[\text{m/s}]$	N	$B [\text{T}]$		S_t		α	Vortices
			$V = 0$	$V > 0$	$B = 0;$ $V > 0$	$B, V > 0$	$\sqrt{\frac{R_m}{N}}$	
200	0.2	0.1	0.023906	0.023893	0.185	0.166	1.118	yes
		0.2	0.033110	0.033096			0.790	yes
		0.25	0.037010	0.036910			0.707	yes
		0.3	0.040558	0.040404			0.645	no
		$0.25 < Nc < 0.3$						
1000	1	0.1	0.117123	0.117081	0.2	0.1666	1.118	yes
		0.15	0.143338	0.143275			0.790	yes
		0.2	0.165584	0.165088			0.790	yes
		0.3	0.201077	0.199963			0.707	yes
		0.4	0.234043	0.23364	0.645	no		
$0.3 < Nc < 0.4$								
2000	2	0.1	0.234175	0.234058	0.2	0.1666	1.118	yes
		0.15	0.286775	0.286643			0.790	yes
		0.25	0.369867	0.369747			0.707	yes
		0.3	0.409457	0.407817			0.645	no
		$0.25 < Nc < 0.3$						
10000	10	0.1	1.170437	1.169775	0.2	0.1666	1.118	yes
		0.15	1.434309	1.433578			0.790	yes
		0.25	1.893800	1.647063			0.707	yes
		0.3	2.058287	2.0489191			0.645	no
		$0.25 < Nc < 0.3$						

One diagrams of the Cd coefficient for this second case of study are given below in case $Re = 10000$.

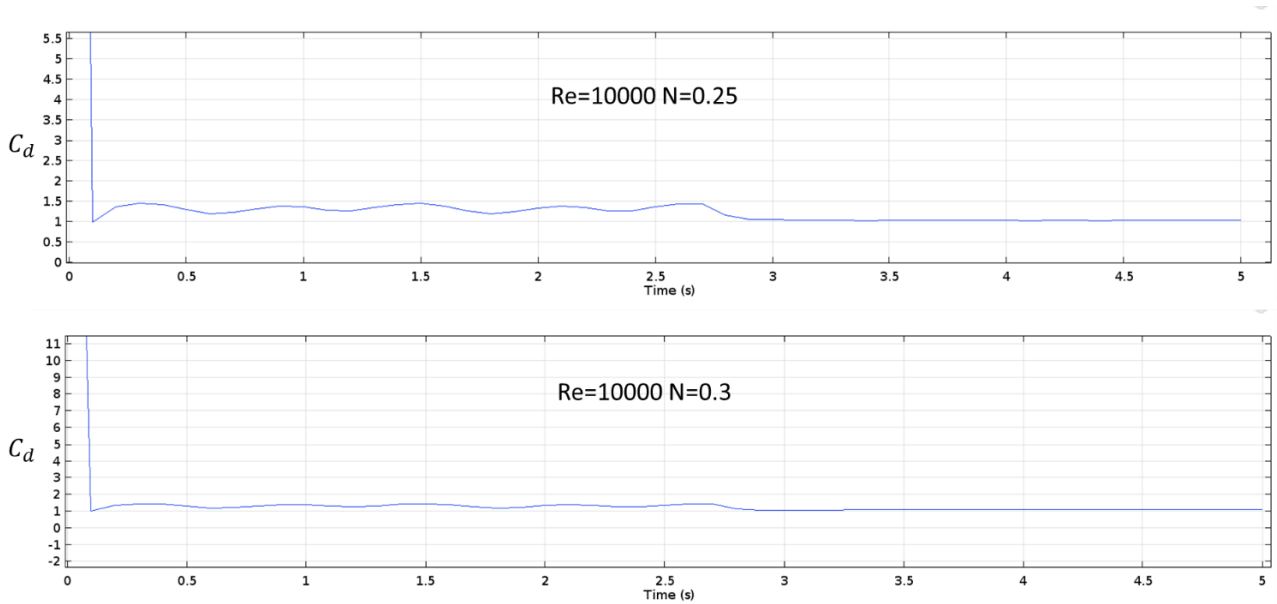


Figure 3.43: C_d coefficient for $Re = 10000$.

The magnetic field brings C_d close to the value of the unit. In Fig. 3.44 can be observed that the behavior is analogous to the previous case: fixed Re , C_d decreases when the interaction parameter N increases, namely when the magnetic induction rises.

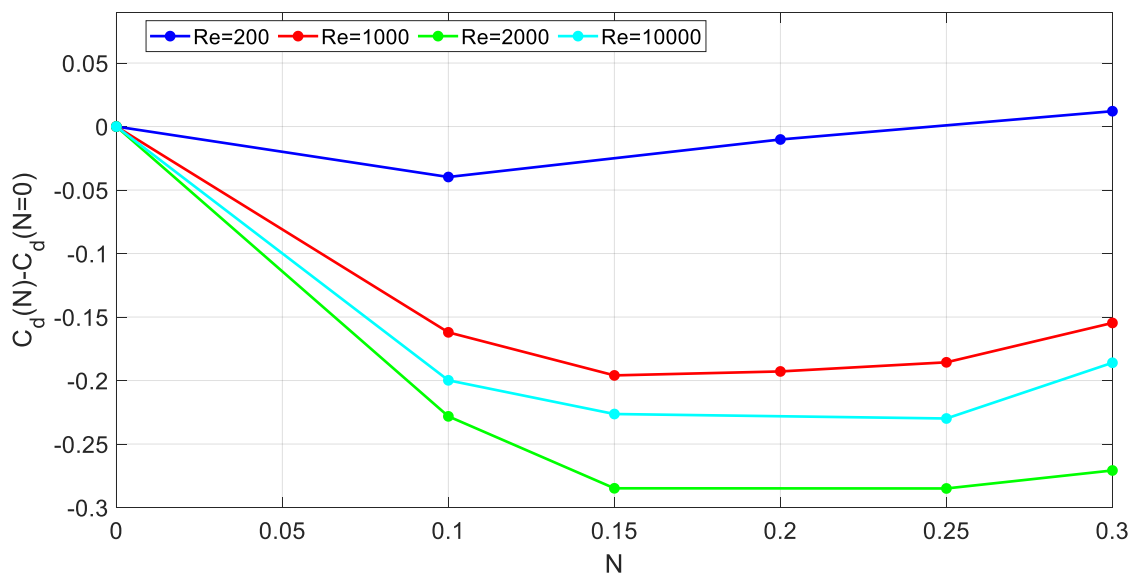


Figure 3.44: Evolution of the drag coefficient versus the interaction parameter

The configuration of the cavity in case $Re = 1000$ and $N = 0.4$ is shown in Fig. 3.45.

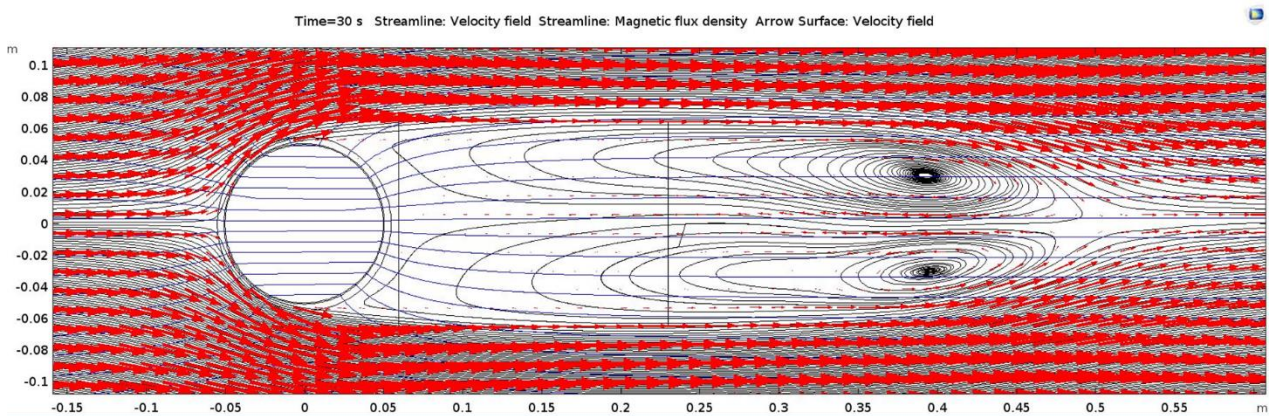


Figure 3.45: Streamline of velocity and magnetic field inside and outside the cavity for $N = 0.4$

3.5.4 Third case: $M = 1/100$

This configuration, with $M = \mu_{r_{cyl}}/\mu_{r_{flu}} = 0.01$, shows the behavior of system when the magnetic permeability of fluid is 100 times larger than that of the cylinder. In particular we impose:

$$\mu_{r_{flu}} = 1, \text{ and } \mu_{r_{cyl}} = 1/100$$

Each test of the system, with $Re = 200$, $Re = 1000$ and $Re = 10000$, has been studied in the three above-described configurations a), b) and c). In this case, magnetic field streamline tend to come out of the cylinder (see Fig 3.46).

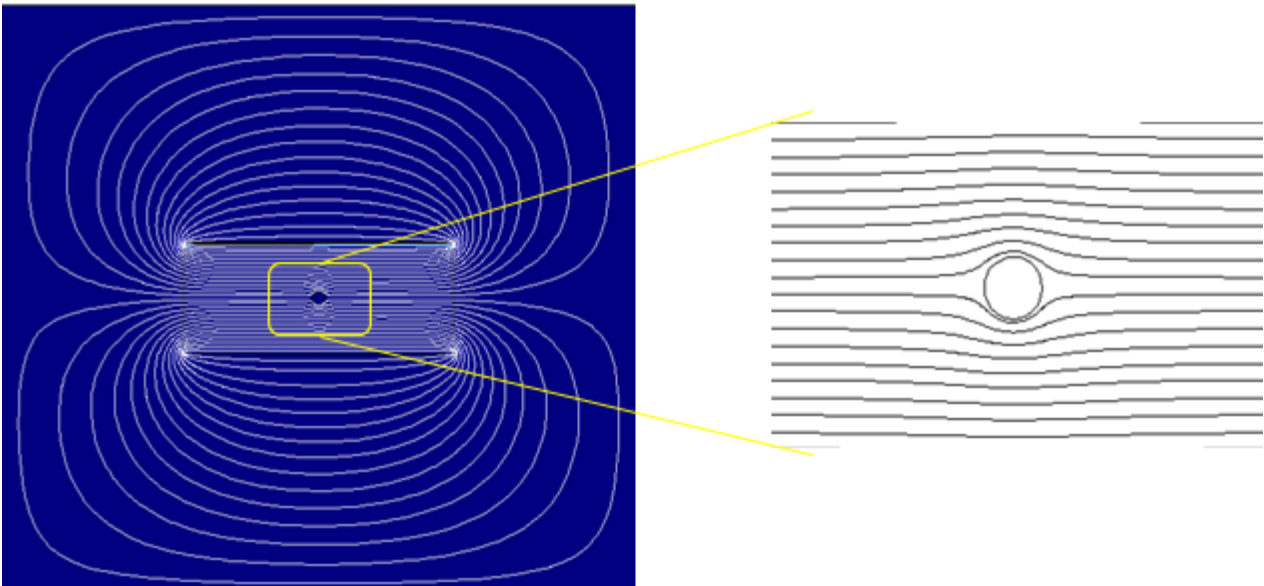


Figure 3.46: Distribution of magnetic field \mathbf{B} when $\mu_{cyl} < \mu_{flu}$

By maintaining the same operating conditions as in the previous tests, the values of magnetic field have been calculated as the average of the values of magnetic field **B** in a vertical section of the domain upstream of the cylinder.

For different values of the Reynolds number, different values of conductivity are considered, in order to maintain constant the value of Reynolds Magnetic number: $R_m = DV_{flu}\sigma_{flu}\mu_{flu} = 0.125$. Also, the reference values of Alfven number are the same as in previous tests.

The main parameters are show in the Table 3.22.

Table 3.22: Main parameters of the test

$Re = D\rho V_{flu} / \mu_d$	V_{flu} [m/s]	σ_{flu} [S/m]	$R_m = DV_{flu}\sigma_{flu}\mu_{flu}$	$N = \sigma B^2 D / \rho V_{flu}$	$\alpha = \sqrt{\frac{R_m}{N}}$
200	0.2	$5 \cdot 10^6$	0.125	$0.1 < N < N_c$	$0.65 < \alpha < 1.12$
1000	1	$1 \cdot 10^6$	0.125	$0.1 < N < N_c$	$0.65 < \alpha < 1.12$
10000	10	$1 \cdot 10^5$	0.125	$0.1 < N < N_c$	$0.65 < \alpha < 1.12$

The results of the study are summarized in Table 3.23.

Table 3.23: Test results

Re	V_{flu} [m/s]	N	B [T]		S_t		α	Vortices
			$V = 0$	$V > 0$	$B = 0$ $V > 0$	$B > 0$ $V > 0$		
200	0.2	0.1	0.023440293	0.023428557	0.185	0.172	1.118	yes
		0.15	0.028672224	0.028660542		0.1666	0.913	yes
		0.2	0.033135688	0.033125095		0.1666	0.790	yes
		0.3	0.041477313	0.041379738		0.1666	0.645	yes
		0.4	0.047169398	0.047105392			0.559	no
$0.3 < N_c < 0.4$								
1000	1	0.1	0.117241262	0.117184916	0.2	0.2	1.118	yes
		0.2	0.165529624	0.165489106		0.1666	0.790	yes
		0.25	0.185088324	0.185062001		0.1686	0.707	yes
		0.3	0.203066495	0.202818591		0.1686	0.645	yes
		0.4	0.236635360	0.236216058			0.559	no
$0.3 < N_c < 0.4$								
10000	10	0.1	1.170561061	1.169921372	0.2	0.2	1.118	yes
		0.2	1.653315915	1.652889438		0.1666	0.790	yes
		0.25	1.850559568	1.850307992		0.1666	0.707	yes
		0.4	2.350325799	2.346896920		0.1666	0.559	yes
		0.45	2.497607263	2.494176100			0.527	no
$0.4 < N_c < 0.45$								

The results show that, when the magnetic permeability of the fluid is greater than that one of the cylinder, the critical value of the interaction parameter is reached for smaller values than in the case

of fluid and cylinder with the same magnetic permeability. In fact, for each value of the interaction parameter N and for each value of the considered Reynolds number, the post-interaction magnetic field value is always greater than the corresponding value in the case the two materials have the same magnetic permeability. In this case, the Strouhal number seems to decrease when B increase.

The plots in Fig. 3.47, referred to case $Re = 10000$, shows that the coefficient C_d decreases, when the magnetic field increases.

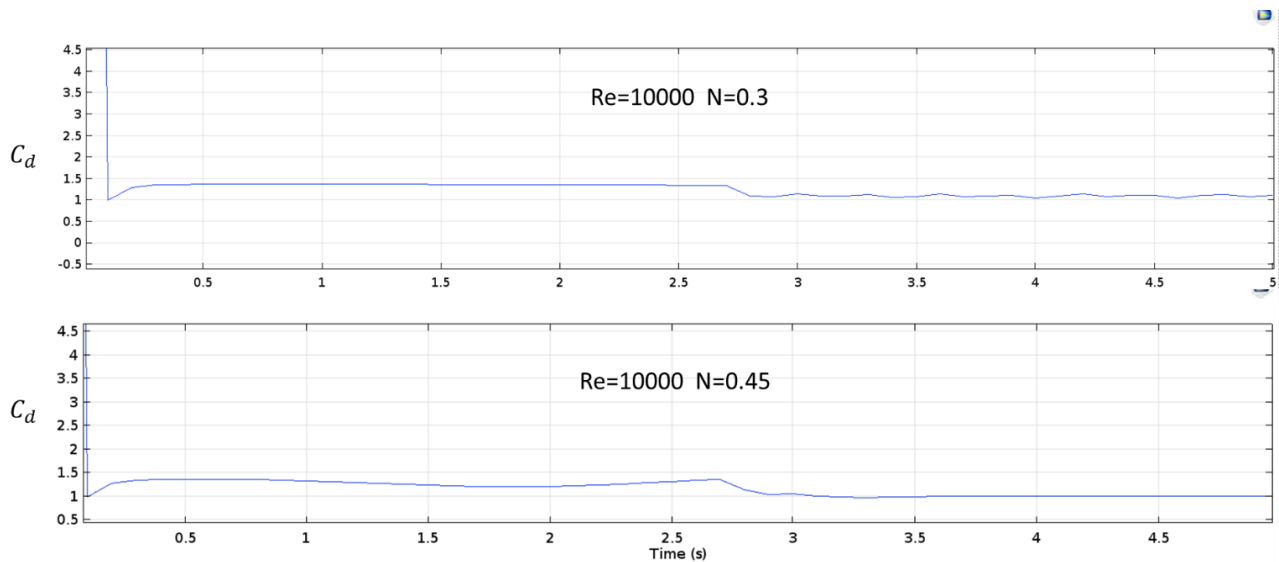


Figure 3.47: C_d coefficient for different values of N when $Re = 10000$

For the evolution of drag coefficient versus the interaction parameter, similar results to the previous case have been obtained; fixed Re , the C_d coefficient decreases when the interaction parameter N increases (Fig. 3.48).

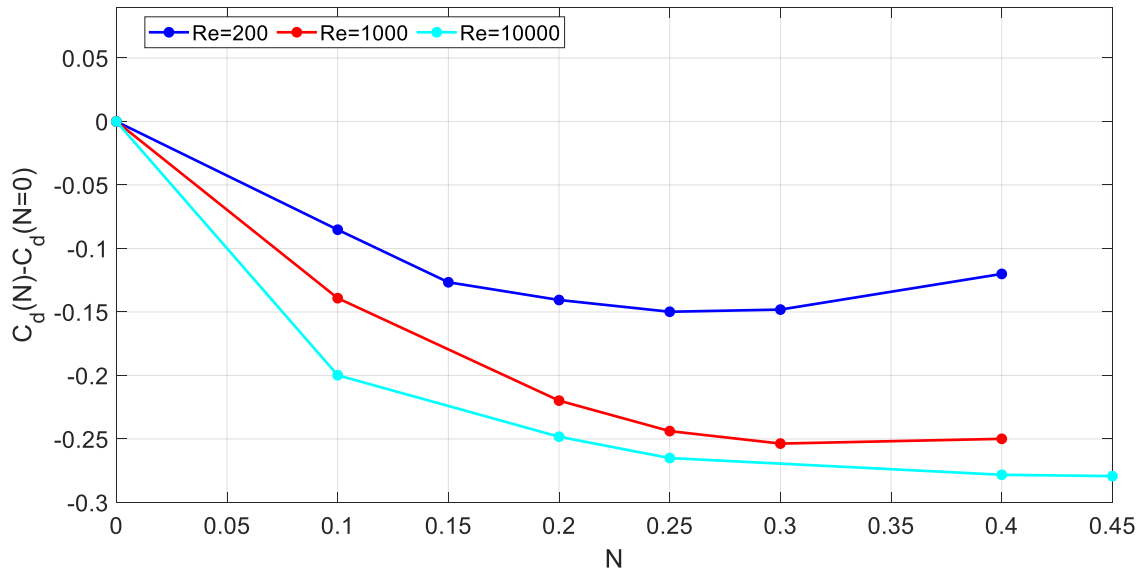


Figure 3.48: Evolution of the drag coefficient versus the interaction parameter

The configuration of the cavity in case $Re = 1000$ and $N = 0.4$ is shown in Fig. 3. 49.

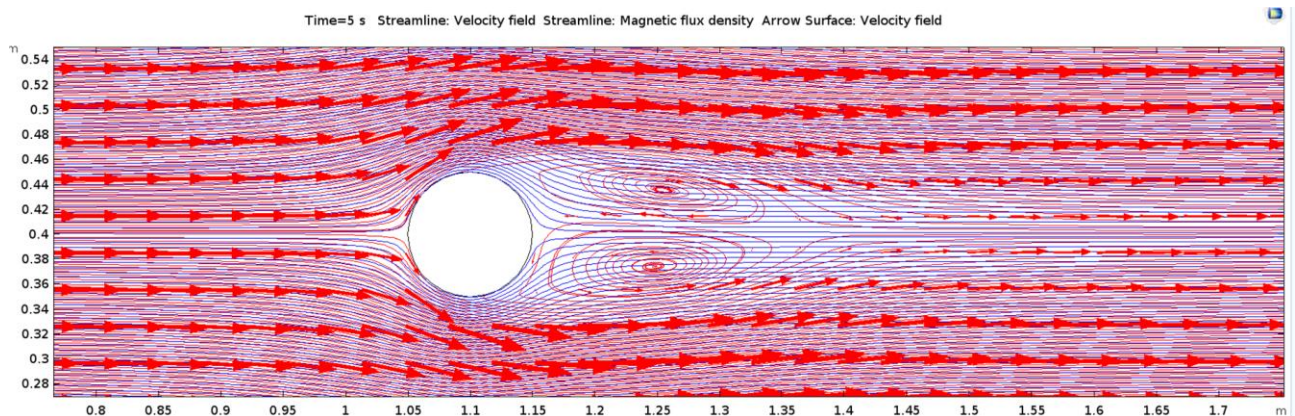


Figure 3.49: Streamline of velocity and magnetic field inside and outside the cavity for $N = 0.4$.

3.6 Results for high Magnetic Reynolds number

3.6.1 $R_m = 12.5$ and $M = 1$

In this paragraph, the previous analysis is performed for a high value of the Magnetic Reynolds number. In Table 3.24 the main parameters of the study are reported.

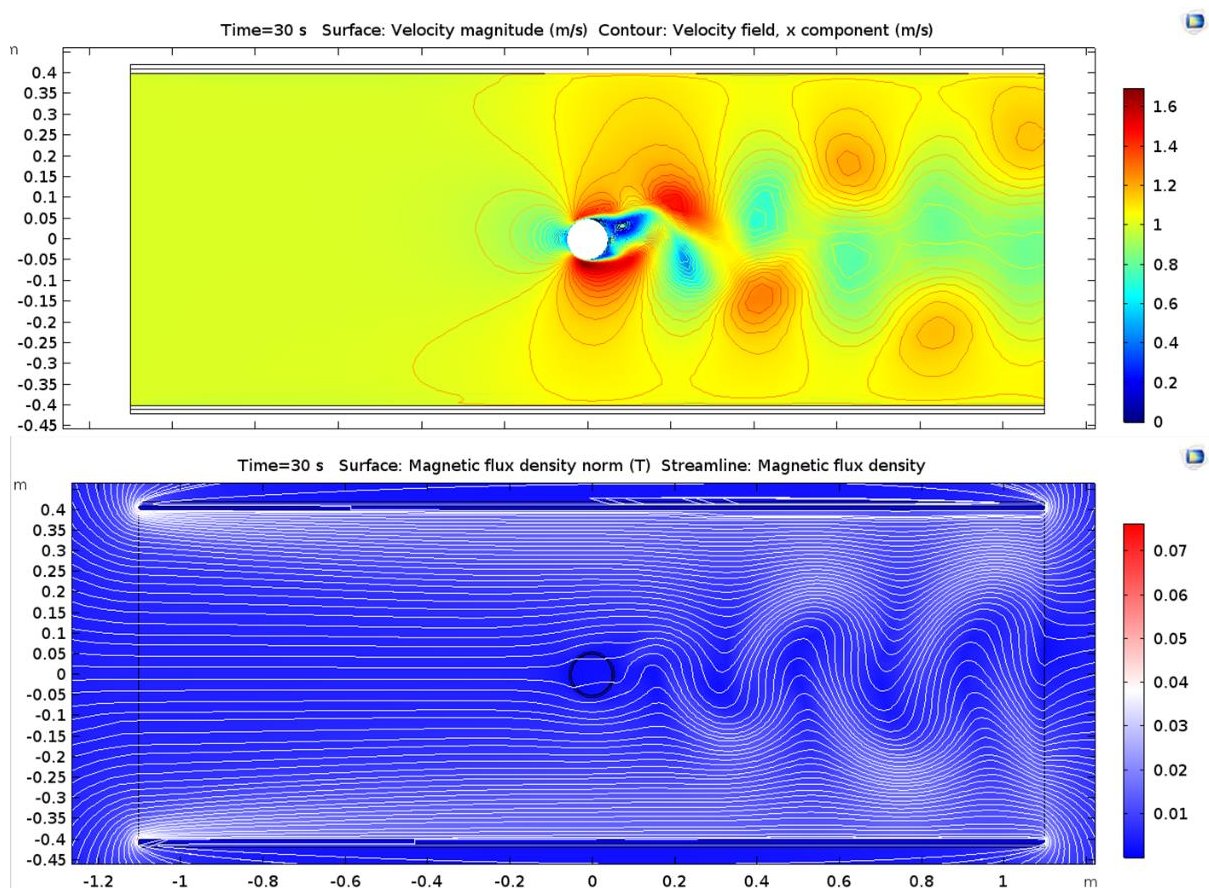
Table 3.24: Main parameters of the test.

$Re = D\rho V_{flu} / \mu_d$	$V_{flu}[\text{m/s}]$	$\sigma_{flu}[\text{S/m}]$	$R_m = DV_{flu}\sigma_{flu}\mu_{flu}$	$N = \sigma B^2 D / \rho V_{flu}$	$\alpha = \sqrt{\frac{R_m}{N}}$
1000	1	10^8	12.5	$0.1 < N < 20$	$5 < \alpha < 11.2$

The magnetic permeability of the fluid is assumed equal to that of the cylinder: $\mu_{flu} = \mu_{cyl} = 1$, but in this case the conductivity of the fluid has been increased up to 10^8 [S/m]. The value of the magnetic Reynolds number becomes:

$$R_m = DV_{flu}\sigma_{flu}\mu_{flu} = 12.5$$

Fig. 3.50 and 3.51 show that, in the range of $0.1 < N < 1$, the quasi frozen condition are reached: the magnetic induction is driven by the flow.

**Figure 3.50:** Streamlines of velocity and magnetic field when $N = 0.1$.

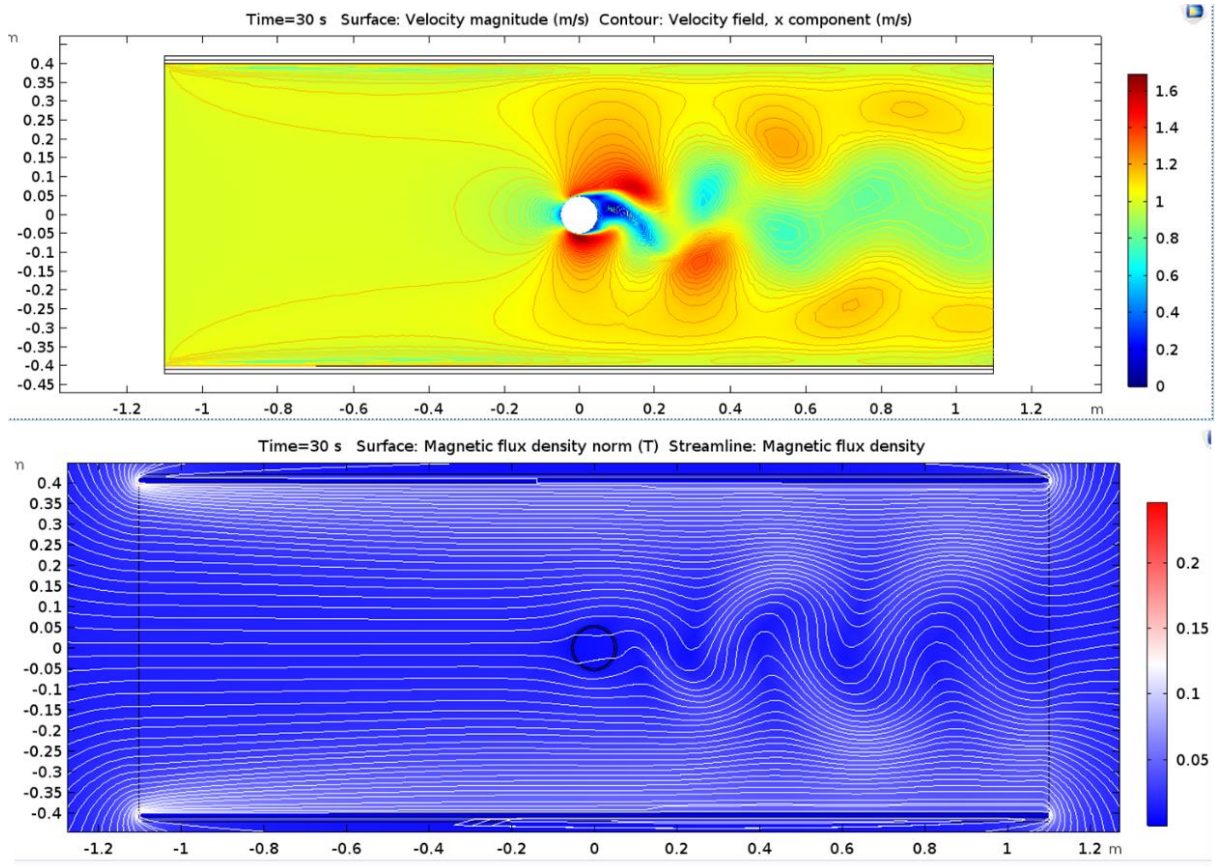


Figure 3.51: Streamlines of velocity and magnetic field when $N = 1$.

Let refer to the case in which the MHD system has the same Reynolds number: $R_e = 1000$ but $R_m = 0.125$. In this case (see paragraph 3.5.1 first case: $M = \mu_{r_{cyl}}/\mu_{r_{flu}} = 1$ $R_e = 1000$), the conductivity of the fluid is $\sigma_{flu} = 10^6 \left[\frac{S}{m} \right]$ and from the critical value of $N_c = 0.3$ the vortices disappear. The different behavior of the MHD system for high R_m is shown below. It can be observed that the Von Karman's wake is maintained for higher values of N compared to the case of small R_m . Being the magnetic field carried by the flow, when hydrodynamic vortices are present, magnetic vortices are also present.

Due to the fact that the magnetic field is transported by the fluid, the magnetic stream lines tend to the hydrodynamics stream lines, so the interaction between velocity and magnetic field, $J = \sigma \vec{V} \wedge \vec{B}$, is lower as well as the electromagnetic forces, compared to the case with small R_m . Consequently, the suppression of the von Karmann street appears for higher values of N .

In Fig. 3.52 it is shown that while outside the cylinder the magnetic field lines follow the velocity field lines (frozen conditions), inside the cylinder they tend to be deflected outside.

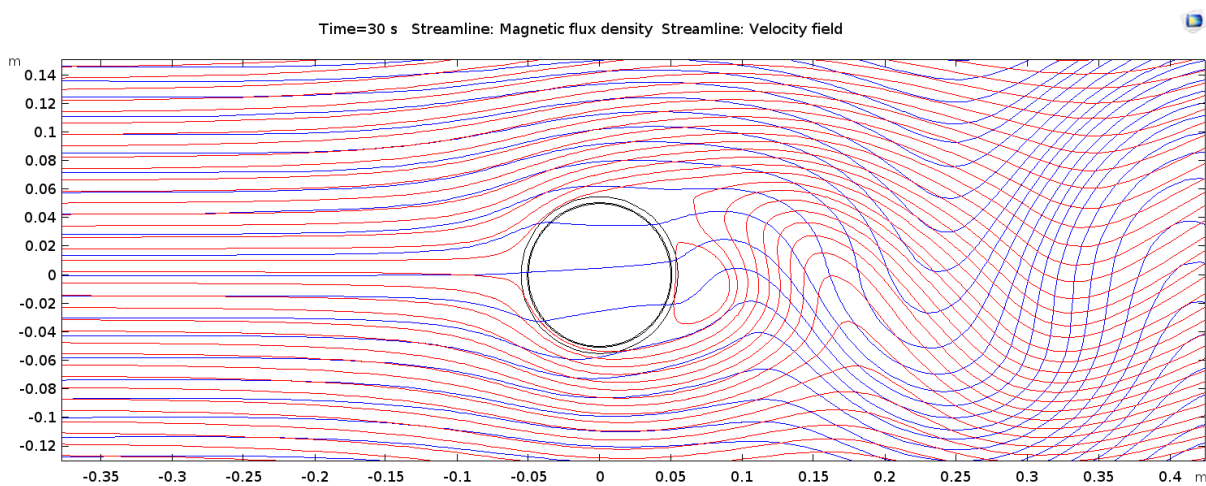


Figure 3.52: Magnetic field streamlines (red) and velocity field streamlines (blu) for $N = 1$.

In case $R_m = 12.5$, when N ranges in the interval: $0.1 < N < 1$, the frequency of detachment of vortices does not change with respect to the analyzed reference case, and the Strouhal number remains equal to 0.2. The Von Karmann street is not present for $N = 3$, which is out of the ranges analysed in this study, then only a few general comments are reported here.

Fig. 3.53 shows the development, in a given time, of the magnetic and the velocity fields for $N = 3$. The magnetic field remains almost aligned with the velocity field, but the Von Karman's street disappeared.

In the zone behind the cylinder the velocity field takes the form of a cavity where the fluid velocity is very low. The external fluid drags the internal fluid to the periphery of the cavity, and this is the reason why in this part the velocity has the highest value in the cavity. To ensure the continuity of the flow rate, a flow is generated inside the cavity in the form of two symmetrical vortices with respect to the axis of the flow. The global hydrodynamic configuration inside the cavity takes the form of two symmetrical vortices. The same type of configuration persists as long as a cavity is formed behind the cylinder.

The same behavior has been also observed for $N = 5$.

In case $N = 10$ (see Fig. 3.54) the cavity is reduced in size compared to the case $N = 3$ and $N = 5$ and the vortices are flattened in the limit zone.

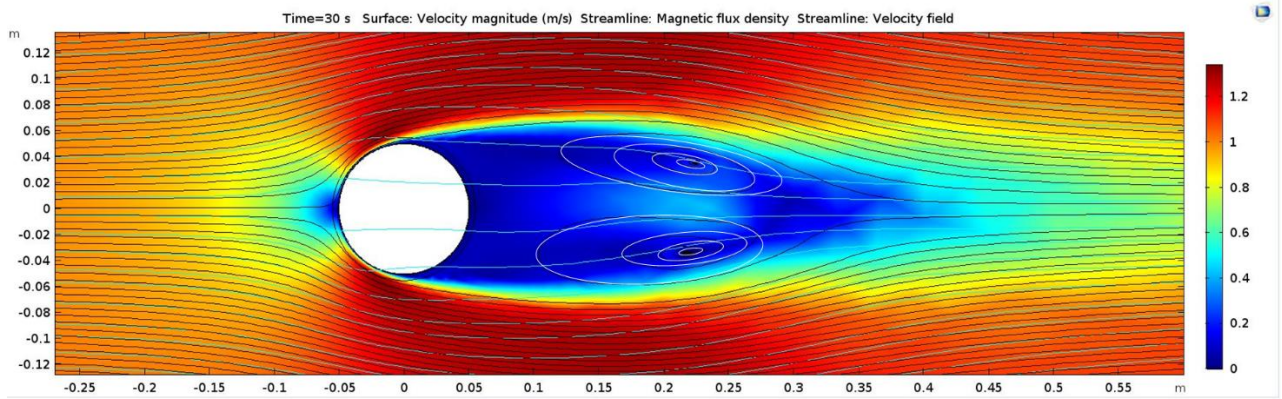


Figure 3.53: Magnetic field streamlines and velocity field streamlines in case $N = 5$.

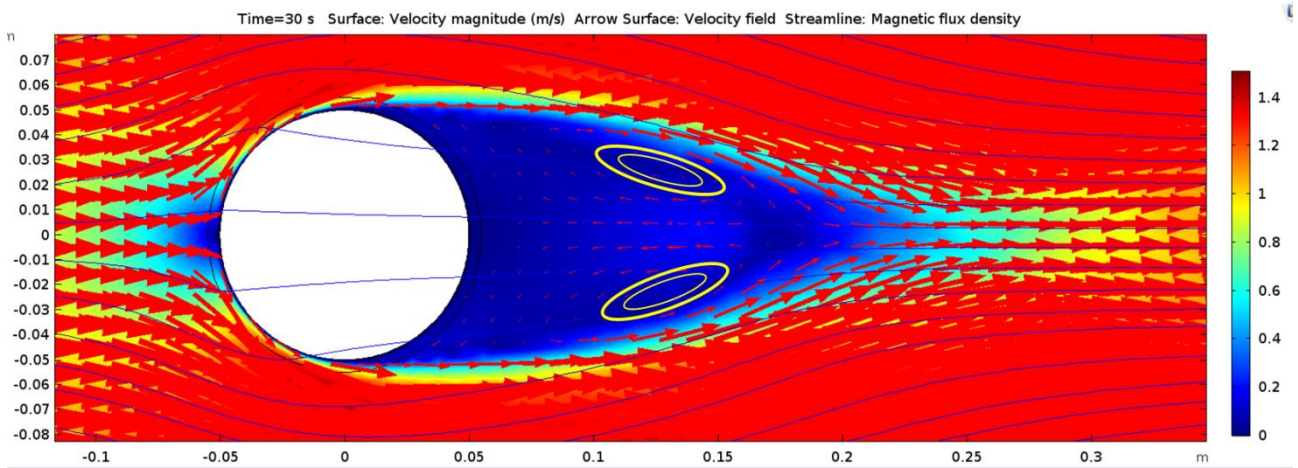


Figure 3.54: Magnetic field streamlines and velocity field streamlines in case $N = 10$.

By further increasing the interaction parameter up to $N = 20$ the cavity disappears, due to the fact that for high values of the magnetic Reynolds number the fluid drives the magnetic field, and both completely surround the cylinder without forming any cavity (see Fig. 3.55).

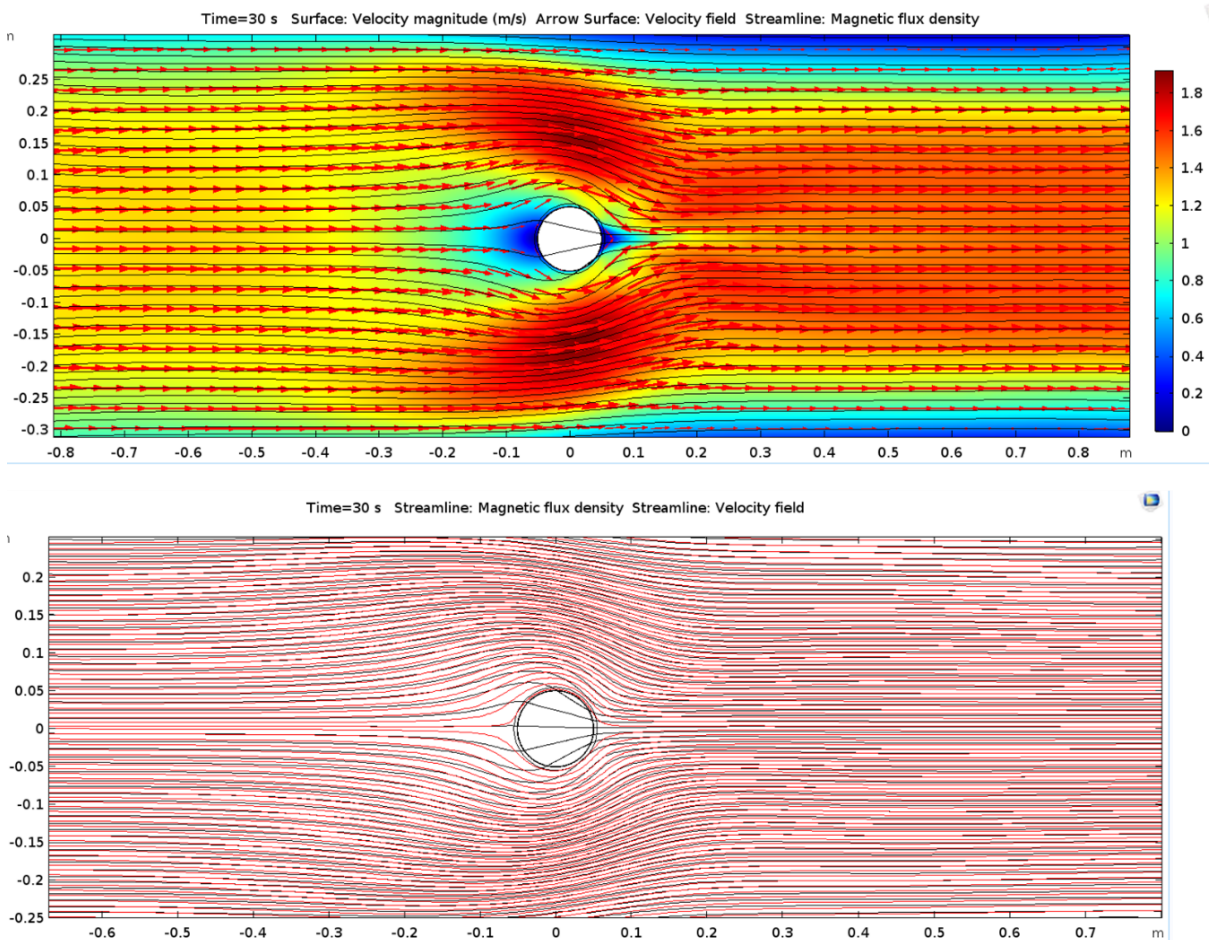


Figure 3.55: Magnetic field streamlines and velocity field streamlines in case $N = 20$.

It can be observed that the flow configuration is similar to that one observed when no magnetic field is applied and the fluid dynamic Reynolds number is low. It can be seen that the vorticity causes a reduction of the velocity upstream and an increase downstream the cylinder, and then the distance among the stream lines is greater upstream than downstream.

To summarize, when R_m is high the magnetic field is driven by the flow and tends to be parallel to it. As a consequence, for a given interaction parameter the interaction between the fluid and the magnetic field is less strong and the Von Karmann street is maintained for higher values of N in comparison to the case of small R_m .

3.6.1.1 Evolution of drag coefficient

For sake of completeness, the trend of the coefficient C_d for two cases $N = 0.1$ and $N = 1$ are reported (Fig. 3.56).

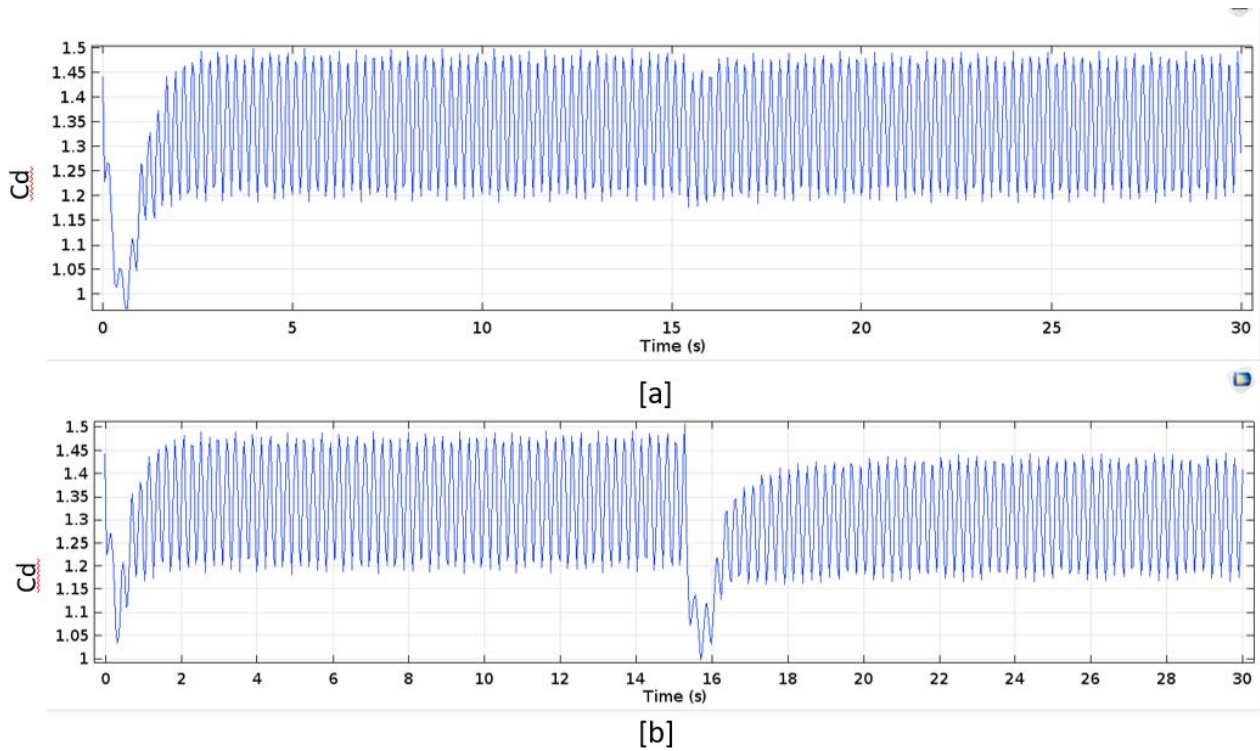


Figure 3.56: C_d coefficient in case $Re = 1000$ and $N = 0.1$ [a] and $N = 1$ [b].

In Fig. 3.57 the C_d evolution versus the interaction parameter N , with $0.1 < N < 1$, in case $R_m = 0.125$ and $R_m = 12.5$ is shown. It can be observed that in case $R_m = 12.5$ the trend of C_d is almost linear and decreasing.

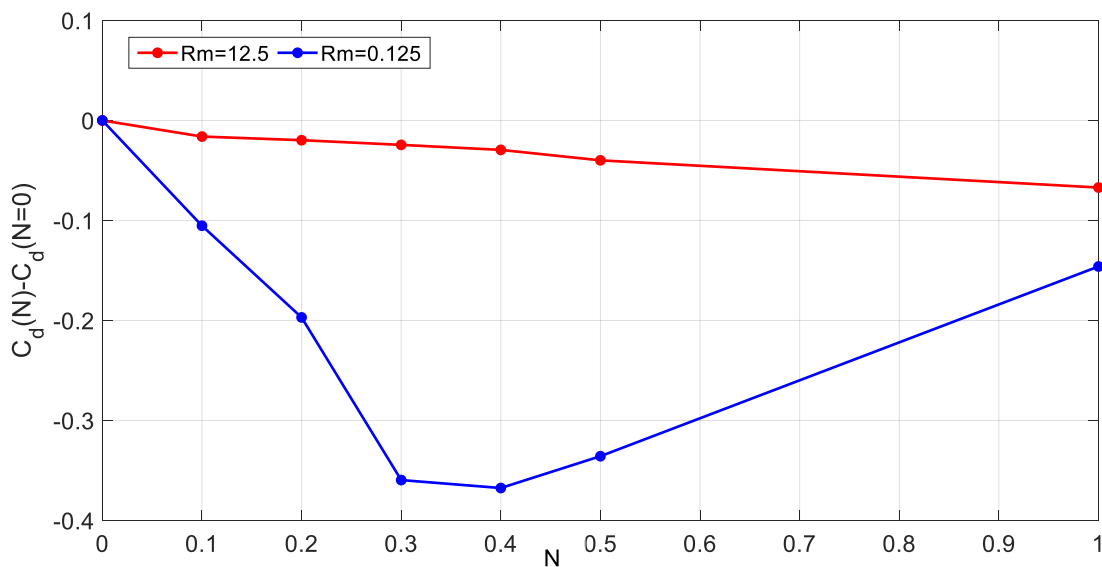


Figure 3.57: C_d evolution versus N with $0 < N < 1$, for $R_m = 0.125$ and $R_m = 12.5$

If the values of N still increase we can observe, like in case $R_m = 0.125$, a minimum value from which the C_d starts to rise. The global evolution of C_d for different values of $N \leq 20$ for the two values of R_m is shown in Fig. 3.58.

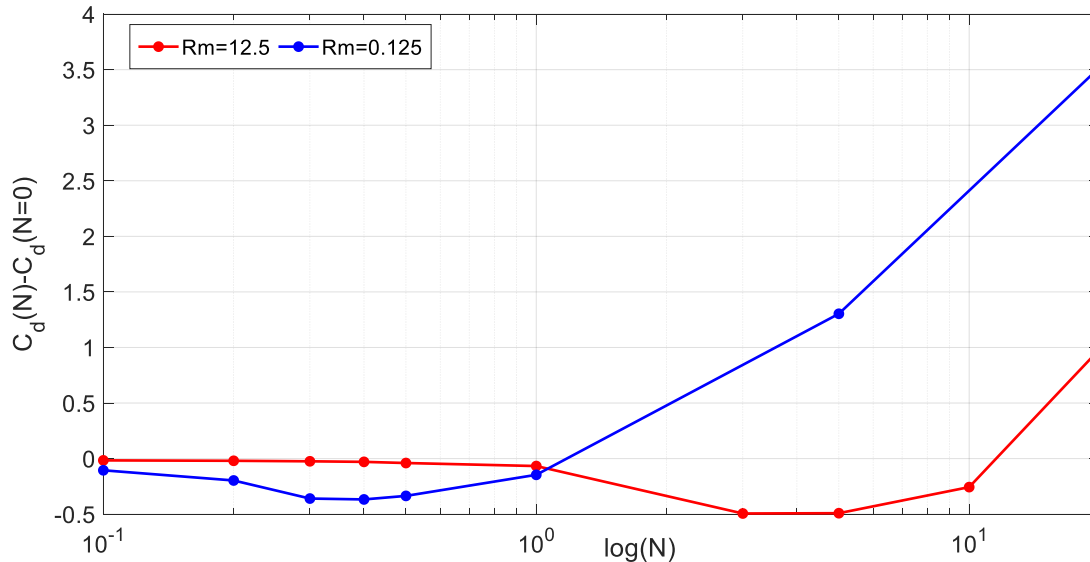


Figure 3.58: C_d evolution versus N with $0 < N < 20$, for $R_m = 0.125$ and $R_m = 12.5$.

As shown in Fig. 3.58, the evolution of the drag coefficient C_d versus N in case $R_m = 0.125$ is similar to in case $R_m = 12.5$ but this last is translated towards greater values of N .

As previously noted, for high values of R_m the magnetic field tends to follow the flow; as a result, the velocity and the magnetic fields are almost parallel so their interaction becomes weaker compared to the case of small values of R_m .

This means that, in order to have the same results of small R_m , much higher values of magnetic field \mathbf{B} , and therefore of the interaction parameter N , are required.

Further consequence is that the drag for a given value of N , is less important for high R_m compared with the small R_m .

3.7 Conclusion

In this part of the thesis, the paradigm of conducting flow, submitted to the influence of a magnetic field, which invests a cylindrical obstacle has been analysed by means of the Finite Elements Method. Firstly, the Hydrodynamics of the setup without applied magnetic field is evaluated, to validate the numerical model. In fact, all the phenomena described in the literature, like the Von Karman street, the slowing flow upstream the obstacle and the acceleration on the side of the obstacle, have been confirmed by the simulation. Alter this, a number of analyses have been performed with different values of the non-dimensional parameters, mainly the Reynolds numbers and the interaction parameters. It has been demonstrated that a magnetic field parallel to the direction of the undisturbed flow is able to dampen the eddies up to suppress them completely, when the interaction parameter is sufficiently high. It has been demonstrated, also, that the value of the interaction parameter for which the eddies collapse depends on the setup parameters, such as the containment of the flow and the relative permeability of the fluid with respect to the obstacle. The dragging force that the flow applies to the obstacle has been evaluated for the different operative conditions. As expected, the dragging force, or equivalently the resistance of a cylindrical object traveling in a fluid mean, is strongly related to the dynamics of the eddies, and then the applied magnetic field can be used to reduce the drag coefficient.

The dragging force applied to the cylinder decreases for small values of N , lower than the critical value corresponding to the disappearance of the von Karmann street, after that the drag coefficient increases continuously when N increases.

The different behavior of the system for small and high values of the magnetic Reynolds number has been analyzed. An overall difference between small and high values of the magnetic Reynolds number can be summarized as follow: for small R_m , the flow tends to follow the magnetic lines and on the contrary when R_m is high, the flow drives the magnetic field.

The interaction between the magnetic field and the flow, for the same N , is stronger when R_m is low than in the case where R_m is high. Consequently, the C_d coefficient is also less important in the latter case.

4 Magneto Plasma Sail

4.1 Introduction

In this Chapter the results of the Part I are exploited for the analysis of some specific problems related to the Magnetic Plasma Sails, an aerospace propulsion system which exploits the energy of the solar wind. This is formed by electrons and protons traveling at very high velocity (500 km/s at 1 [AU] from the Sun) and very low density ($7 \div 8$ electrons/protons per cubic centimeter), therefore to exploit its thrust, a very large sail is necessary (tens of km of the main dimension). A sail with a big mass reduces the acceleration and it is troublesome to handle in the Space, therefore the Magnetic Plasma Sails have been ideated, with the aim to realize a propulsion system with a small mass. The idea is to create a magnetized plasma flow surrounding the space vehicle, which generates a magnetosphere in the same manner of the Earth. This magnetosphere is able to deflect the charged particles of the solar wind, obtaining from this a thrust by reaction. The main issue of this technology is the generation of the cloud of plasma that generates the magnetosphere. A solid coil integral with the vehicle supplied by a current, generates a magnetic field distribution. From the center of the coil, a plasma is ejected, whose velocity allows to reach a high value of the interaction parameter N . In its turn, as demonstrated in the Part I, the value of N which produces the desired effects strongly depends on the magnetic Reynolds number. This aspect represents an advantage in this application, because the plasma is an acollisional gas, whose conductivity is extremely high, and finally the magnetic Reynolds number is very high. In these conditions, the plasma trajectories are deviated, assuming a toroidal component. If the interaction is enough strong, the particles of the plasma are captured by the magnetosphere of the coil, giving rise to an enlarged coil of current, but the added current circulates without any solid support. The plasma, in its turn, enlarges the magnetosphere, making it possible to capture new plasma ejected by the vehicle. Theoretically, this process of “inflation” could continue as long as the value of the interaction parameter is guaranteed in the periphery of the cloud of plasma. In this way, it is possible to obtain extremely large sails, with a very limited solid support. This technology has not yet been tested, as a number of open issues have to be solved before. The complete analysis of this system is far beyond the scope of this thesis, but some of the aspects treated in the previous sections find a direct application in this technology. These aspects are the subject of this Part.

In particular, the conditions for the plasma deviation in order to inflate the sail are assessed, and the calculations of the thrust exerted by the wind on the spacecraft are determined. Starting from the

existing literature [19] [20], in this work a Finite Element model has been developed, which simulates the magnetic sail inflation process, its interaction with the solar wind and the obtained thrust. By exploiting the nondimensional analysis, the same model can represent both an experimental setup and a real-scale application. This approach is compulsory, due to the range of scales in the system and the extreme values of density and velocity, which make unaffordable the computational burden of a real-scaled problem.

Finally, the results on the thrust are used to estimate the possibility to perform a mining mission on the asteroids belt, valuating the time for a return journey.

4.2 State-of-the-art of solar sails

Early pioneers of solar sailing include Konstantin Tsiolkovsky [21] and Friedrich Tsander [22], who realized it is possible to attain cosmic velocities using the pressure of solar radiation. A photonic solar sail (or sailcraft) is considered to be a spacecraft that is propelled mainly or exclusively by solar radiation, then a typical solar sail would utilize thin sheet(s) of reflective membrane material to harness sun's radiation for propulsion purposes.

4.2.1 *Solar wind*

The sun emits energy mainly in the form of electromagnetic radiation and, in a small part, also in the form of solar wind (see Fig. 4.1). The solar wind is a hydrogen plasma flux, which propagates in interstellar space. Near the Earth, the solar wind velocity varies between 300 to 500 km/s. It is supersonic, then produces bow shocks (this occurs when the magnetic field of an astrophysical object interacts with the nearby flowing ambient plasma) encountering obstacles. The solar wind is highly conductive, so that it is strongly coupled with magnetic field and tends to transport outward the sun magnetic field toward the interstellar space.

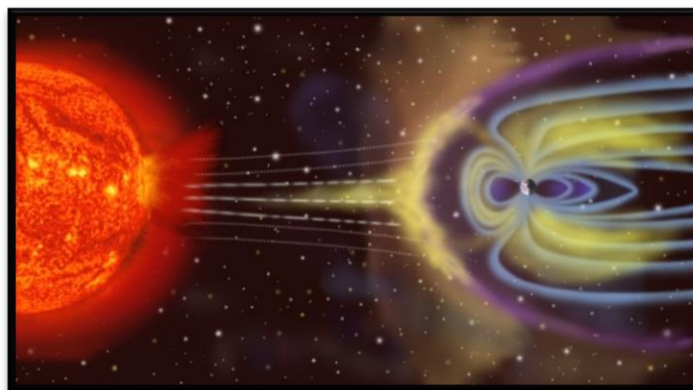


Figure 4.1: Solar wind

In Table 4.1 the properties of the solar wind flow are reported, as the velocity, the temperature, and the density, that can be exploited by the solar sail to obtain a thrust.

Table 4.1: Properties of solar wind

Properties of the solar wind flow observed at 1 AU	
Proton density	$7 \div 8 \text{ cm}^{-3}$
Electron density	$7 \div 8 \text{ cm}^{-3}$
H_e^{2+} density	0.3 cm^{-3}
Velocity	450 Km/s
Proton temperature	$1.2 \times 10^5 \text{ K}$
Electron temperature	$1.4 \times 10^5 \text{ K}$
Magnetic induction	7 nT

4.2.2 *Types of solar sails*

Different kind of solar sail have been developed.

The first one is the **Photon Sail** (Fig. 4.2) that exploits the radiation pressure exerted by sunlight on large mirrors for spacecraft propulsion. Ideally, if the incident photons were all reflected and if there was no attenuation, the thrust F would be directly proportional to the square of the cosine of the angle θ between the sail normal and the incident radiation, and inversely proportional to the square of the distance r from the sun:

$$F = F_0 \frac{\cos^2 \theta}{r^2} [N]$$

In the reality, the sail performance is affected by the accuracy of its surface, by its reflectivity, its mass per unit area and other factors a lesser extent. For example, with a 100 m^2 sail, made of aluminum on polymer background (500 kg), a thrust of 50 mN can be obtained. The thrust, however small, will persist until the sail is illuminated. This system is very attractive because it does not require on-board energy sources; however it presents deployment difficulties, high weight and fragility.

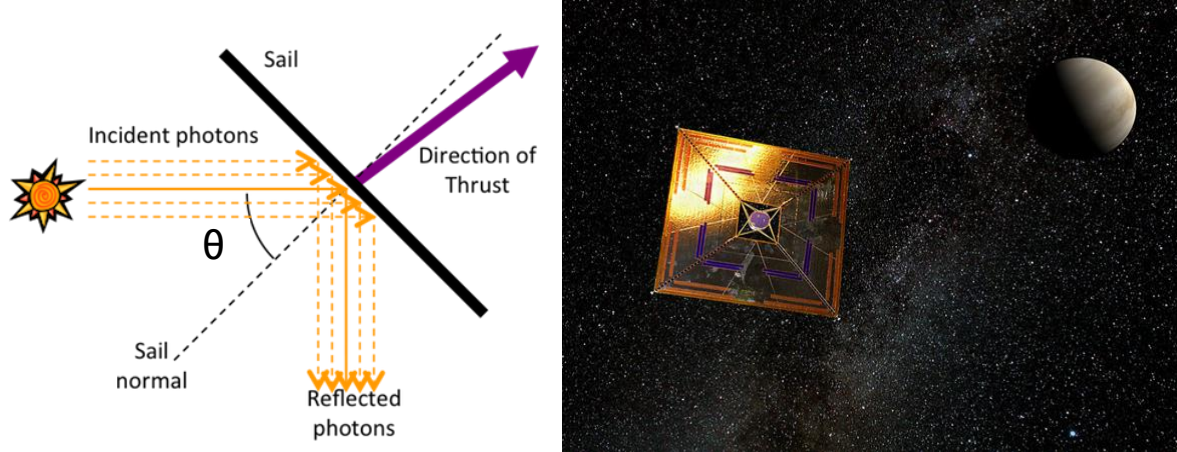


Figure 4.2: Photon Sail.

The second one is the **electric sail (E-sail)** (Fig. 4.3), a propulsion invention made in 2006 at the Finnish Meteorological Institute by Pekka Janhunen [23] [24]. It creates a "virtual" sail by using small wires (tethers) to form an electric field that deflects solar wind protons and extracts their momentum. E-sail tethers need to be lightweight, conductive, resistant to micrometeoroid impacts, and able to withstand the tension and pull created by the centrifugal acceleration. The number and lengths of the tethers can vary. Their diameter is restricted by the need to limit surface area in order do not generate excessive thermal electron current. Such current would need to be cast off by the electron gun, the use of which decreases the global performance by due to its energy consumption.

Typical tethers (about 50-100) are long 20 km and thin 25 microns. The spacecraft contains a solar-powered electron gun that emits a typical power of few hundred watts, which is used to keep the spacecraft and the wires in a high (typically 20 kV) positive potential. The electric field of the tethers extends a few tens of meters into the surrounding solar wind plasma that interacts with these long obstacles. Thrust for the E-sail is produced by the interaction of charged tethers with solar wind particles: deflected by the electric potential surrounding the tethers, the particles transfer some of their momentum to the E-sail. The produced thrust of an E-sail is inversely proportional to its distance from the Sun, $F \propto (1/r)$ [25], in contrast to the traditional photonic solar sail, for which $F \propto (1/r^2)$. The reason behind this is that, with greater distance from the Sun and a corresponding attenuation of the solar wind, the effective area around the charged E-sail tethers increases.

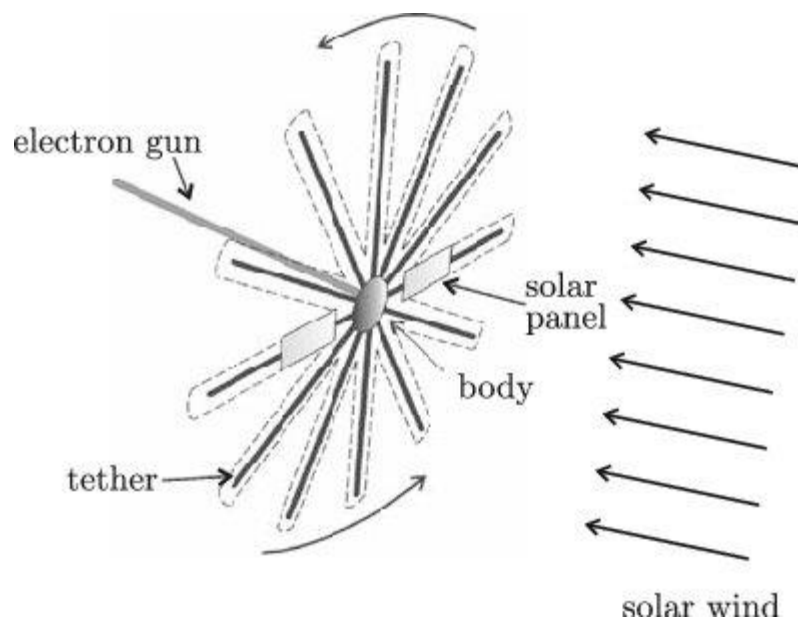


Figure 4.3: Electric Sail [26]

Another type of solar sail is the **Magnetic Solar sail (MagSail)**, a unique interplanetary propulsion system that has never been realized. The use of the solar wind in a concept of the magnetic sail as a propulsion system was first proposed and invented by Andrews and Zubrin [27]. The MagSail (Fig. 4.4) comes into being with the aim of exploiting the solar wind energy. The idea is to use an on-board magnetic field which is sufficiently intense to deflect the charges carried by the solar wind, so that, for the momentum conservation, a thrust will act on the spacecraft that is mechanically integral with the field itself. The magnetic field around an onboard superconducting coil of the spacecraft is generated by a loop of superconducting wire attached to the spacecraft. The superconducting cable, which once fed, will tend to form a ring (to have an idea, we need a 100 km diameter loop to have pressures in the order of 1 N). The ring, thanks to its superconducting properties, has to be fed only initially and, kept at the right temperature. The current, once started, will be maintained indefinitely in the superconductor without the need for additional power. The only energy is required to set the initial current and feed the cryogenic systems.

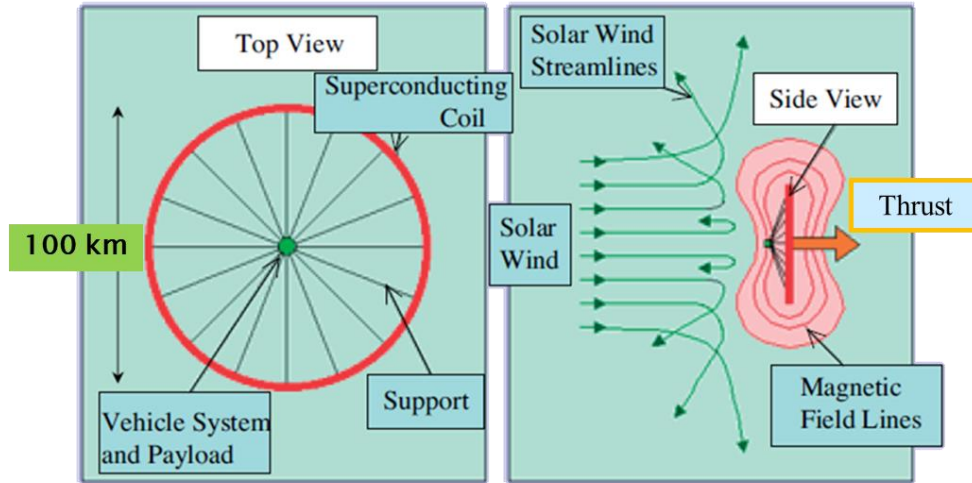


Figure 4.4: Magnetic Solar sail

In Fig. 4.5 a three-dimensional representation of the magnetic sail which appears as a kind of "magnetic bubble shows" is shown. The boundary between a solar wind plasma and a magnetosphere is called magnetospheric boundary or magnetopause, where induced currents divide the plasma and the magnetic field regions. This "bubble" then, while generating the momentum transfer, also acts as a barrier against the solar wind, as the magnetosphere does with earth planet, therefore the MagSail can be considered as a kind of mini-magnetospheric propulsion system.

The force on the coil of a MagSail is formulated as

$$F = C_d \frac{1}{2} \rho_{sw} u_{sw}^2 S [N] \quad (4.1)$$

where C_d is thrust coefficient, $\frac{1}{2} \rho_{sw} u_{sw}^2$ is the dynamic pressure of the solar wind, S is the blocking area, $\rho_{sw} = m_i n$ is the solar wind, m_i is the mass of an ion, n is the number density, and u_{sw} is the velocity of the solar wind.

To calculate F from Eq. (4.1), the blocking area S should be specified, but S is not a priori given. It is therefore customary to employ the characteristic length L that depends on the solar wind properties and on the magnetic moment of MagSail, and to approximate the blocking area as $S = \pi L^2$.

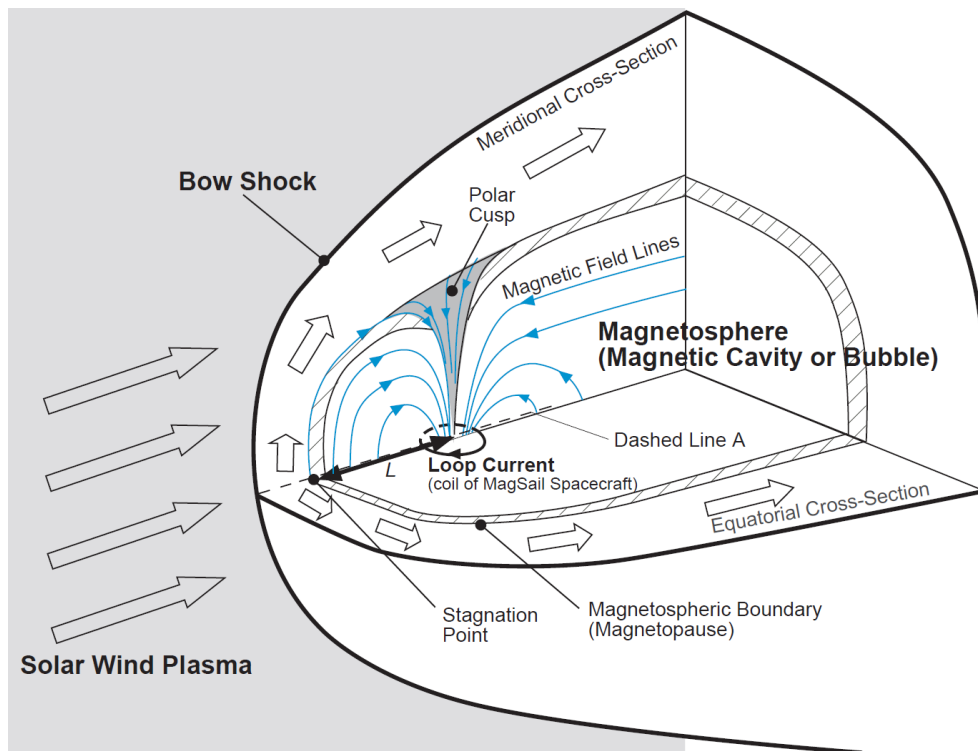


Figure 4.5. Magnetosphere of MagSail [28].

This system, compared to previous solar sails, greatly reduces deployment and fragility issues, but volume and excessive weight (about tens of tons) are its main drawbacks. With the aim to overcome the limitations of this layout of magnetic sails, it was thought to inject a plasma flow at the center of a small coil in order to strengthen the magnetic field.

In particular conditions ($Rm \gg 1$) the plasma jet is able to advect outward the magnetic field, allowing its extension away from the aircraft, at significantly greater distances than for a simple dipole field. This system is called **Mini Magnetospheric Plasma Propulsion** system (**M2P2**) or **Magneto Plasma Sail (MPS)**, and, as the Magnetic Sail, exploits a magnetic field to transfer momentum from the solar wind to the spacecraft (Fig. 4.6 **Figure 4.6**). Developed by Winglee in 2000 [29] [30] a Mini-Magnetospheric Plasma Propulsion system uses an artificially generated bubble of a magnetic field, which is inflated by the injection of high- or low-energy plasma. The magnetic bubble around and the attached spacecraft will be carried by the solar wind.

The spacecraft will be pushed into the wind direction with a very low energy demand due to the coil fed and the plasma generation: a 0.25 – 1.0 kg/day of plasma permits to generate a magnetic cross section of 15-30 km, 1-2 kW of power and a velocity of 3-4 km/s.

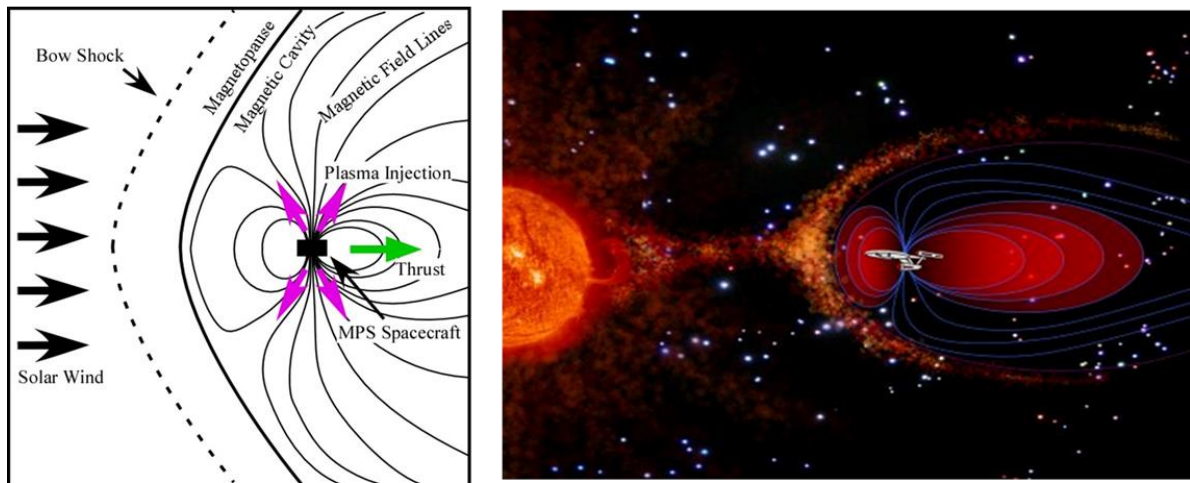


Figure 4.6: Magneto Plasma Sail M2P2

The M2P2 system has manifold of strengths. First of all, it uses electromagnetic processes to produce an obstacle to the solar wind, therefore removing many of the technical issues related to other solar sails. Secondly, it is able to ensure a large interaction cross-section with the solar wind, with limited weight and power. Finally, unlike the other layouts of solar sails that oppose a constant interface to the solar radiation, thus providing a variable thrust which decreases with the squared of the distance from the sun, the MPS system acts like a balloon and expands while the wind pressure decreases, ensuring a constant thrust and so a constant acceleration to the spacecraft as it moves away from the sun.

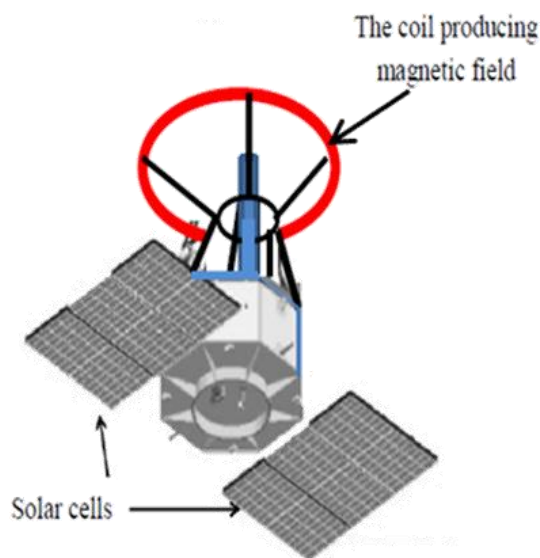


Figure 4.7: Spaceship with magnetic coil source

Despite these advantages, the TRL of this technology is still very low, because of the difficulty to perform laboratory experiments to proof the real possibility to inflate the magnetosphere and to determine the values of the obtainable thrust. In fact, it is very hard to reproduce in laboratory the very low density of the space and the velocity of the solar wind.

When the plasma flows along the field lines the dynamic plasma pressure varies until to reach the equilibrium with the magnetic pressure: $\rho \cdot V^2 = B^2/2\mu_0$; starting from these conditions, the further plasma injected can drag outwards the magnetic field (sail inflation).

The system relies on the reduction of the decay of the magnetic field with the radial distance from the source. If the magnetic field is in frozen conditions (magnetic Reynolds number $Rm \gg 1$), the injection of plasma can drag the magnetic field outwards, resulting in a decrease of the field with R^{-2} rather than with R^{-3} (as happens for a simple dipole magnetic field). The energy of the injected plasma will support this decrease in the magnetic field fall-off. In addition, the action of solar wind against the magnetic bubble determines compression and heating of the plasma, leading to the formation of current sheets, so that, finally, the magnetic field will tend to fall off as R^{-1} [30].

The relationship between solar wind pressure and magnetic pressure will be of fundamental importance in this phenomenon. In fact, being:

$$\beta = \frac{\text{Plasma dynamic pressure}}{\text{Magnetic field pressure}} = \frac{\rho v^2}{B^2/2\mu_0} = \frac{n K_B T}{B^2/2\mu_0} \quad (4.2)$$

where ρ is the plasma mass density, v is the plasma velocity, n is the plasma number density, K_B is the Boltzmann constant, T is the plasma temperature, B is the magnetic induction module and μ_0 is the vacuum magnetic permeability, when β increases the thrust increases. But also the power consumption increase contemporarily and the ratio between thrust and fuel consumption globally decreases. For this reason, it is convenient to choose as long as possible a fairly low β in the high magnetic field region inside the coil. ($\beta \approx 10^{-2}$ [30] [31], or $\beta \approx 10^{-4}$ [32] [33]).

4.3 M2P2 – Analytical Model

The phenomena and equations involved in the M2P2 system are related to the fluid mechanics, electromagnetism and plasma physics. In order to model the M2P2 system and in particular the process of inflating the magnetosphere and its interaction with the solar wind to determine the thrust exerted on the vehicle, the following hypotheses can be done:

1. The plasmas involved in the process are modelled as highly conducting fluids (but it is not identical to a plasma) where the single charged particles are not distinguishable
2. The interaction between the solar wind and the magnetic field generated by the coil reaches stationary conditions at the magnetopause

Some problems arise when one wants to model such complex systems. In fact, the difference in scale between coil and magnetosphere makes laboratory and numerical experimentation very difficult; the density, the ionization of fluid and the wind velocity are not reproducible in laboratory and make the numerical model instable. A solution consists in developing a model that considers the non-dimensional form of the involved equations simplifying both numerical modelling and laboratory experiments.

4.4 FEM model

4.4.1 *Starting FEM model*

In the present work, a transient finite element method (FEM) Multiphysics analysis has been performed in 2D to assess the magnetosphere formation process of the M2P2 system, its interaction with the solar wind and to calculate the thrust exerted by the wind on the spacecraft.

The results of this analysis provided indications on the values of the non-dimensional numbers, such as the fluid dynamic and magnetic Reynolds numbers and the interaction parameter, whose values have a range of validity, which do not depend on the domain and the parameters of the model. In the following, the main results obtained are shown.

In Fig. 4.8, the model geometry and the triangular mesh for the simulations are shown. A single coil with diameter of 20 cm made by copper representing the on-board magnetic field source, and a device for the plasma injection along the axial direction at the centre of the coil, has been positioned at the centre of the square domain with a side of 10 m. The solar wind has been simulated by a high conducting fluid flow coming from the left side of the domain.

4.4.2 *Sail inflation: conditions for deviating the plasma*

In analogy with the model examined in the first part of the present study, the simulation required successive steps of analysis. As a first step, the transient study has been run in order to analyze the formation and distribution of the magnetic field generated by the coil (Fig 4.9). This first test had a duration of $t = 500$ s to be sure that the steady state conditions have been reached.

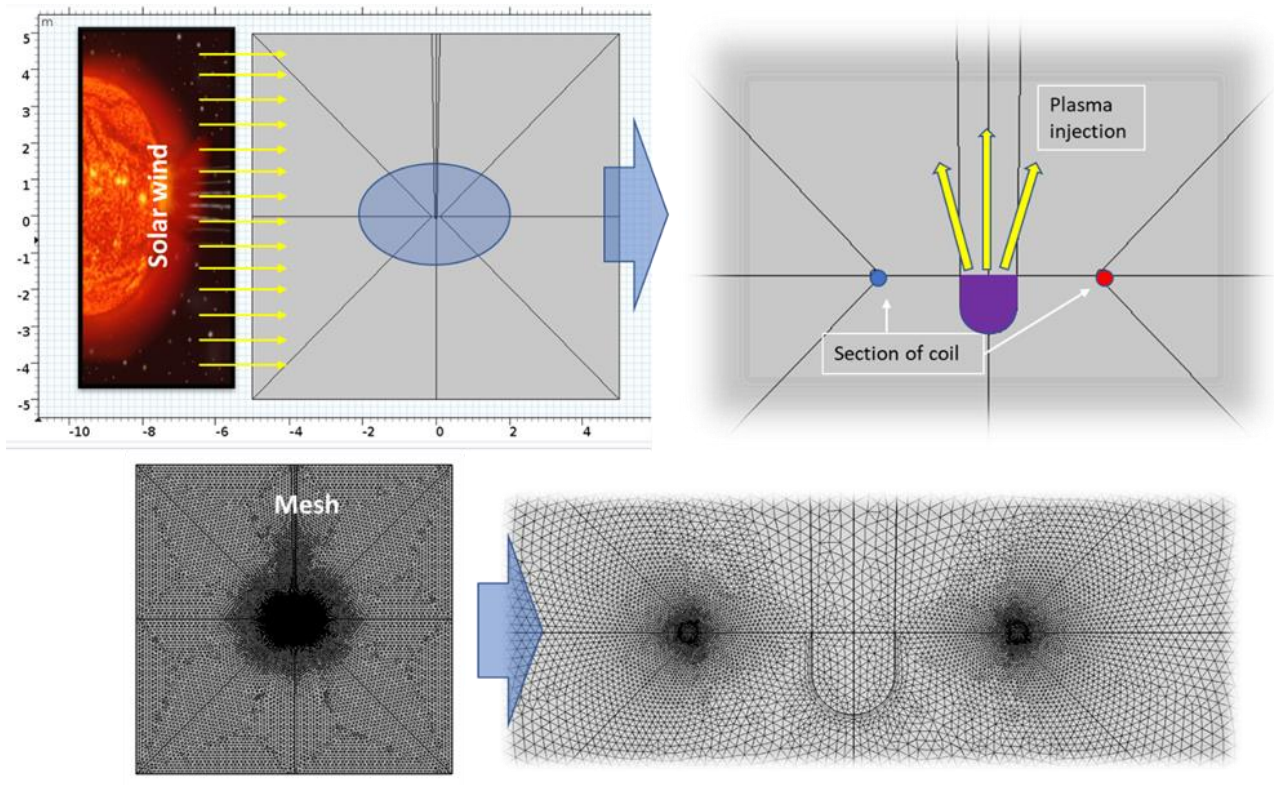


Figure 4.8: Geometrical FEM model and mesh

In a second step, the effects of the injection of plasma inside the magnetic field, in particular the behaviour of magnetosphere around the coil system, have been evaluated. The successive step regards the interaction between the solar wind and the magnetic field. Finally, the MHD interaction between magnetic field, plasma and solar wind has been studied.

Some parameters of test are shown in the Table 4.2 and 4.3.

Table 4.2: Main fluid dynamic parameters

$V_{solar\ wind}$ [m/s]	V_{plasma} [m/s]	$\sigma_{wind} = \sigma_{plasma}$ [S/m]	$\mu_{wind} = \mu_{plasma}$ [Pa*s]
1	5	$1 \cdot 10^8$	$1 \cdot 10^{-4}$

Table 4.3: Values of dimensionless parameters in the inflation of the sail

	Description	Injected plasma
R_e	Reynolds number	1250
R_m	Magnetic Reynolds number	15.7
N_{max}	Max Interaction parameter	13.3
Ha	Hartmann number	129.2

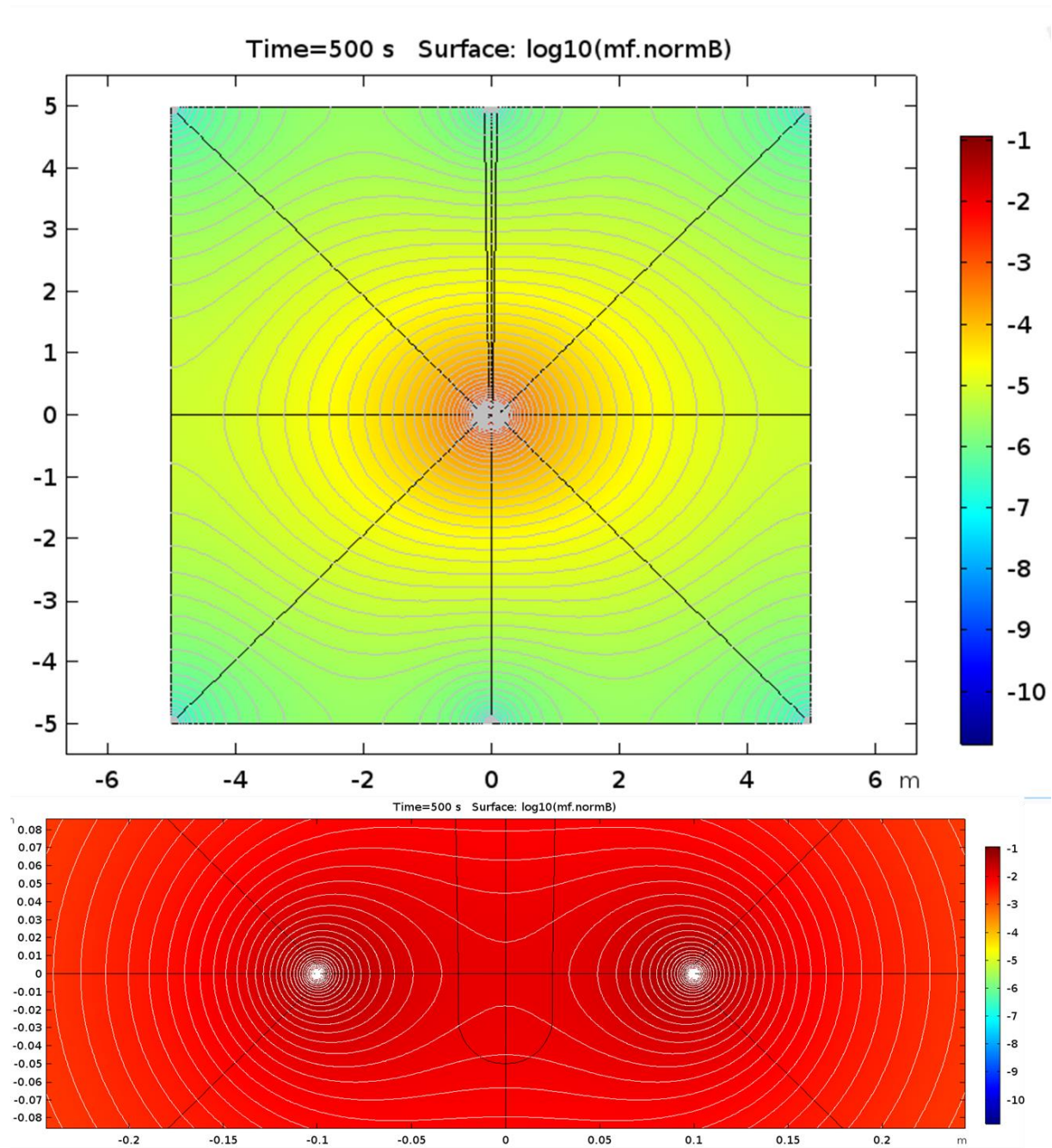


Figure 4.9: Magnetic flux density norm B (log scale)

In Fig. 4.10 the interaction between the injected of plasma flow and the magnetic field is shown. The trajectory of the plasma particles is evidently deviated by the presence of the magnetic field; these ones tend to align to the trajectory of the magnetic field streamlines, increasing the magnetosphere around the coil.

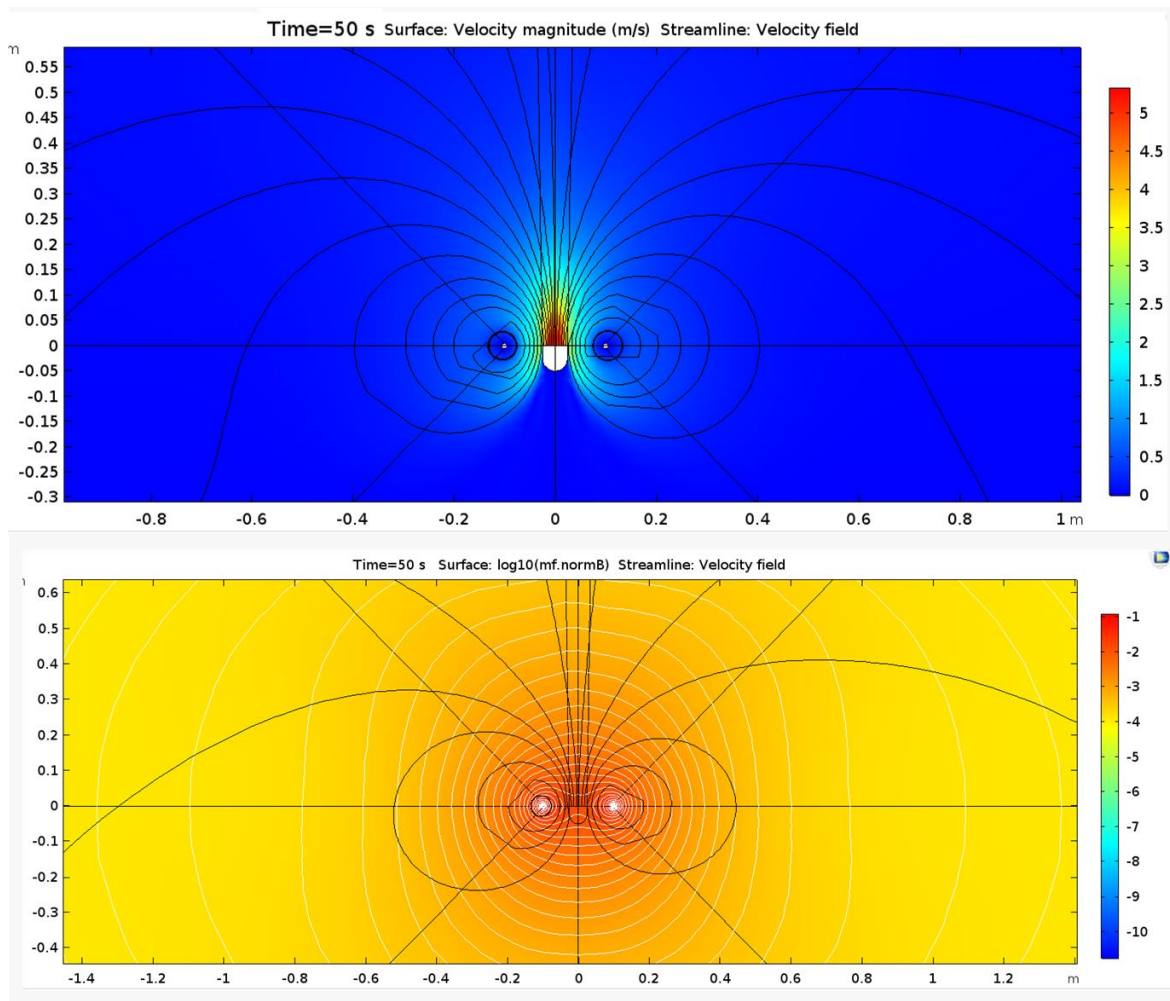


Figure 4.10: Effect of plasma injection in the presence of magnetic field.

This behavior depends, as seen in the previous study, on value of the interaction parameter N and therefore on magnetic Reynolds number R_m . For high values of the magnetic Reynolds number, the magnetic field tends to follow the flow lines. In other words, for high values of the interaction parameter N , the interaction between the magnetic field and the flow increases and these tend to dispose themselves parallel.

In Fig. 4.11 the effects of plasma injection on the magnetic field are shown. Without any injection, a simple dipole magnetic field vanishes with the cube of the distance. This rate of decadence is greater than in the void, because the coil induces a distribution of current in the mean, which act as a shield of the magnetic field. The profile changes when a plasma injection is applied in the center of the coil. It could be observed an increase of the \mathbf{B} field at the edge of the domain, which means that the magnetopause is pushed away from the coil and finally the solar sail is enlarged. Moreover, the magnetic field norm increases more in longitudinal direction than that in transverse direction to the magnetosphere.

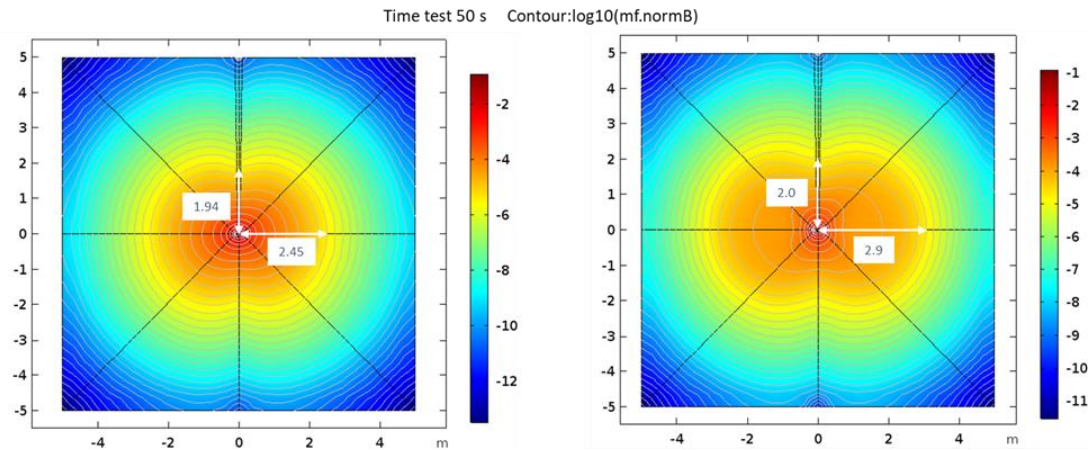


Figure 4.11: Magnetic flux density norm B (log scale); left without plasma injection; right with plasma injection.

This last aspect is also evident in Fig. 4.12 that shows the effect of plasma injection on velocity field in the presence of solar wind; it can be observed that the inflation increased the distance of the magnetopause from the solid coil, causing an enlargement of the sail.

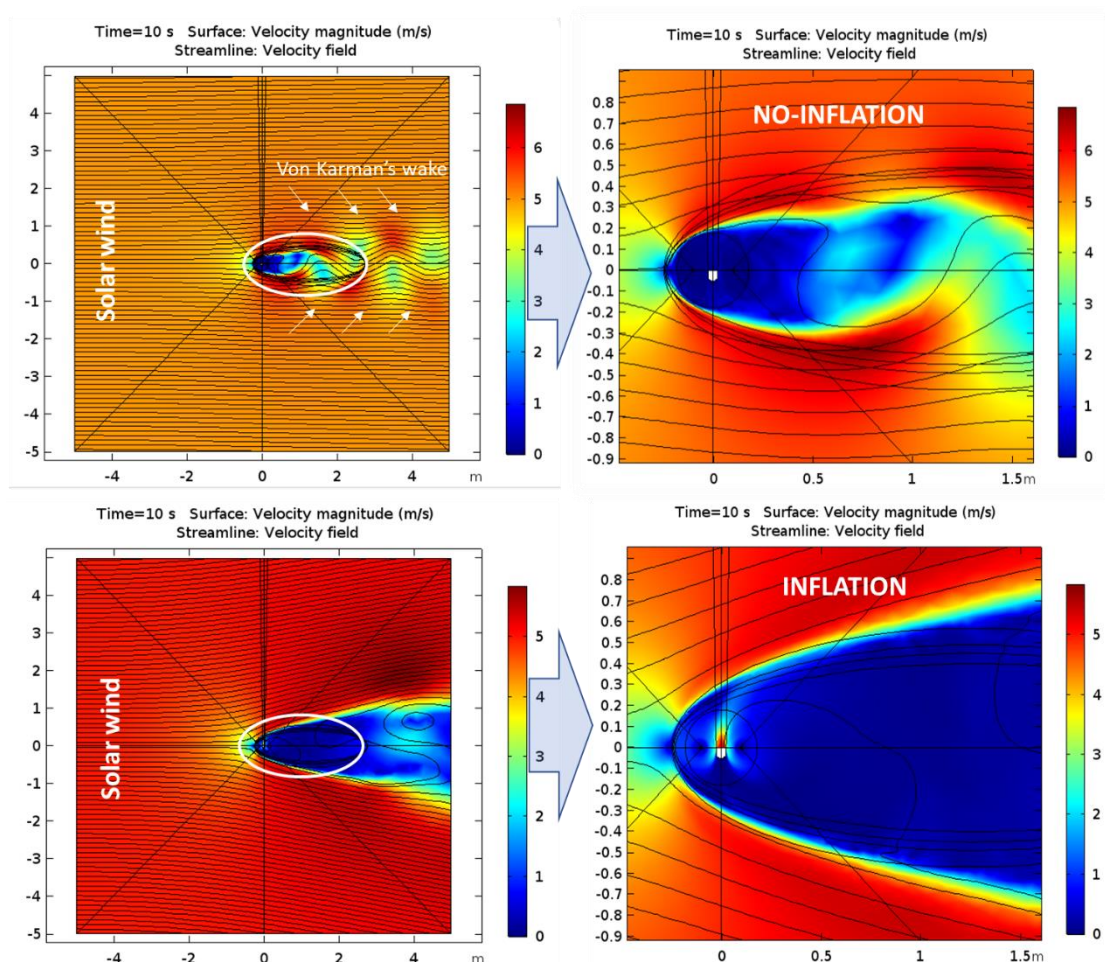


Figure 4.12: Effect of plasma injection on velocity field: with solar wind.

These results provide important insights for understanding the phenomenon of inflating of magnetic sail and the extension of the magnetic field, with the spacecraft inside, far from magnetopause.

The following remarks can be done:

- The solar sail behaves from the fluid-dynamic point of view like a squat body, which is invested by the solar wind flow.
- As in the case of the MHD system with a cylinder, studied in the Part I of this thesis, when a moving fluid meets a squat body, the Von Karman's wake is present behind the obstacle, with alternating vortices in the upper and lower region of the obstacle.
- The plasma injection, which follows the lines of the magnetic field around the coil, perturbs and increases the magnetic field, when the value of N and R_m is enough high, determining the growth of the surface of magnetopause. As a result, the wind thrust grows.
- Since the resulting thrust is proportional to the square of the transverse dimension of the solar sail (see equation (4.1)), we can estimate the increase of the thrust by the increase of the transversal dimension of the magnetosphere (see Fig. 4.12).
- The force of the solar wind is transferred to the coil with the deformation of the magnetic field in the region around the coil. This is the only way the thrust is transmitted to the vehicle, as the magnetosphere isolates it from the solar wind and therefore no gradient of pressure establishes in this region.
- As a result of interaction between the solar wind particles and the magnetosphere, the surface currents inside the magnetopause are formed; they act as a barrier to the magnetic field, which is therefore confined within the magnetosphere.

Concerning the fluid dynamic interaction between the magnetic sail and the solar wind, the value of Reynolds number is $R_e = 1 \cdot 10^4$.

These values, although far from the values of the real case, represent the starting point for the studies of a dimensionless model, in which the Reynolds number, the Magnetic Reynolds number and also the Interaction Parameter may vary independently on the domain and the other parameters of the model. In particular, it is very important to maintain for the injected plasma, the Magnetic Reynolds number much greater than one; in fact, in this condition the particle of the plasma are forced to follow trajectories around the coil, in this way extending the coil of current that generates the magnetosphere.

Also the interaction parameter, which represents the ratio between the electromagnetic forces and the inertia forces, must be maintained much larger than one, so that the fluid streamlines are heavily modified by the magnetic field distribution. This means that the plasma, injected from the center of the on-board coil, will be able to lead outward the magnetic field causing its extension far away from the aircraft.

It is also important that the Reynolds number for solar wind is much higher than one. This means in fact a greater fluid-dynamic resistance coefficient and a greater thrust. As the velocity of the wind cannot be modified, the only way to increase the Reynolds number is that of enlarging the size of the sail.

4.5 Propulsions system FEM analysis

4.5.1 Thrust on the sail

Considering an analytical model, the force exerted by the solar wind on the M2P2 system can be expressed as:

$$F = C_d \frac{1}{2} \rho u_{sw}^2 S \quad (4.3)$$

where, $\frac{1}{2} \rho u_{sw}^2$ is the dynamic pressure exerted by the solar wind, u_{sw} is the velocity and ρ the density, $S = \pi L^2$ is the blocking area, L is the sub solar standoff distance. Theoretically, the velocity of vehicle will tend to the solar wind velocity, but the acceleration depends on the exerted thrust and on the weight of the spacecraft. The thrust coefficient C_d is the only unknown in equation (4.3) and it is theoretically derived for various scales of Magnetic sail [34] [35] [36] [31].

Starting from results retrieved from the literature and those obtained by the FEM model implemented by using the commercial software COMSOL, the thrust exerted by the wind has been evaluated for different operating conditions. The system is a simple bi-dimensional geometry (see Table 4.5) with a 10 m side square domain, a coil, and a plasma injector positioned at the center. The solar wind flows from the left side of the domain and the plasma has been injected along the axial direction at the center of the coil.

As a simplifying hypothesis, except for the velocity, the same characteristics have been assumed for both the injected plasma and the solar wind (see Table 4.6).

Considering the solar sail as a solid body behaving as an obstacle to solar wind flow, the dynamic Reynolds number have been calculated considering the transverse dimension of the magnetopause. Its value has been shown in Table 4.7.

Table 4.4: Geometrical parameter.

Physical quantity	Symbol	Value [units]
Diameter of the coil	d	0.2 [m]
Radius of coil	R	0.005 [m]
Length of domain	L	10 [m]
Length of injector	$d/8$	0.025 [m]

Table 4.5: Parameter of plasma and solar wind

Parameter	Description	Simulated values
μ_r	Relative magnetic permeability	1
ε_r	Relative electric permittivity	1
σ [S/m]	Electrical conductivity	10^8
μ_d [m^2/s]	Dynamic viscosity	10^{-4}
γ	Heat capacity ratio	1.4
k [$W/(m \cdot K)$]	Thermal conductivity	k (T)
c [m/s]	Speed of sound	c (T)
ρ [kg/m^3]	Mass density	(p, T) (Perfect gas law)
V [m/s]	Velocity plasma	5

Table 4.6: Reynolds number in the solar wind

Reynolds number: $R_e = \frac{\rho V D}{\mu_d}$	
ρ [kg/m^3]	1
V_w [m/s]	1
D [m]	1,14
μ_d [m^2/s]	10^{-4}
$R_e = 11400$	

Due to the surface currents, which confine the magnetic field within the magnetopause, in the outer space of the magnetopause, the effects of the magnetic field were considered negligible, and then the Magnetic Reynolds number, the Interaction parameter and the Hartmann number have been neglected in this analysis.

For the calculation of the thrust, the following considerations were made: the solar sail behaves, to the effects of fluid dynamics, like a stocky body, but the application of (4.3) is troublesome as the thrust coefficient is unknown. This in fact depends on the shape of the solid body but the magnetopause system has a shape that changes over the time.

Moreover, one cannot evaluate the magnetic pressure on the surface of magnetopause, because there isn't a surface where the velocity is null, as it happens for solid bodies. For these reasons, the value of the resulting thrust has been calculated on the cross sections of the two coils, taking into account the interaction between the applied electric current and the induction field.

At rest, namely without wind and plasma injection, the current circulating in the coil gives rise to a magnetic field, which exerts a force which tends to widen the coil. For symmetry, the forces in the two cross sections, due to the interaction between induction field and electrical current, are in equilibrium, and the coil does not undergo any acceleration. The same reasoning holds valid if a plasma is injected at the center of the coil, in a vertical direction, in absence of wind. On the contrary, the presence of the wind deforms the magnetosphere, making it asymmetric. As an effect, the forces applied to the two cross sections of the coil are no longer in equilibrium, and this determines an accelerating thrust. One can interpret this phenomenon as the way the magnetic field translates on the coil the thrust that the wind exerts on the magnetopause. The wind deforms the magnetosphere even no plasma is injected from the center of the solid coil. The injection of the plasma enlarges the magnetosphere, and then the imbalance between the forces applied to the two cross sections of the coils increases, and finally the thrust increases too (see fig. 4.17) increases the thrust of the wind.

The Table 4.8 shows the values of the resulting force in the tests carried out, where the force has been calculated as integral, on the section of the coil, of the product between the current density J in the coil and the vertical component of magnetic field B_y .

In the case of the simple magnetic dipole, the resultant force has been calculated considering a steady state configuration, in order to avoid any deformation of the stream-line of magnetic field

over time. In this case, the magnetic field, in the absence of interactions with moving fluids, will give rise to resultant force converging to zero.

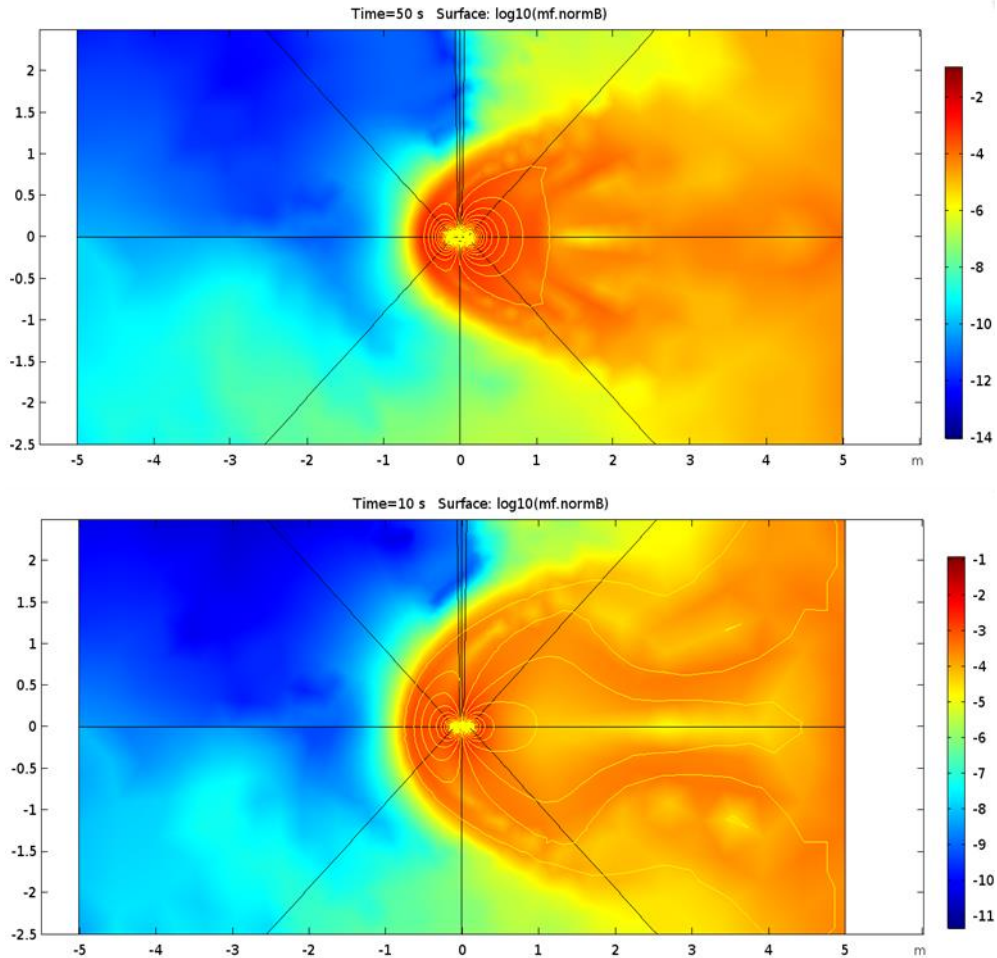


Figure 4.13: Deformation of the magnetosphere without plasma (above) and with plasma (below)

Table 4.7: Values of the resulting thrust.

TEST	Force on the left coil F_l [N/m]	Force on the right coil F_r [N/m]	Resultant Force R [N/m]
Magnetic field	-8.1788	8.186	0
Magnetic field + Solar wind	-7.330	7.609	0.279
Magnetic field +solar wind + injector plasma	-7.840	8.376	0.536

In Figg. 4.18 and 4.19 the time diagrams of the force calculated on two sections of the coil and the trend of the net thrust applied to the vehicle before and after plasma injection are shown.

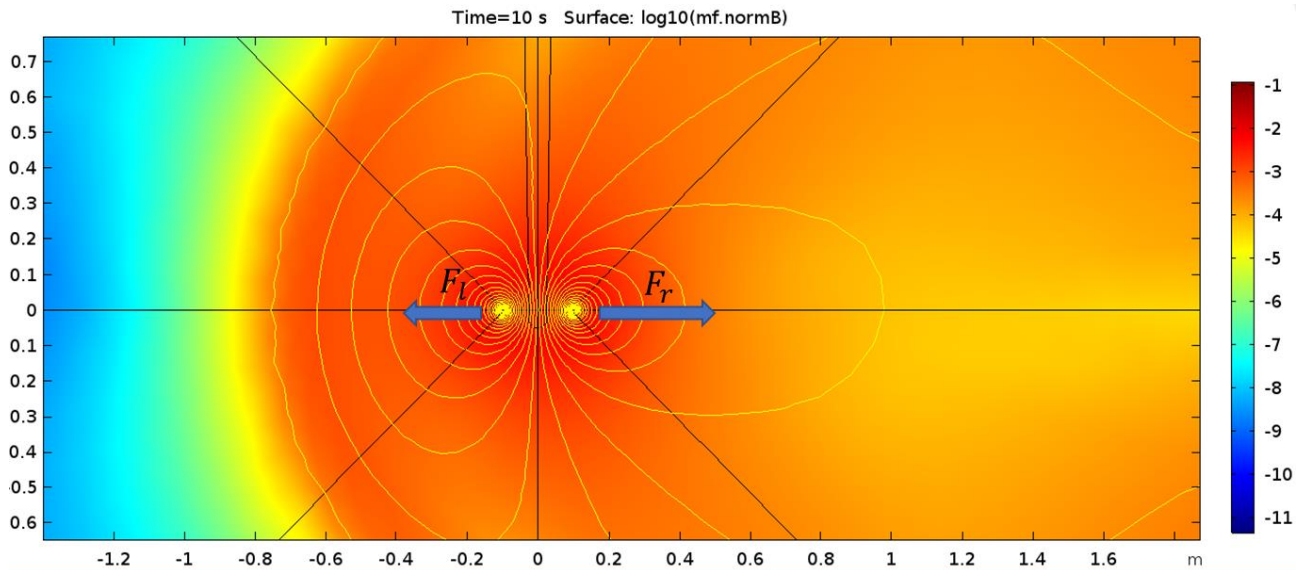


Figure 4.14: Forces applied to the two cross sections

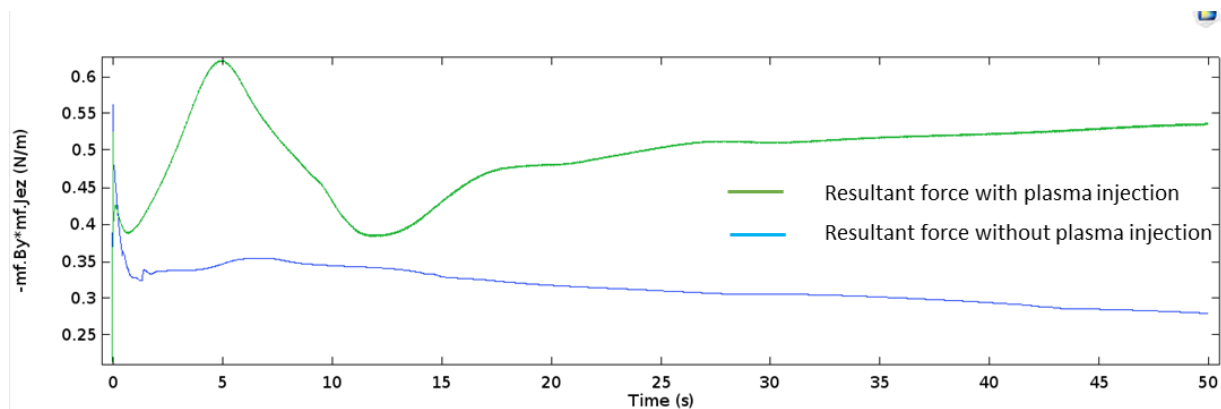


Figure 4.15: Net thrust applied on the solid coil with and without plasma injection

It is clear that the transitional regime is not yet concluded at the end of the test, which lasted 50 seconds. On the other hand, in this first phase of study, it is not possible to predict how long the transitional regime will last to have an evaluation of the resulting force in steady-state conditions. For the aim of the study, it is sufficient to demonstrate that the injection of the plasma is able to increase the thrust, and that this enhancement increases during the time.

It can be seen also that the initial phase of the transient regime produces a clear perturbation in the resultant force during the plasma injection. It is worth to remark that the FEM model has been developed to represent the behavior of the real system, laboratory setup or real application, in stationary conditions, therefore transient phenomena observed in simulation may not be present in the real case. For example, in the numerical model the injected plasma encounters resistance by the mean at rest, while in the Space the plasma is injected in the vacuum. Nevertheless, the transient

analysis becomes compulsory in the case of plasma injection or wind, to guarantee the convergence of the model.

4.6 Propulsions system dimensionless analysis

This paragraph shows an application of dimensionless analysis reported in the Section 2 of this dissertation; all values of parameters in the previous FEM simulation, chosen as the reference study, the independent and dependent reference scales are show in the Table 4.9.

Table 4.8: Dimensional and dimensionless parameters in the previous FEM simulation

Dimension parameters (FEM analysis)	Independent reference scales	Dependent reference scales	dimensionless parameters
$V_p = V_w = 5[m/s]$	$V_0 = 5[m/s]$		$V' = \frac{V_p}{V_0} = 5$
$d = 0.2[m]$	$D_0 = 0.2[m]$		$d' = \frac{d}{D_0}$
$\sigma_p = \sigma_w = 10^8[S/m]$		$\sigma_0 = \sigma$	$\sigma' = \frac{\sigma}{\sigma_0} = 1$
$\mu_p = \mu_w = 10^{-4}[Pa/s]$			$\mu_{d'} = \frac{V_0}{Ha^2}$
$\rho_p = \rho_w = 1 [kg/m^3]$	$\rho_0 = \sigma B_0^2 D_0 / V_0 [kg/m^3]$		$\rho' = \frac{1}{N}$
$B = 0.0052[T]$	$B_0 = 1[T]$		$B' = \frac{B}{B_0}$
$t = 10[s]$	$t_0 = D_0 / V_0$		$t' = \frac{t}{t_0} = \frac{V_0}{D_0}$
$\mu_0 = 4\pi 10^{-7} [H/m]$			$\mu_0' = R_m$

To limit the computational burden, the same velocity and the same physical properties has been assumed for the solar wind and plasma.

The dimensionless parameters shown in Table 4.10 refer to the area inside the magnetopause, where the dimensionless parameter have been calculated considering the diameter D of coil and the magnetic field in a representative point along the axis of coil.

Table 4.9: Dimensionless parameters

Name parameter	Reynolds number Re	Magnetic Reynolds number R_m	Hartmann number Ha	Interaction parameter N
Definition	$\frac{D\rho V}{\mu_d} = 10000$	$DV\sigma\mu_0 = 125.6$	$BD\sqrt{\frac{\sigma}{\mu_d}} = 440$	$\frac{\sigma B^2 D}{\rho V} = 19.36$

Now, the dimensionless numbers can be set, and changing some reference values, taking into account the relations previously described, new reference values can be obtained that allow one to extend this solution to the whole class of systems having the same dimensionless numbers.

As a first example, only an independent reference value has been changed and the others will change in order to keep unchanged the dimensionless numbers.

In Table 4.11, the modified values of the parameters are reported, corresponding to the velocity of plasma equal to $V = 100$.

Table 4.10: New parameters after change of velocity.

Symbol	Reference value	Reference value after dimensionless analysis
$V = V_0$	5 [m/s]	100 [m/s]
$D = D_0$	0.2 [m]	0.2 [m]
B	0.0022 [T]	0.00984 [T]
μ_d	10^{-4} [Pa/s]	10^{-4} [Pa/s]
ρ	1 [kg/m ³]	0.05 [kg/m ³]
$\sigma = \sigma_0$	10^8 [S/m]	$5 \cdot 10^6$ [S/m]

In Table 4.12, the reference values are calculated by changing the value of induction field from 0.022 [T] to 2 [T]. Finally, in Table 4.13, the new reference values of the parameters are shown when the density changes from 1 [kg/m³] to 10^{-4} [kg/m³].

Table 4.11: New parameters after change of Magnetic field

Symbol	Reference value	Reference value after dimensionless analysis
$V=V_0$	5 [m/s]	4132231 [m/s]
$D = D_0$	0.2 [m]	0.2 [m]
B	0.0022 [T]	2 [T]
μ_d	10^{-4} [Pa/s]	10^{-4} [Pa/s]
ρ	1 [kg/m ³]	0.00000121[kg/m ³]
$\sigma = \sigma_0$	10^8 [S/m]	121[S/m]

Table 4.12: New parameters after change of density.

Symbol	Reference value	Reference value after dimensionless analysis
$V=V_0$	5 [m/s]	50000 [m/s]
$D = D_0$	0.2 [m]	0.2 [m]
B	0.0022 [T]	0.22[T]
μ_d	10^{-4} [Pa/s]	10^{-4} [Pa/s]
ρ	1 [kg/m ³]	0.0001 [kg/m³]
$\sigma = \sigma_0$	10^8 [S/m]	10000 [S/m]

4.7 Conclusion

In this section, the analysis method developed in the previous sections has been applied to the study of the Space propulsion system called Mini-Magnetosphere Plasma Propulsion (M2P2). Such system exploits the solar wind to thrust a Space vehicle, acting as a sail. The solar wind is constituted by electrons and protons traveling at high velocity, therefore they are subject to the influence of a magnetic field, as it happens for the terrestrial magnetosphere. The M2P2 system is an innovative design of solar sail, which consists in creating a mini-magnetosphere by means of a plasma current surrounding the vehicle. Such plasma current is formed by ejecting a plasma from the center of a coil integral with the vehicle, and where an electrical current is circulating. For given operative conditions, mainly the value of interaction parameter, the plasma ejected from the vehicle is magnetized by the coil, and circulates around the vehicle. As an effect, the magnetosphere generated by the coil is inflated, and a larger sail is opposed to the wind.

In this study, two specific aspects have been considered. The first one concerns the operative conditions that allow the ejected plasma to be captured by the magnetic field, in this way inflating the sail. The second one, concerns the calculation of the thrust that the wind exerts on the sail. The analysis has been performed resorting to the non-dimensional analysis, on one side to reduce the computational burden of the FEM analysis, on the other side because it made it possible to perform at the same time the analysis of the real application and a possible experimental setup on ground.

One last remark concerns a possible use of this technology. In the last decades, more and more Space agencies are considering the possibility of asteroids belt mining. Such belt is 1.5 [AU] from the orbit of the Earth, therefore a propulsion system that harvests the energy from the environment could represent a valid solution. In fact, the equation of the rockets reveals that they are not suitable for long travels, as most part of the load must be fuel. As reported in the literature [30] the M2P2 system could allow to reach a velocity of 80 [km/s]. This means that the destination could be reached in 6 months. For the return journey, which is done at full load, the mass is no longer an obstacle, because the gravitational attraction of the Sun can be used as propulsion system, all the vehicle needs is to reduce its orbital velocity, so that the centrifugal force no longer compensates the gravitational force. To this end, it is possible to evaluate a proper launch system installed in the asteroid. In the hypothesis of setting to zero the orbital velocity of the vehicle, it can be demonstrated that the time needed to reach the Earth orbit would be less than the outward journey.

5 Appendix

5.1 Appendix 1.

Contribution to the magnetic field due to the walls

Referring to Fig. 5.1 and considering the upper wall of the domain, the contribution of an element of current $dI = J(\xi, \eta) \cdot d\xi d\eta$ to the magnetic field in a general point $M(x, y)$ can be obtained by applying the Ampère's law:

$$2\pi r \cdot dB = \mu \cdot dI = \mu \cdot J(\xi, \eta) \cdot d\xi d\eta$$

$$dB = \frac{\mu J(\xi, \eta) d\xi d\eta}{2\pi \sqrt{(x - \xi)^2 + (\eta - y)^2}}$$

$$r^2 = (x - \xi)^2 + (\eta - y)^2 \quad \Rightarrow \quad r = \sqrt{(x - \xi)^2 + (\eta - y)^2}$$

$$PH = (\eta - y) = r \cos\theta = \sqrt{(x - \xi)^2 + (\eta - y)^2} \cos\theta \quad \Rightarrow \quad \cos\theta = \frac{(\eta - y)}{\sqrt{(x - \xi)^2 + (\eta - y)^2}}$$

$$HM = (x - \xi) = r \sin\theta = \sqrt{(x - \xi)^2 + (\eta - y)^2} \sin\theta \quad \Rightarrow \quad \sin\theta = \frac{(x - \xi)}{\sqrt{(x - \xi)^2 + (\eta - y)^2}}$$

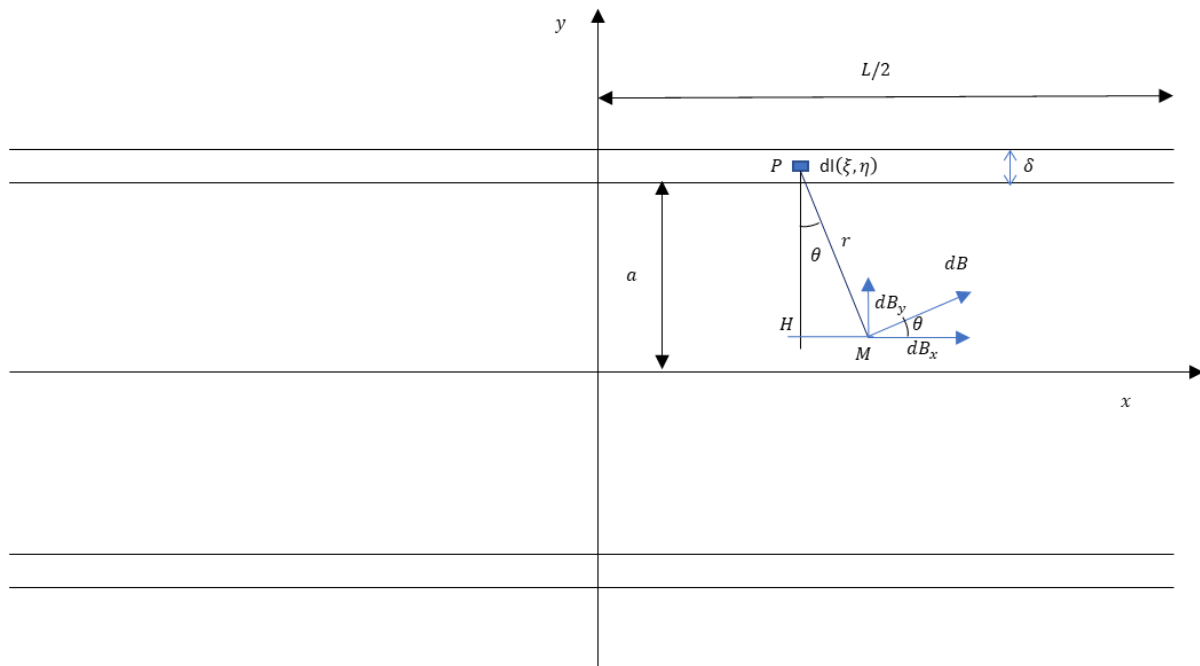


Figure 5.1: Magnetic field generate by the small element on the upper wall.

$$dB_x = dB \cos\theta = dB \frac{(\eta-y)}{\sqrt{(x-\xi)^2+(\eta-y)^2}} = \frac{\mu J(\xi,\eta) d\xi d\eta}{2\pi\sqrt{(x-\xi)^2+(\eta-y)^2}} \frac{(\eta-y)}{\sqrt{(x-\xi)^2+(\eta-y)^2}} = \frac{\mu J}{2\pi} \left[\frac{(\eta-y)}{(x-\xi)^2+(\eta-y)^2} \right] d\xi d\eta$$

$$dB_y = dB \sin\theta = dB \frac{(x-\xi)}{\sqrt{(x-\xi)^2+(\eta-y)^2}} = \frac{\mu J(\xi,\eta) d\xi d\eta}{2\pi\sqrt{(x-\xi)^2+(\eta-y)^2}} \frac{(x-\xi)}{\sqrt{(x-\xi)^2+(\eta-y)^2}} = \frac{\mu J}{2\pi} \left[\frac{(x-\xi)}{(x-\xi)^2+(\eta-y)^2} \right] d\xi d\eta$$

The B_x component due to the entire upper wall can be expressed in the following way

$$\begin{aligned} B_x &= \frac{\mu J}{2\pi} \int_{-\frac{L}{2}}^{\frac{L}{2}} d\xi \int_a^{a+\delta} \frac{(\eta-y)}{(x-\xi)^2+(\eta-y)^2} d\eta = \frac{J}{4\pi} \int_{-\frac{L}{2}}^{\frac{L}{2}} d\xi \int_a^{a+\delta} \frac{2(\eta-y)}{(x-\xi)^2+(\eta-y)^2} d\eta = \\ &= \frac{\mu J}{4\pi} \int_{-\frac{L}{2}}^{\frac{L}{2}} \left[\ln[(x-\xi)^2 + (\eta-y)^2] \right]_a^{a+\delta} d\xi = \\ &= \frac{J}{4\pi} \int_{-\frac{L}{2}}^{\frac{L}{2}} \ln[(x-\xi)^2 + (a+\delta-y)^2] - \ln[(x-\xi)^2 + (a-y)^2] d\xi \end{aligned}$$

Integrating by parts:

$$\begin{aligned} B_x &= \frac{\mu J}{4\pi} \left\{ (x-\xi) \ln[(x-\xi)^2 + (a+\delta-y)^2] - 2(x-\xi) + 2(a+\delta-y) \operatorname{atan}\left(\frac{x-\xi}{a+\delta-y}\right) + \right. \\ &\quad \left. -(x-\xi) \ln[(x-\xi)^2 + (a-y)^2] + 2(x-\xi) - 2(a-y) \operatorname{atan}\left(\frac{x-\xi}{a-y}\right) \right\}_{-\frac{L}{2}}^{\frac{L}{2}} = \\ &= \frac{\mu J}{4\pi} \left\{ (x-\xi) \cdot \ln \frac{(x-\xi)^2+(a+\delta-y)^2}{(x-\xi)^2+(a-y)^2} + 2(a+\delta-y) \operatorname{atan}\left(\frac{x-\xi}{a+\delta-y}\right) - 2(a-y) \operatorname{atan}\left(\frac{x-\xi}{a-y}\right) \right\}_{-\frac{L}{2}}^{\frac{L}{2}} = \\ &= \frac{\mu J}{4\pi} \left\{ \left(x - \frac{L}{2}\right) \ln \left(1 + \frac{\delta^2 - 2y\delta + 2a\delta}{\left(x - \frac{L}{2}\right)^2 + (a-y)^2}\right) + 2(a+\delta-y) \operatorname{atan}\left(\frac{x - \frac{L}{2}}{a+\delta-y}\right) - 2(a-y) \operatorname{atan}\left(\frac{x - \frac{L}{2}}{a-y}\right) + \right. \\ &\quad \left. - \left(x + \frac{L}{2}\right) \ln \left(1 + \frac{\delta^2 - 2y\delta + 2a\delta}{\left(x + \frac{L}{2}\right)^2 + (a-y)^2}\right) - 2(a+\delta-y) \operatorname{atan}\left(\frac{x + \frac{L}{2}}{a+\delta-y}\right) + 2(a-y) \operatorname{atan}\left(\frac{x + \frac{L}{2}}{a-y}\right) \right\} = \end{aligned}$$

$$\begin{aligned} B_x &= \frac{\mu J}{4\pi} \left\{ \left(x - \frac{L}{2}\right) \ln \left(1 + \frac{\delta^2 - 2y\delta + 2a\delta}{\left(x - \frac{L}{2}\right)^2 + (a-y)^2}\right) - \left(x + \frac{L}{2}\right) \ln \left(1 + \frac{\delta^2 - 2y\delta + 2a\delta}{\left(x + \frac{L}{2}\right)^2 + (a-y)^2}\right) + \right. \\ &\quad \left. + 2(a+\delta-y) \left[\operatorname{atan}\left(\frac{x - \frac{L}{2}}{a+\delta-y}\right) - \operatorname{atan}\left(\frac{x + \frac{L}{2}}{a+\delta-y}\right) \right] - 2(a-y) \left[\operatorname{atan}\left(\frac{x - \frac{L}{2}}{a-y}\right) - \operatorname{atan}\left(\frac{x + \frac{L}{2}}{a-y}\right) \right] \right\} \quad (5.1) \end{aligned}$$

Regarding the calculation of the B_y component:

$$dB_y = \frac{\mu J}{2\pi} \left[\frac{(x-\xi)}{(x-\xi)^2 + (\eta-y)^2} \right] d\xi d\eta$$

$$B_y = \frac{\mu J}{2\pi} \int_a^{a+\delta} d\eta \int_{-\frac{L}{2}}^{\frac{L}{2}} \frac{(x-\xi)}{(x-\xi)^2 + (\eta-y)^2} d\xi = \frac{J}{4\pi} \int_a^{a+\delta} d\eta \int_{-\frac{L}{2}}^{\frac{L}{2}} \frac{2(x-\xi)}{(x-\xi)^2 + (\eta-y)^2} d\xi =$$

$$= \frac{J}{4\pi} \int_a^{a+\delta} [\ln(x-\xi)^2 + (\eta-y)^2]_{-\frac{L}{2}}^{\frac{L}{2}} d\eta =$$

$$= \frac{\mu J}{4\pi} \int_a^{a+\delta} \ln \left[\left(x - \frac{L}{2}\right)^2 + (\eta-y)^2 \right] - \ln \left[\left(x + \frac{L}{2}\right)^2 + (\eta-y)^2 \right] d\eta$$

Integrating by parts:

$$B_y = \frac{\mu J}{4\pi} \left\{ (\eta-y) \ln \left[\left(x - \frac{L}{2}\right)^2 + (\eta-y)^2 \right] - 2(\eta-y) + 2 \left(x - \frac{L}{2}\right) \operatorname{atan} \left(\frac{\eta-y}{x - \frac{L}{2}} \right) + \right.$$

$$\left. - (\eta-y) \ln \left[\left(x + \frac{L}{2}\right)^2 + (\eta-y)^2 \right] + 2(\eta-y) - 2 \left(x + \frac{L}{2}\right) \operatorname{atan} \left(\frac{\eta-y}{x + \frac{L}{2}} \right) \right\}_a^{a+\delta} =$$

$$= \frac{\mu J}{4\pi} \left\{ (\eta-y) \ln \left[\frac{\left(x - \frac{L}{2}\right)^2 + (\eta-y)^2}{\left(x + \frac{L}{2}\right)^2 + (\eta-y)^2} \right] + 2 \left(x - \frac{L}{2}\right) \operatorname{atan} \left(\frac{\eta-y}{x - \frac{L}{2}} \right) - 2 \left(x + \frac{L}{2}\right) \operatorname{atan} \left(\frac{\eta-y}{x + \frac{L}{2}} \right) \right\}_a^{a+\delta} =$$

$$= \frac{\mu J}{4\pi} \left\{ (a+\delta-y) \ln \left[\frac{\left(x - \frac{L}{2}\right)^2 + (a+\delta-y)^2}{\left(x + \frac{L}{2}\right)^2 + (a+\delta-y)^2} \right] - (a-y) \ln \left[\frac{\left(x - \frac{L}{2}\right)^2 + (a-y)^2}{\left(x + \frac{L}{2}\right)^2 + (a-y)^2} \right] + \right.$$

$$\left. + 2 \left(x - \frac{L}{2}\right) \left[\operatorname{atan} \left(\frac{a+\delta-y}{x - \frac{L}{2}} \right) - \operatorname{atan} \left(\frac{a-y}{x - \frac{L}{2}} \right) \right] - 2 \left(x + \frac{L}{2}\right) \left[\operatorname{atan} \left(\frac{a+\delta-y}{x + \frac{L}{2}} \right) - \operatorname{atan} \left(\frac{a-y}{x + \frac{L}{2}} \right) \right] \right\} \quad (5.2)$$

As validation, one can see that $B_y(0, y) = 0$.

5.2 Appendix 2.

Contribution to the field due to the current distribution $\Gamma(\alpha)$ and $q(\alpha)$

As said before, the surface distribution of current is caused by the currents circulating in the walls and the discontinuous magnetic permeability. To simplify the calculations, for this calculation one can assume: $\delta = 0$, namely, the thickness δ of the solenoid is negligible with respect to other lengths. In this case, B_x^{up+low} and B_y^{up+low} expressions become respectively:

$$\begin{aligned} B_x^{up+low} &= \frac{\mu_{flu} J}{2\pi} \left\{ \operatorname{atan} \left(\frac{\frac{L}{2}-x}{a-y} \right) + \operatorname{atan} \left(\frac{x+\frac{L}{2}}{a-y} \right) + \operatorname{atan} \left(\frac{\frac{L}{2}-x}{a+y} \right) + \operatorname{atan} \left(\frac{x+\frac{L}{2}}{a+y} \right) \right\} \\ B_y^{up+low} &= \frac{\mu_{flu} J}{4\pi} \left\{ \ln \left[\frac{\left(\frac{L}{2}-x\right)^2 + (a-y)^2}{\left(\frac{L}{2}+x\right)^2 + (a-y)^2} \right] + \ln \left[\frac{\left(\frac{L}{2}+x\right)^2 + (a+y)^2}{\left(\frac{L}{2}-x\right)^2 + (a+y)^2} \right] \right\} \end{aligned} \quad (5.3)$$

So, starting for: $2\pi r dB_M^\Gamma = \mu_{flu} \Gamma(\alpha) R d\alpha$ and $2\pi r dB^q = \mu_{flu} q(\alpha) R d\alpha$ and considering the horizontal and vertical component of induction magnetic field due to the vortex Γ and the dipole q , using these last expressions (5.3) it is possible to define both the distributions $\Gamma(\alpha)$ and $q(\alpha)$:

$$\Gamma(\alpha) = \frac{B_{\theta(flu)}}{\mu_{flu}} \left(1 - \frac{\mu_{flu}}{\mu_{cy}} \right) = \frac{B_x^{up+low} \sin(\alpha) - B_y^{up+low} \cos(\alpha)}{\mu_{flu}} \left(1 - \frac{\mu_{flu}}{\mu_{cy}} \right) \quad (5.4)$$

$$q(\alpha) = \frac{B_r(flu)}{\mu_{flu}} \left(1 - \frac{\mu_{flu}}{\mu_{cy}} \right) = \frac{B_x^{up+low} \cos(\alpha) + B_y^{up+low} \sin(\alpha)}{\mu_{flu}} \left(1 - \frac{\mu_{flu}}{\mu_{cy}} \right) \quad (5.5)$$

Replacement the expressions (5.3) the (5.4) and (5.5) can re-written in terms of the angle α

$$\Gamma(\alpha) =$$

$$\frac{J}{4\pi} \left(1 - \frac{\mu_{flu}}{\mu_{cy}} \right) \left\{ 2 \operatorname{atan} \left[\frac{\frac{L}{2} \pm R \cos \alpha}{a \pm R \sin \alpha} \right] \sin \alpha - \left[\ln \frac{\left(\frac{L}{2} - R \cos \alpha\right)^2 + (a - R \sin \alpha)^2}{\left(\frac{L}{2} + R \cos \alpha\right)^2 + (a - R \sin \alpha)^2} + \ln \frac{\left(\frac{L}{2} + R \cos \alpha\right)^2 + (a + R \sin \alpha)^2}{\left(\frac{L}{2} - R \cos \alpha\right)^2 + (a + R \sin \alpha)^2} \right] \cos \alpha \right\} \quad (5.7)$$

$$q(\alpha) =$$

$$\frac{J}{4\pi} \left(1 - \frac{\mu_{flu}}{\mu_{cy}} \right) \left\{ 2 \operatorname{atan} \left[\frac{\frac{L}{2} \pm R \cos \alpha}{a \pm R \sin \alpha} \right] \cos \alpha + \left[\ln \frac{\left(\frac{L}{2} - R \cos \alpha\right)^2 + (a - R \sin \alpha)^2}{\left(\frac{L}{2} + R \cos \alpha\right)^2 + (a - R \sin \alpha)^2} + \ln \frac{\left(\frac{L}{2} + R \cos \alpha\right)^2 + (a + R \sin \alpha)^2}{\left(\frac{L}{2} - R \cos \alpha\right)^2 + (a + R \sin \alpha)^2} \right] \sin \alpha \right\} \quad (5.8)$$

5.3 Appendix 3.

Summary of boundary conditions of magnetic induction field

Table 5.1 summarizes all the boundary conditions for the magnetic induction field where expressions have been simplified with following hypothesis:

$$\delta \ll a; \text{ and } \delta \rightarrow 0; a \ll L$$

If the thickness $\delta \rightarrow 0$ we can assume constant the current density J .

Table 5.1: Summary of boundary conditions of magnetic induction field

Boundary Condition	Symbols	Expression of total Magnetic field
Upper wall	$B_x^1(J)$	$\frac{\mu_{flu} J}{2\pi} \left\{ \pi + \operatorname{atan} \left(\frac{\frac{L}{2} - x}{2a} \right) + \operatorname{atan} \left(\frac{x + \frac{L}{2}}{2a} \right) \right\} + \frac{\mu_{flu} R}{2\pi} \int_{-\pi}^{\pi} \frac{\Gamma(\alpha) (h \sin \gamma - R \cos \alpha)}{[h^2 - 2hR \cos(\alpha - \gamma) + R^2]} d\alpha$ $+ \frac{\mu_{flu}}{4\pi} \int_{-\pi}^{\pi} \left[\frac{3r \cos(\alpha - \psi) + qr \cos \psi}{r^5} - \frac{q \cos \alpha}{r^3} \right] \sin \eta \, d\alpha$
	$B_y^1(J)$	$\frac{\mu_{flu} J}{4\pi} \left\{ \ln \left[\frac{\left(\frac{L}{2} - x\right)^2}{\left(\frac{L}{2} + x\right)^2} \right] + \ln \left[\frac{\left(\frac{L}{2} + x\right)^2 + (2a)^2}{\left(\frac{L}{2} - x\right)^2 + (2a)^2} \right] \right\} - \frac{\mu_{flu} R}{2\pi} \int_{-\pi}^{\pi} \frac{\Gamma(\alpha) (h \cos \gamma - R \cos \alpha)}{[h^2 - 2hR \cos(\alpha - \gamma) + R^2]} d\alpha$ $+ \frac{\mu_{flu}}{4\pi} \int_{-\pi}^{\pi} \left[\frac{3r \sin(\alpha - \psi) + qr \cos \psi}{r^5} - \frac{q \sin \alpha}{r^3} \right] \cos \eta \, d\alpha$
Lower Wall	$B_x^2(J)$	$\frac{\mu_{flu} J}{2\pi} \left\{ \operatorname{atan} \left(\frac{\frac{L}{2} - x}{2a} \right) + \operatorname{atan} \left(\frac{x + \frac{L}{2}}{2a} \right) + \pi \right\} + \frac{\mu_{flu} R}{2\pi} \int_{-\pi}^{\pi} \frac{\Gamma(\alpha) (h \sin \gamma - R \cos \alpha)}{[h^2 - 2hR \cos(\alpha - \gamma) + R^2]} d\alpha$ $+ \frac{\mu_{flu}}{4\pi} \int_{-\pi}^{\pi} \left[\frac{3r \cos(\alpha - \psi) + qr \cos \psi}{r^5} - \frac{q \cos \alpha}{r^3} \right] \sin \eta \, d\alpha$
	$B_y^2(J)$	$\frac{\mu_{flu} J}{4\pi} \left\{ \ln \left[\frac{\left(\frac{L}{2} - x\right)^2 + (2a)^2}{\left(\frac{L}{2} + x\right)^2 + (2a)^2} \right] + \ln \left[\frac{\left(\frac{L}{2} + x\right)^2}{\left(\frac{L}{2} - x\right)^2} \right] \right\} - \frac{\mu_{flu} R}{2\pi} \int_{-\pi}^{\pi} \frac{\Gamma(\alpha) (h \cos \gamma - R \cos \alpha)}{[h^2 - 2hR \cos(\alpha - \gamma) + R^2]} d\alpha$ $+ \frac{\mu_{flu}}{4\pi} \int_{-\pi}^{\pi} \left[\frac{3r \sin(\alpha - \psi) + qr \cos \psi}{r^5} - \frac{q \sin \alpha}{r^3} \right] \cos \eta \, d\alpha$
Cylinder	$B_x^3(J)$	$\frac{\mu_{flu} J}{2\pi} \left\{ \operatorname{atan} \left(\frac{\frac{L}{2} - x}{a - y} \right) + \operatorname{atan} \left(\frac{x + \frac{L}{2}}{a - y} \right) + \operatorname{atan} \left(\frac{\frac{L}{2} - x}{a + y} \right) + \operatorname{atan} \left(\frac{x + \frac{L}{2}}{a + y} \right) \right\}$ $+ \frac{\mu_{flu} R}{2\pi} \int_{-\pi}^{\pi} \frac{\Gamma(\alpha) (h \sin \gamma - R \cos \alpha)}{[h^2 - 2hR \cos(\alpha - \gamma) + R^2]} d\alpha$ $+ \frac{\mu_{flu}}{4\pi} \int_{-\pi}^{\pi} \left[\frac{3r \cos(\alpha - \psi) + qr \cos \psi}{r^5} - \frac{q \cos \alpha}{r^3} \right] \sin \eta \, d\alpha$

	$B_y^3(J)$	$\frac{\mu_{flu}J}{4\pi} \left\{ \ln \left[\frac{\left(\frac{L}{2} - x\right)^2 + (a - y)^2}{\left(\frac{L}{2} + x\right)^2 + (a - y)^2} \right] + \ln \left[\frac{\left(\frac{L}{2} + x\right)^2 + (a + y)^2}{\left(\frac{L}{2} - x\right)^2 + (a + y)^2} \right] \right\}$ $- \frac{\mu_{flu}R}{2\pi} \int_{-\pi}^{\pi} \frac{\Gamma(\alpha)(h\cos\gamma - R\cos\alpha)}{[h^2 - 2hR\cos(\alpha - \gamma) + R^2]} d\alpha$ $+ \frac{\mu_{flu}}{4\pi} \int_{-\pi}^{\pi} \left[\frac{3r\sin(\alpha - \psi) + qr\cos\psi}{r^5} - \frac{q\sin\alpha}{r^3} \right] \cos\eta d\alpha$
Inlet	$B_x^4(J)$	$\frac{\mu_{flu}J}{2\pi} \left\{ \operatorname{atan} \left(\frac{\frac{L}{2} + 1.1}{a - y} \right) + \operatorname{atan} \left(\frac{-1.1 + \frac{L}{2}}{a - y} \right) + \operatorname{atan} \left(\frac{\frac{L}{2} + 1.1}{a + y} \right) + \operatorname{atan} \left(\frac{-1.1 + \frac{L}{2}}{a + y} \right) \right\}$ $+ \frac{\mu_{flu}R}{2\pi} \int_{-\pi}^{\pi} \frac{\Gamma(\alpha)(h\sin\gamma - R\cos\alpha)}{[h^2 - 2hR\cos(\alpha - \gamma) + R^2]} d\alpha$ $+ \frac{\mu_{flu}}{4\pi} \int_{-\pi}^{\pi} \left[\frac{3r\cos(\alpha - \psi) + qr\cos\psi}{r^5} - \frac{q\cos\alpha}{r^3} \right] \sin\eta d\alpha$
	$B_y^4(J)$	$\frac{\mu_{flu}J}{4\pi} \left\{ \ln \left[\frac{\left(\frac{L}{2} + 1.1\right)^2 + (a - y)^2}{\left(\frac{L}{2} - 1.1\right)^2 + (a - y)^2} \right] + \ln \left[\frac{\left(\frac{L}{2} - 1.1\right)^2 + (a + y)^2}{\left(\frac{L}{2} + 1.1\right)^2 + (a + y)^2} \right] \right\}$ $- \frac{\mu_{flu}R}{2\pi} \int_{-\pi}^{\pi} \frac{\Gamma(\alpha)(h\cos\gamma - R\cos\alpha)}{[h^2 - 2hR\cos(\alpha - \gamma) + R^2]} d\alpha$ $+ \frac{\mu_{flu}}{4\pi} \int_{-\pi}^{\pi} \left[\frac{3r\sin(\alpha - \psi) + qr\cos\psi}{r^5} - \frac{q\sin\alpha}{r^3} \right] \cos\eta d\alpha$
Outlet	$B_x^5(J)$	$\frac{\mu_{flu}J}{2\pi} \left\{ \operatorname{atan} \left(\frac{\frac{L}{2} - 1.1}{a - y} \right) + \operatorname{atan} \left(\frac{1.1 + \frac{L}{2}}{a - y} \right) + \operatorname{atan} \left(\frac{\frac{L}{2} - 1.1}{a + y} \right) + \operatorname{atan} \left(\frac{1.1 + \frac{L}{2}}{a + y} \right) \right\}$ $+ \frac{\mu_{flu}R}{2\pi} \int_{-\pi}^{\pi} \frac{\Gamma(\alpha)(h\sin\gamma - R\cos\alpha)}{[h^2 - 2hR\cos(\alpha - \gamma) + R^2]} d\alpha$ $+ \frac{\mu_{flu}}{4\pi} \int_{-\pi}^{\pi} \left[\frac{3r\cos(\alpha - \psi) + qr\cos\psi}{r^5} - \frac{q\cos\alpha}{r^3} \right] \sin\eta d\alpha$
	$B_y^5(J)$	$\frac{\mu_{flu}J}{4\pi} \left\{ \ln \left[\frac{\left(\frac{L}{2} - 1.1\right)^2 + (a - y)^2}{\left(\frac{L}{2} + 1.1\right)^2 + (a - y)^2} \right] + \ln \left[\frac{\left(\frac{L}{2} + 1.1\right)^2 + (a + y)^2}{\left(\frac{L}{2} - 1.1\right)^2 + (a + y)^2} \right] \right\}$ $- \frac{\mu_{flu}R}{2\pi} \int_{-\pi}^{\pi} \frac{\Gamma(\alpha)(h\cos\gamma - R\cos\alpha)}{[h^2 - 2hR\cos(\alpha - \gamma) + R^2]} d\alpha$ $+ \frac{\mu_{flu}}{4\pi} \int_{-\pi}^{\pi} \left[\frac{3r\sin(\alpha - \psi) + qr\cos\psi}{r^5} - \frac{q\sin\alpha}{r^3} \right] \cos\eta d\alpha$

Bibliography

- [1] S. Mandelli, “VIV su un cilindro: analisi sperimentale e modellazione numerica,” Politecnico di Milano, Milano, Italy, 2012.
- [2] A. Ongoren e D. Rockwell, «Flow structure from an oscillating cylinder Part 1. Mechanisms of phase shift and recovery in the near wake.,» *Journal of fluid Mechanics*, vol. 191, pp. 197-223, 1988.
- [3] M. M. Zdravkovich, «Different modes of vortex shedding: an overview,» *Journal of fluids and Structures*, vol. 10, n. 5, pp. 427-437, 1996.
- [4] R. D. Blevins, *Flow-induced vibration.*, New York: Van Nostrand Reinhold Co., 1977.
- [5] A. Techet, «Vortex induced vibration,» MIT OpenCourseWare, USA: Massachusetts Institute , 2005.
- [6] M. Sahin e R. G. Owens, «A numerical investigation of wall effects up to high blockage ratios on two-dimensional flow past a confined circular cylinder,» *Physics of Fluids*, vol. 16, n. 5, pp. 1305-1320, 2004.
- [7] C. Williamson, «Oblique and parallel modes of vortex shedding in the wake of a circular cylinder at low Reynolds numbers,» *Journal of Fluid Mechanic*, vol. 206, pp. 579-627, 1989.
- [8] R. D. Henderson, «Details of the drag curve near the onset of vortex shedding,» *Physics of Fluids*, vol. 7, n. 9, pp. 2102-2104, 1995.
- [9] O. Posdziech e R. Grundmann, «Numerical simulation of the flow around an infinitely long circular cylinder in the transition regime,» *Theoretical and Computational Fluid Dynamics*, vol. 15, n. 2, pp. 121-141, 2001.
- [10] R. Orselli, «Simulation numerique des tourbillons de Karman,» Grenoble, 2000.
- [11] P. Trichet, «Etude de l'écoulement autour d'un cylindre et de son sillage proche,» Toulouse, 1975.
- [12] «Drag coefficient,» *Encyclopædia Britannica*, [Online]. Available: <https://www.britannica.com/science/drag-coefficient>. [Consultato il giorno October 2019].

- [13] J. Lahjomri, P. Capéran e A. Alemany, «The cylinder wake in a magnetic field aligned with the velocity,» *Journal of Fluid Mechanics*, vol. 253, pp. 421-448, 1993.
- [14] M. Berhanu, «Magnétohydrodynamique turbulente dans les métaux liquides,» PhD Thesis, 2008.
- [15] G. Mutschke, G. Gerbeth, V. Shatrov e A. Tomboulides, «Two-and three-dimensional instabilities of the cylinder wake in an aligned magnetic field.,» *Physics of Fluids*, vol. 9, n. 11, pp. 3114-3116, 1997.
- [16] J. Lahjomri, P. Caperan, A. Alemany e S. Cristoloveanu, «On Local Measurements of the Up and Downstream Magnetic Wake of a Cylinder at Low Magnetic Reynolds Number,» *Liquid Metal Magnetohydrodynamics*, pp. 381-390, 1989.
- [17] A. Alemany e G. Gerbeth, «Study of the boundary layer around a cylinder and of the drag coefficient in an aligned magnetic field,» *Comptes Rendus de l'Academie des Sciences Series IIB Mechanics Physics Chemistry Astronomy*, vol. 7, n. 325, pp. 375-381, 1997.
- [18] «COMSOL Multiphysics® User's Guide. Version 5.1.,» [Online]. Available: <https://www.comsol.it/release/5.1>.
- [19] R. Asahi, I. Funaki, H. Ogawa, H. Yamakawa, K. Fujita e Y. Nakayama, «Numerical Study on Thrust Production Mechanism of a Magnetoplasma Sail,» in *40th AIAA/ASME/SAE/ASEE Joint Propulsion Conference and Exhibit.*, Fort Lauderdale, Florida, 2004.
- [20] A. Alemany, R. Forcinetti, F. Masson e A. Montisci, «FEM analysis of the inflation process of Magnetoplasma sails,» *Magnetohydrodynamics* , vol. 53, n. 2, 2017.
- [21] K. E. Tsiolkovsky, «Extension of man into outer space,» in *Proceedings of Symposium Jet Propulsion* , 1936.
- [22] K. Tsander, «From a scientific heritage,» NASA Technical Translation No. TTF-541, NASA, 1967.
- [23] P. Janhunen, « Electric sail for spacecraft propulsion,» *Journal of Propulsion and Power*, vol. 20, n. 4, pp. 763-764, 2004.
- [24] P. Janhunen e A. Sandroos, «Simulation study of solar wind push on a charged wire: basis of

solar wind electric sail propulsion,» *Annales Geophysicae*, vol. 25, n. 3, pp. 755-767, 2007.

- [25] P. Janhunen e e. al., «Invited Article: Electric solar wind sail: Toward test missions,» *Review of scientific instruments*, vol. 81, n. 11, p. 111301, 2010.
- [26] G. Mengali e A. A. Quarta, «Non-Keplerian orbits for electric sails,» *Celestial Mechanics and Dynamical Astronomy*, vol. 105, n. 1-3, pp. 179-195, 2009.
- [27] D. Andrews e R. Zubrin, «Magnetic sails and interstellar travel,» *Journal of British Interplanetary Society*, vol. 43, pp. 265-272, 1990.
- [28] I. Funaki, H. Kojima, H. Yamakawa e Y. S. Y. Nakayama, «Laboratory Experiment of Plasma Flow Around Magnetic Sail,» *Astrophysics and Space Science*, vol. 307, n. 1-3, 2007.
- [29] R. M. Winglee, «Mini-Magnetospheric Plasma Propulsion (M2P2),» NASA Innovative Advanced Concepts (NIAC), Award No. 07600-010, Final report. , NASA, 1999.
- [30] R. M. Winglee, J. Slough, T. Ziemba e A. Goodson, «Mini-magnetospheric plasma propulsion: Tapping the energy of the solar wind for spacecraft propulsion,» *Journal of Geophysical Research: Space Physics*, vol. 105, n. A9, pp. 21067-21077, 2000.
- [31] K. Ueno, I. Funaki, T. Kimura, H. Horisawa e H. Yamakawa, «Thrust Measurement of a Pure Magnetic Sail Using Parallelogram-Pendulum Method,» *Journal of Propulsion and Power*, vol. 25, n. 2, pp. 536-539, 2009.
- [32] I. Funaki, H. Yamakawa, Y. Kajimura, K. Ueno, Y. Oshio, H. Nishida, H. Usui, M. Matsumoto e I. Shinohara, «Experimental and Numerical Investigations on the Thrust Production Process of Magnetoplasma Sail,» in *AIAA Guidance, Navigation, and Control Conference*, Nashville, Tennessee, USA, 2010.
- [33] I. Funaki e H. Yamakawa, «Solar wind sails,» in *Exploring the Solar Wind*, IntechOpen, 2012.
- [34] D. Akita e K. Suzuki, «Kinetic analysis on plasma flow of solar wind around magnetic sail,» in *36th AIAA Plasmadynamics and Lasers Conference*, Toronto, Ontario, Canada, 2005.
- [35] K. Fujita, «Particle simulation of moderately-sized magnetic sails,» *The Journal of Space Technology and Science*, vol. 20, n. 2, pp. 2_26-2_31, 2004.
- [36] H. Nishida, H. Ogawa, I. Funaki, K. Fujita, H. Yamakawa e Y. Nakayama, «Two-dimensional

magnetohydrodynamic simulation of a magnetic sail,» *Journal of Spacecraft and Rockets*, vol. 43, n. 3, pp. 667-672, 2006.